Electron-N_2^+ scattering and dynamics

Duncan Adam Little

University College London

A dissertation submitted for the degree of

Doctor of Philosophy

March 2015

Declaration

I, Duncan Adam Little, confirm that the work presented in this thesis is my own. Where information has been derived from other sources, I confirm that this has been indicated in the thesis. The work contains nothing which is the outcome of work done in collaboration except where specifically indicated in the text.

Parts of this dissertation have been published as follows.

Chapter 4: D. A. Little and J. Tennyson, 'An *ab initio* study of singlet and triplet Rydberg states of N_2', *Journal of Physics B: Atomic, Molecular and Optical Physics*, **46** (2013) 145102.

Chapter 5: D. A. Little and J. Tennyson, 'An R-matrix study of singlet and triplet continuum states of N_2', *Journal of Physics B: Atomic, Molecular and Optical Physics*, **47** (2014) 105204.

Chapter 6: D. A. Little, K. Chakrabarti, J. Zs. Mezei, I. F. Schneider and J. Tennyson, 'The dissociative recombination of N_2^+: an *ab initio* study', *Physical Review A: Atomic, Molecular and Optical Physics*, **90**, (2014) 052705.

Duncan Adam Little

March 2015

Abstract

Molecular nitrogen, N_2, is the most abundant molecule in the terrestrial atmosphere. Its cation N_2^+ is therefore prevalent in the earth's ionosphere as well as in nitrogen plasmas produced for reasons varying from lightning strikes to combustion. Any model which seeks to describe plasmas in air must contain a description of nitrogen ion chemistry. Despite this, there is a distinct paucity of data describing electron-N_2^+ interactions and the resultant bound and quasi-bound electronic structure of N_2. The characterisation of these states is essential for describing dissociative recombination which is the main destroyer of molecular ions in a plasma. This thesis aims to alleviate this problem by performing extensive *ab initio* R-matrix calculations to create a comprehensive map of the highly-excited electronic structure of N_2 which can the be used to perform a dissociative recombination cross-section calculation.

Potential energy curves were found by performing resonant and bound state calculations for all singlet and triplet molecular symmetries of N_2 up to $\ell \leq 4$. The use of a dense grid meant that highly-excited electronic states could be found with an unprecedented level of detail. Many of the states were previously unknown. A new fitting method was developed for the characterisation of resonant states using the time-delay method. It was shown that whilst the R-matrix method is not competitive with conventional quantum chemistry techniques for low lying valence states, it is particularly appropriate for highly-excited states, such as Rydberg states.

The data gained from these calculations was then used as an input for a multichannel quantum defect theory calculation of a dissociative recombination cross-section. A description is given of how to prepare the data from the R-matrix calculation for input into a multichannel quantum defect theory dissociative recombination cross-section calculation. Cross-sections were found for $v_i^+ = 0 - 3$ including three ionic cores. Whilst previous studies of dissociative recombination using R-matrix data required some empirical intervention, the cross-section found in this thesis is completely *ab initio* and is in good agreement with experiment.

Acknowledgements

First and foremost I would like to thank my supervisor Prof. Jonathan Tennyson for his support, unfailingly good humour, and enthusiasm. Throughout the course of my Ph.D I always felt I was in safe hands with regards to any matter, no matter how trivial. Without Jonathan's help, patience and advice, completing this degree would have been a near impossible task.

Secondly I would like to thank Prof. Ioan F. Schneider at the University of Le Havre for his collaborative effort on the dissociative recombination cross-section calculation and the many helpful discussions we have had. I'd also like to thank Ioan for his welcoming and inclusive attitude towards scientific research. I'd like to thank the other collaborators on the dissociative recombination calculation: Dr. Kalyan Chakrabarti and Dr. Zsolt Mezei.

I would like to thank Drs. Peter and Penny Marriot from Themisys Ltd. for providing the funding for me to complete my Ph.D. Without their financial support and enthusiasm for the subject none of this would have been possible.

I would like to thank Dr. Zdenek Masin for his help and advice on using MOLPRO orbitals in the UKRMol codes.

I would like to thank Dr. Andrew Sunderland and Dr. Martin Plummer for the provision of computer time to complete the time-delay resonance calculation.

I would like to thank my Mother and Father for their love and support throughout the completion of this degree. Without their encouragement and patience I could have never have hoped to be in the position that I am now. I'd also like to thank my brothers for their occasional reluctant acknowledgement of my work.

Last but not least I would like to thank all of my friends at UCL, in particular: Bobby Antonio, Seto Balian, Martin Uhrin, Hugh Price, Clara Sousa-Silva, Ahmed Al-Refaie, Georg Schusteritsch and James Millen for sharing this experience with me. I'd also like to thank all of my friends outside of UCL; particular thanks go to Edmund Lovell, George Harrington and Vikesh Mistry. My overriding feeling of my time at UCL has been one of laughter and enjoyment.

Contents

List of Figures

List of Tables

Chapter 1

Introduction

The Earth's atmosphere is a mixture of gases which surround the planet due to the gravitational attraction of its mass. Any space vehicle that wishes to travel to the Earth's surface from outer space must pass through its atmosphere. Due to the gravitational capture of the space vehicle by the Earth, the space vehicle free falls through the atmosphere at speeds of around Mach 25. This free fall through the Earth's atmosphere is known as re-entry, that is, assuming that the space vehicle originated from Earth.

During re-entry the relative velocity of the vehicle and the air flow surrounding it is high enough that the flow becomes hypersonic and a bow shock is formed (Anderson, 1989). As atmospheric constituents pass through the bow shock, the particle velocity decreases significantly resulting in a huge increase in the temperature and density of the gas. This increase in temperature and density results in the atomic and molecular constituents becoming ionised and electronically and vibrationally excited. The result of this is that the gas is now a highly reactive high temperature plasma.

The largest constituent of the Earth's atmosphere is molecular nitrogen, N_2, and therefore its cation, N_2^+, plays a major role in the chemistry of the re-entry plasma; if one wishes to describe this plasma correctly then a correct description of the processes involving electron-molecule collisions with this ionised molecule is essential. Providing this description by characterising electron–molecule scattering and dynamics with N_2^+ is the focus of this thesis.

1.1 Motivation

Despite the obvious successes in space travel (NASA, 1975), producing a reliable model of a spacecraft re-entering an atmosphere is still a significant problem. Due to the extreme conditions of re-entry, laboratory measurements are difficult, therefore there is a strong interest in producing accurate computational models of the plasma surrounding the re-entering space vehicle (Bird, 1989; Bultel et al., 2002, 2006; Boyd, 2007; Ozawa et al., 2008; Gallis et al., 2009; Bird, 2011; Li et al.,

Table 1.1: Processes relevant in re-entry plasmas involving N_2^+. i, ν and j, ω indicate initial and final electronic, vibrational states of the molecules and atomic products respectively.

	Process description
Electron impact electronic excitation	$N_2^+(i) + e^- \longrightarrow N_2^+(j) + e^-$
Dissociative excitation	$N_2^+(\nu) + e^- \longrightarrow N^+ + N + e^-$
Dissociative recombination	$N_2^+(\nu) + e^- \longrightarrow N + N$
Electron impact vibrational excitation	$N_2^+(\nu) + e^- \longrightarrow N_2^+(\omega) + e^-$

2011; Bultel and Annaloro, 2013; Annaloro et al., 2014). The models which seek to describe the re-entry plasma can be thought of as existing on two levels; a dynamical description of an ensemble of particles colliding with each other such as the direct simulation Monte Carlo (DSMC) method of Bird (2009), implemented by Marriot and Marriot (2012) in the UK DSMC codes, and the individual quantum mechanical behaviour of each particle interacting with another. This quantum mechanical description is in general complex and it is not practical in most cases to implement on a large scale. Therefore, one must try to capture the essential parts of the full quantum mechanical description in a way that can be included in a large scale dynamical calculation. This can be achieved by theoretically calculating or experimentally measuring the cross-section of an interaction between particles. The cross-section is an effective area which describes the probability of an interaction occurring. As these many-particle descriptions are on the macro-scale, cross-sections are often thermally averaged to give a reaction rate-coefficient. This describes the rate of a process as a function of temperature. The rate-coefficients then control the relative proportions of each constituent of the plasma as they interact on the macro-scale.

Due to the reactive nature of re-entry plasmas many chemical processes are relevant to these models (Bultel and Annaloro, 2013), those involving N_2^+ can be see in table 1.1. There have been a number of attempts to compile sets of reaction rates to correctly describe these processes for re-entry models (Johnston, 1968; Bortner, 1969; Gupta et al., 1990; Park, 1990, 1993). However, all of these compilations suffer from a common problem, there is a distinct lack of data for reaction-rates at temperatures relevant to space vehicle re-entry ($T_e \gtrsim 10000$ K, where T_e is electron temperature); as a result, the high temperature data in these compilations are extrapolations of low temperature data (Park, 1990; Reese et al., 2003; Gallis et al., 2009; Bird, 2011). In some cases this extrapolation is justified, however in others the uncertainty in the extrapolation can be as large as one order of magnitude or even unknown (Park, 1990). There is, therefore, a need for more accurate high temperature cross-sections and reaction rates for processes relevant to re-entry plasmas.

Whilst an experimental measurement could be considered to give the most exact representation of a cross-section or reaction rate-coefficient, it is usually the case that it is only valid over a small temperature range and extrapolation is necessary. When performed with care a theoretical calculation can yield an accurate and more general cross-section applicable over a large temperature range. To fully exploit this advantage, the candidate process for a theoretical calculation should be one which does not behave predictably with increasing temperature and therefore extrapolation from low temperatures is not justified. One process which fulfils this criteria is the dissociative recombination (DR) of N_2^+. DR is a vital process in all plasmas as it is the main destroyer of ions (Larsson and Orel, 2008), it has a cross-section which behaves non-linearly with increasing vibrational temperature and hence fulfils the above criteria.

1.2 Dissociative recombination

If a free electron has non-zero kinetic energy and it recombines with a molecular ion then its energy must be dissipated in some way so that it can form a bound state. A molecule can use its internal chemical structure to break one or many of its chemical bonds to move the electron to a bound state. The breaking of a bond or bonds which leads to the molecule breaking up is known as dissociation. The stabilisation of the recombining electron through dissociation is known as dissociative recombination.

The process of dissociative recombination can be described for diatomic molecules as

$$\mathrm{AB}^+ + \mathrm{e}^- \rightarrow \text{intermediate state} \rightarrow \mathrm{A} + \mathrm{B} \tag{1.1}$$

where A and B are both N for the DR of N_2^+. An electron collides with an ionised molecule, there is then an intermediate state which results in the dissociation of the molecule to two neutral atoms; the nature of this intermediate state will be discussed below. One or both of the atomic products are generally in an excited electronic state.

Although this process may appear at first to be relatively simple, it is in fact one of the most complex and poorly understood processes involving small molecules (Florescu-Mitchell and Mitchell, 2006; Larsson and Orel, 2008).

1.2.1 Dissociative recombination mechanisms

There are a number of different ways in which the process can occur, the first is known as the 'direct' mechanism. The direct mechanism occurs when the electron is captured into a doubly excited high-lying resonant state of the neutral molecule, denoted as AB^{**}. These states, often known as valence states, are embedded in the electron-ion continuum above the ionisation threshold of the molecule. If, with increasing internuclear separation, the resonant valence state crosses the ion ground state and becomes bound the electron will become stable with respect to autoionisation. The molecule will then dissociate. States which lead to dissociation are known as 'dissociative'. The intermediate state in this mechanism is then the doubly excited resonant state, AB^{**}, and the

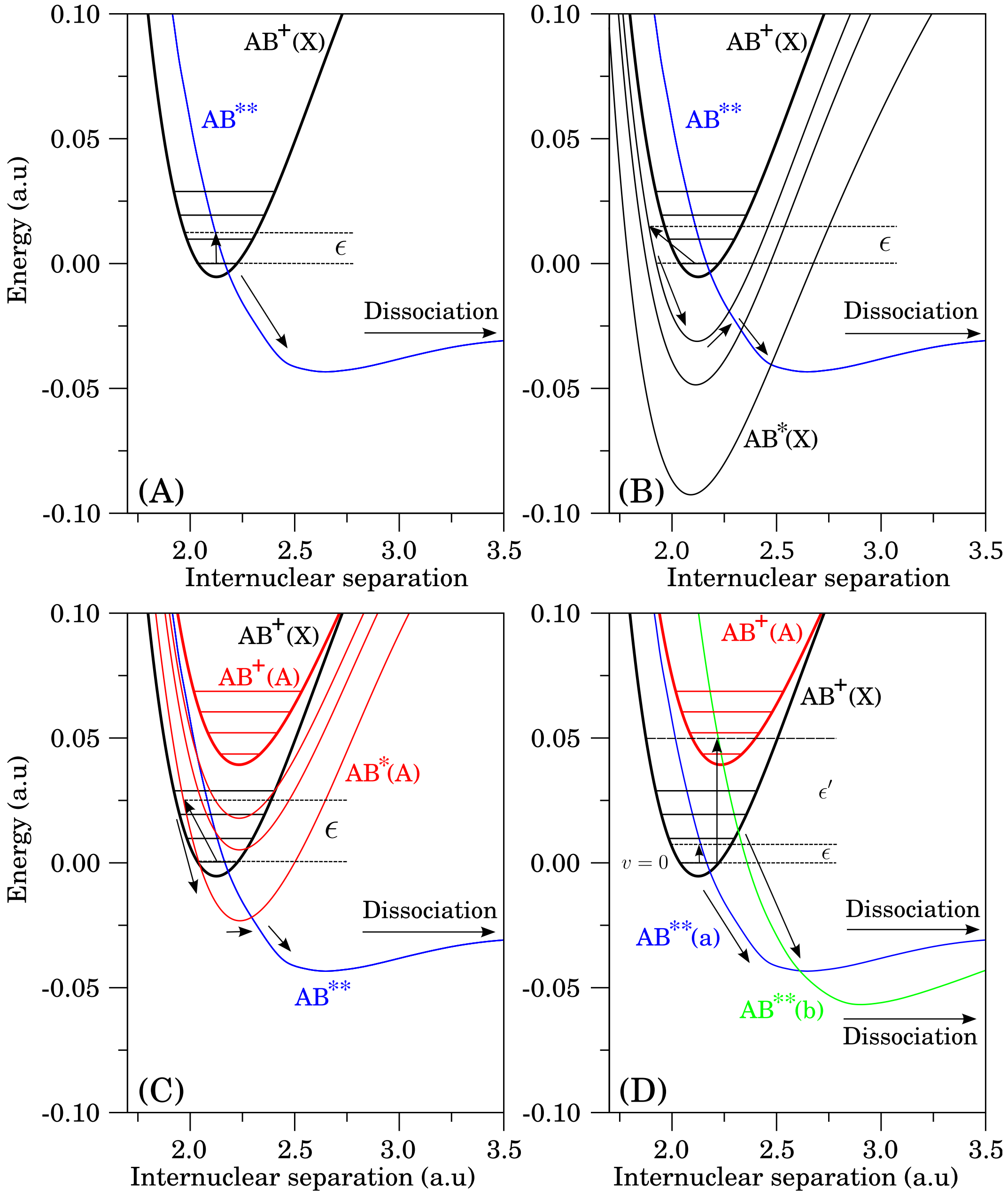

Figure 1.1: Mechanisms of DR. (A) the direct mechanism, (B) the indirect mechanism, (C) the indirect mechanism with core excited Rydberg states, (D) the direct mechanism with multiple curve crossings. The mechanisms are described in detail in the text.

full process can be written,

$$\mathrm{AB}^+ + \mathrm{e}^- \rightarrow \mathrm{AB}^{**} \rightarrow \mathrm{A} + \mathrm{B}. \tag{1.2}$$

This mechanism is shown in panel (A) of figure 1.1, the black curve represents the potential energy curve (PEC) of the ground state of the ion, $\mathrm{AB}^+(\mathrm{X})$ where X denotes the electronic ground state. The blue curve represents a doubly excited neutral state of the ion, AB^{**}, which leads to dissociation. The electron collides with the ion with some energy ϵ, this excites the molecule into the state AB^{**}, as this state is a resonance it has some survival probability against autoionisation related to its autoionisation width. If the survival probability is sufficiently large then the internuclear separation will increase beyond the crossing point of the dissociative state and the ion ground state before the electron has a chance to autoionise. Beyond this crossing point the dissociative state is bound and stable against autoionisation, this then leads to dissociation. The AB^{**} state in panel (A) of figure 1.1 crosses the ground state of the ion very close to its turning point, therefore only a small survival probability is required for the molecule to dissociate. That is, only a small increase in internuclear separation is needed for the dissociative state to cross the ground state and lead to dissociation. If the electron does autoionise before the molecule has a chance to dissociate then the excess energy is transferred to vibrational modes of the molecule resulting in vibrational excitation, this process is known as electron impact vibrational excitation and is shown in table 1.1.

As these dissociative states are high-lying they pass through the Rydberg series converging on the ground state of the ion. There will be an interaction between the valence states and the Rydberg states which leads to two important considerations, firstly the molecule can move to another dissociative state via a Rydberg state, this only affects the final atomic products of the process known as the branching ratios. The branching ratios give the relative proportions of the final atomic products of DR; as the states are in general, high-lying, there are usually no routes to the lowest asymptotes of the molecule meaning that these product channels are closed. The DR of N_2^+ produces the following atomic products: $N(^4S) + N(^2D)$, $N(^4S) + N(^2P)$, $N(^2D) + N(^2D)$ and $N(^2D) + N(^2P)$. Secondly an electron could be captured into a highly vibrationally excited Rydberg state associated with ground state of the ion, denoted $AB^*(X)$, as Rydberg states are bound they cannot dissociate directly; they can however couple to a dissociative state which will then cause the molecule to dissociate. This is known as the ‘indirect mechanism’. As the direct and indirect mechanisms lead to the same products they interfere with each other; the indirect process causes sharp structures in the cross-section as a function of energy. The intermediate state for this process is then $AB^*(X) \rightarrow AB^{**}$ and the full process can be written,

$$AB^+ + e^- \rightarrow AB^*(X) \rightarrow AB^{**} \rightarrow A + B. \tag{1.3}$$

This mechanism is shown in panel (B) of figure 1.1, the narrow black curves represent the Rydberg states associated with the ground state of the ion, $AB^*(X)$. The electron with energy ϵ excites the molecule into a highly excited vibrational state of a Rydberg state. This state then couples to a dissociative state AB^{**} which leads to dissociation.

A third possibility exists if there are low-lying excited states of the molecular ion. These states will have Rydberg states converging upon them. An electron can then be captured into one of these ‘core-excited’ Rydberg states, denoted $AB^*(A)$, which can then couple to a dissociative state leading to dissociation. This process can be written,

$$AB^+ + e^- \rightarrow AB^*(A) \rightarrow AB^{**} \rightarrow A + B, \tag{1.4}$$

and is shown in in panel (C) of figure 1.1. The red lines represent Rydberg states associated with the first excited state of the ion $AB^+(A)$. It is identical to the indirect process described above apart from that the Rydberg state is associated with an excited state of the ion.

The processes above represent the three routes to dissociation for a molecule with curve crossings; DR can occur in molecules without curves crossing such as HeH^+ (Sarpal et al., 1994) through direct predissociation (Larsson and Orel, 2008).

There maybe, of course, more than one dissociative state that crosses the ground state of the ion. This situation is illustrated in panel (D) of figure 1.1.

1.2.2 Vibrational dependence

The direct DR cross-section depends on two couplings, the electronic coupling of the dissociative state to the electron-ion continuum and the vibronic coupling between the dissociative state and the ion. Therefore a dissociative state which is favourable for DR must have two qualities: be strongly coupled to the electron-ion continuum (a large autoionisation width in scattering theory language) and have a large overlap of wavefunctions with the vibrational state of the ion. Therefore the initial vibrational state of the ion can have a significant effect on the DR cross-section. When the ion is in its vibrational ground state, any curve crossing close to the turning point of the ion will have a significantly larger overlap than one that crosses at an internuclear separation outside the range of the $v = 0$ state. See for example, panel (A) in figure 1.2; two dissociative states $AB^{**}(a)$ and $AB^{**}(b)$ (red and green) cross the ground state of the ion at different internuclear separations. The modulus squared of the wavefunction for each vibrational level is displayed in black, the modulus squared of the wavefunctions at E $(v = 0)$ of the two dissociative states are given in red and green to match their respective state, where E $(v = 0)$ is the energy of the vibrational ground state of the ion. Consider the case that the ion is initially in the $v = 0$ state. There is a significant overlap between the $v = 0$ vibrational wavefunction and the wavefunction of the $AB^{**}(a)$ state; resultantly it is highly likely the molecule will dissociate via this dissociative state. Conversely, there is only a small overlap with the $v = 0$ vibrational wavefunction and the wavefunction of the $AB^{**}(b)$ state, so dissociation is unlikely via this route. So for the case when $v = 0$ there is only one probable route to dissociation, via the $AB^{**}(a)$ dissociative state.

The same situation is shown again in panel (B) but this time for the molecule in an excited initial vibrational state, $v = 1$. Now both the $AB^{**}(a)$ and $AB^{**}(b)$ have a significant overlap with the wavefunction of the $v = 1$ state and there are now two probable routes to dissociation.

This demonstrates that there is non-linearity in the magnitude of the cross-section with increasing vibrational excitation, as the molecule becomes more vibrationally excited, more routes to dissociation become available. The opposite can also happen, as there are nodes in both the dissociative and vibrational wavefunctions, for some vibrational levels this can lead to a decrease

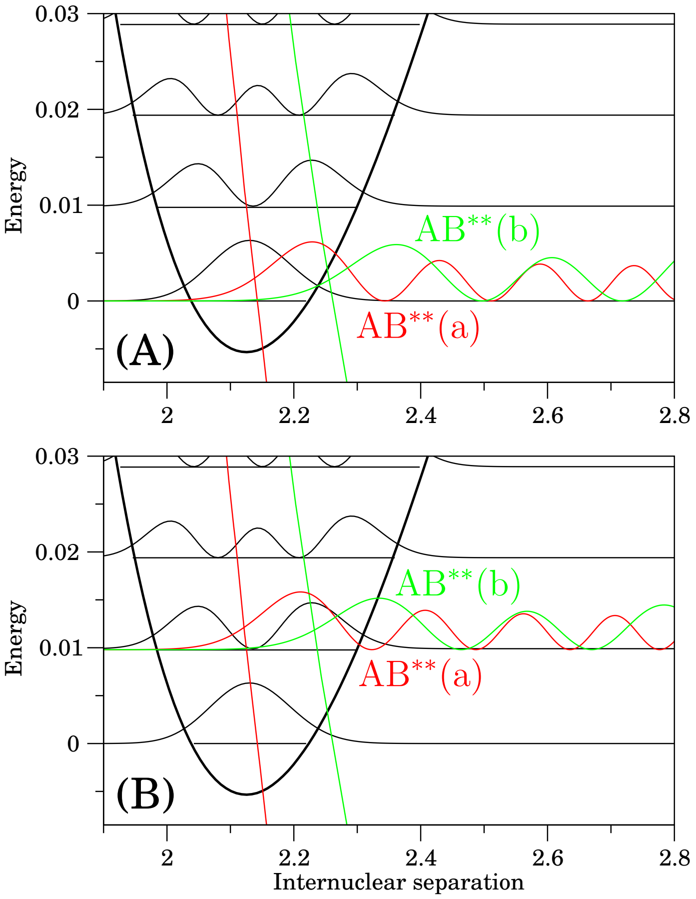

Figure 1.2: A plot to demonstrate the variation in overlap of the vibrational wavefunction of the ion and the wavefunction of the dissociative state. Two dissociative states AB**(a) and AB**(b) are shown in red and green with the respective modulus squared of their wavefunctions. The modulus squared of the vibrational wavefunctions of the ion are shown in black.

in overlap and the size of the cross-section can decrease. Therefore with increasing vibrational temperature, DR is a process which does not behave predictably.

1.2.3 Dissociative recombination of N_2^+

Experimental studies

Due to the prevalence of N_2 in the Earth's atmosphere the DR of N_2^+ has received much experimental attention since it was first discussed by Bates and Massey in 1946 (Bates and Massey, 1946). Initial stationary afterglow (Larsson and Orel, 2008) measurements (Faire et al., 1958; Bialecke and Dougal, 1958; Faire and Champion, 1959; Kasner et al., 1961; Mentzoni, 1963; Hackam, 1965) were hampered by the formation of cluster ions, for example N_4^+, and a lack of a mass spectrometer. Rate-coefficients ranged from 1.2×10^{-7} cm^3 s^{-1} (Mentzoni, 1963) to 1.2×10^{-6} cm^3 s^{-1} (Faire et al., 1958) for measurements at room temperature. Once, however, the problem had been identified it was easily remedied by the use of a mass spectrometer to ensure that only N_2^+ was present in the measurement and a rate of 1.8×10^{-7} cm^3 s^{-1} was found by (Mehr and Biondi, 1969). Since then there have been other stationary afterglow measurements (Zipf, 1980), flowing afterglow Langmuir probe measurements (FALP) (Mahdavi et al., 1971; Geoghegan et al., 1991; Canosa et al., 1991), shock tube measurements (Cunningham and Hobson, 1972), merged beams measurements (Mul and McGowan, 1979; Noren et al., 1989; Sheehan and St.-Maurice, 2004) and a single storage ring measurements (Peterson et al., 1998). There should also be a mention of the storage ring measurement of $^{15}N^{14}N$ by Kella et al. (1996) which only gave branching ratios. The results of these measurements are more consistent with a range of 1.5–2.6×10^{-7} cm^3 s^{-1} at 300 K, but are not as consistent as other diatomic ions of a similar size, such as O_2^+ and NO^+

The reason for this lack of consistency can be attributed to the difficulties cooling N_2^+ to its vibrational ground state. Storage rings have revolutionised our ability to measure DR rates reliably for small molecules (Florescu-Mitchell and Mitchell, 2006; Larsson and Orel, 2008), not least because the ability to store ions for a sufficiently long time for them to cool means that measurements can be made from vibrationally and rotationally cold molecules. It transpires, however, that N_2^+, which has no electric permanent dipole moment, is particularly difficult to cool even in long-lived beams in storage rings (Peterson et al., 1998). N_2^+ is also only partially susceptible to collisional quenching (Sheehan and St.-Maurice, 2004). With the exception of the FALP measurements, which utilise a buffer gas to cool the ions, all modern measurements have been performed on vibrationally hot ions. No FALP measurements have been made to date which provide a temperature dependence of the rate-coefficient.

Theoretical studies

Guberman has published a series of articles on theoretical calculations of the DR cross-section of N_2^+ (Guberman, 1991, 2003, 2007, 2012, 2013) using high quality curves and couplings computed using standard quantum chemistry procedures, such as multireference configuration interaction (MRCI), and a multichannel quantum defect theory (MQDT) treatment of the actual DR process. MQDT is a quantum mechanical method which considers the DR problem in terms of interacting ionisation and dissociation channels and has proven to be the most successful method for calculating DR cross-sections to date (Larsson and Orel, 2008).

Whilst these studies show good agreement with experiment, there is still some level of empirical intervention in the model and they could not be called completely *ab initio* . Two separate calculations must be performed for ion ground state and the neutral dissociative curves, the ion ground state is then placed at the experimental ionisation energy. As discussed in the previous section, for DR the relative placement of the ion curve and neutral states can have a significant effect on the cross-section. It is difficult to produce a self-consistent model using an MRCI calculation. Orbitals must be tailored for each symmetry to produce correct results. The electronic couplings discussed in the previous section can only be approximated using quantum chemistry techniques (Larsson and Orel, 2008) with the use of Fermi's Golden Rule.

Secondly the data provided in these studies is relatively limited, the highest vibrational level computed is $v = 4$ and electron temperature is $T = 3000$ K. For re-entry problems the plasma electron temperatures are $\gtrsim 10000$ K (Bultel and Annaloro, 2013), this corresponds to an electron impact energy of around 6 eV. To compute cross-sections for energies this high, one must include all the dissociative states which cross the ion ground state up to this energy as well as the couplings for each state. Confidently computing states this high above the ground state of a neutral is difficult with standard configuration interaction calculations (Larsson and Orel, 2008); the accuracy of the calculation decreases with increasing energy.

Electron–molecule scattering techniques such as the *ab initio* R-matrix method (Tennyson, 2010) lend themselves more naturally to computing the necessary inputs for the calculation of a DR cross-section. The starting point of the calculation is the target state of the ion, all parameters are computed self-consistently from this point. The doubly excited neutral states can be found by detecting resonances above the ground state of the ion; the width of these resonances provides the electronic coupling described in the previous section. The neutral states can then be tracked below the ground state of the ion using a bound state calculation. This calculation also provides the quantum defects necessary to describe the Rydberg states and the indirect mechanism described above (Rabadán and Tennyson, 1996). In short, the R-matrix method provides all of the necessary tools to compute, completely *ab initio*, the inputs for a DR cross-section. Data from R-matrix calculations has been used previously to successfully compute DR cross-sections with MQDT for NO^+ (Schneider et al., 2000); however, it was necessary to empirically adjust the position of the neutral curves to find agreement with experiment.

1.3 The aim of this thesis

It is instructive at this point to summarise the discussion so far. N_2 and its cation N_2^+ are of fundamental importance to atmospheric plasmas. One such plasma is that which surrounds a space vehicle as it re-enters the Earth's atmosphere. A process of particular importance and complexity is dissociative recombination, this process behaves unpredictably with increasing temperature and so extrapolating a low temperature cross-section or rate is not appropriate. Measuring the ground state cross-section of the DR of N_2^+ has proven to be difficult, this makes a theoretical calculation relevant. DR cross-sections are dependent on the electronic structure of the molecule, as a result there is no general formula to calculate a DR cross-section. Input parameters must be found individually for each molecule then used to compute a cross-section. Previous theoretical calculations by Guberman used input data calculated by quantum chemistry techniques and provide only limited data on cross-sections and rates. A more natural approach to calculating the input parameters would be to use a scattering technique such as the R-matrix method, these inputs can then be used to calculate a comprehensive set of cross-sections and rates for the DR of N_2^+ using MQDT. The only other previous DR cross-section calculation using R-matrix data by Schneider et al. (2000) required empirical intervention to find agreement with experiment. The aim of this thesis is to produce a completely *ab initio* DR cross-section where no empirical data is required.

If performed in a comprehensive manner, the calculation of the inputs will also yield a detailed description of the super-excited electronic structure of N_2 above and below the ground state of the ion. MQDT calculations also provide electron impact vibrational excitation cross-sections, see table 1.1.

The aim of this thesis is then this: to first calculate the input parameters needed to calculate a DR cross-section of N_2^+ for temperatures relevant to space vehicle re-entry using the R-matrix method, this will be the main focus of the thesis. Secondly to use these parameters to calculate a DR cross-sections using multichannel quantum defect theory (MQDT).
The parameters that need to be found for an MQDT calculation of a DR cross-section are (Florescu-Mitchell and Mitchell, 2006);

1. Potential energy curve (PEC) of the ground state of the ion.
2. PECs of the neutral which cross the ion close to the turning point of the ion ground state with their respective asymptotes.
3. Electronic couplings between the neutral valence states and the electronic-ion continuum.
4. Quantum defects of the Rydberg series converging on the ion.

For a DR cross-section that includes 'core-excited' Rydberg states of the ion one additionally requires;

5. PECs of the excited ion states.
6. Rydberg-Rydberg coupling between each series converging on each state of ion.
7. Quantum defects of the core-excited Rydberg series considered.

All of these parameters can be calculated using the R-matrix method. Electronic structure calculations are used to find the potential energy curves of the ion or, in the context of a scattering calculation, the target molecule. The properties of the neutral molecule are found by introducing an additional scattering electron into the model. This provides the information needed to find the neutral potential energy curves. Below the ground state of the ion the scattering problem is solved for negative scattering energies, giving us bound states. Above the ground state we find neutral electron scattering resonances of the ion at many bond lengths, the widths of these resonances also provide electronic couplings. By combining the bound and resonant states of the ion a complete description of the electronic structure above and below ionisation threshold is given. This thesis will show the steps that need to be taken to carry out the above calculations and then, in turn, to calculate a dissociative recombination cross-section.

1.4 Outline of this thesis

With consideration of the final statement of the previous section, this thesis will be organised as follows. Chapter 2 will give an overview of the theory of the R-matrix method used to calculate the input parameters for a DR cross-section. Chapter 3 describes the computational advances that were made to compute resonances. Chapter 4 will discuss the computation of bound states. Chapter 5 the computation of the resonant states. Finally chapter 6 will give a brief overview of the theory of MQDT and the actual computation of the DR cross-section. The conclusions of this thesis are in chapter 7. Included in each chapter, when relevant, is a detailed comparison with previous work.

Chapter 2

The R-matrix method

2.1 Introduction

In this chapter an overview of the theory of the fixed-nuclei R-matrix method and its implementation in the UKRmol codes will be given.

The R-matrix method was originally proposed by Wigner in the 1940s (Wigner, 1946; Wigner and Eisenbud, 1947) for nuclear scattering processes. In the 1970s the R-matrix method was established as a technique for the treatment of electron-atom (Burke et al., 1971; Robb, 1972; Burke, 1973) and electron-diatomic molecule scattering (Schneider, 1975; Schneider and Hay, 1976; Burke et al., 1977). However, it was not until the 1990s that polyatomic codes were developed for general electron-molecule scattering (Nestmann et al., 1994; Morgan et al., 1997, 1998). Comprehensive reviews of the method and of recent work are given by Burke (2011) for electron-atom and electron-molecule scattering and Tennyson (2010) for electron-molecule scattering only.

The defining feature of the R-matrix method is the partitioning of space into two distinct regions by a sphere of radius a, centred on the centre-of-mass of the molecule, see figure 2.1. This sphere separates the 'inner region' from the 'outer region', which is the space outside of the sphere. Within the inner region, the scattering electron is considered to be indistinguishable from the electrons of the target molecule, hence correlation and exchange effects must be taken into consideration. Beyond a, in the outer region, the electron is treated as being distinct and only long-range interactions are considered. The inner region is split again into two separate calculations; a target calculation, which just considers the N target electrons interacting, and a target plus electron or $(N+1)$-electron calculation, in which the scattering electron is allowed to interact with all target electrons in the active space. The results of these two calculations are then combined in the outer region to calculate scattering properties. A balanced treatment between these two calculations is crucial for obtaining good results, see section 4.2.2 of chapter 4. The R-matrix itself acts as the interface between the two separate regions and constructed on the boundary between;

it acts to link the inner region solutions to their matching asymptotic scattering solution.

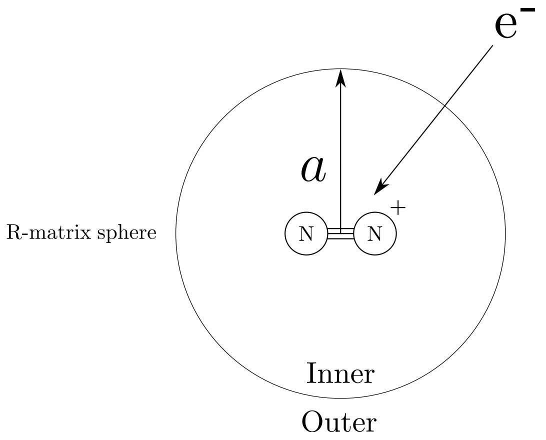

Figure 2.1: A diagram showing the R-matrix sphere surrounding an N_2^+ molecule. Space is separated into the 'inner' and 'outer' regions by a sphere of radius a.

2.2 Fixed-nuclei R-matrix theory

2.2.1 Born-Oppenheimer approximation

The work performed in this thesis was carried out using the fixed-nuclei formulation of R-matrix theory. This use of this formulation, often known as the Born-Oppenheimer approximation, means that the nuclear and electronic motion are separated in the wavefunction of the molecule. This approximation is valid in situations where the electron's response to the movement of the nuclei is much faster than the movement of the nuclei themselves and is therefore often referred to as an 'adiabatic approximation'.

The most noticeable implication of the Born-Oppenheimer approximation for electronic structure calculations of diatomic molecules is the appearance of avoided crossings in potential energy curves. The avoided crossings are the result of the von Neumann-Wigner non-crossing rule (see appendix A) which states that two electronic curves of the same symmetry or irreducible representation cannot cross. The non-crossing rule arises from the fact that the electronic Hamiltonian is only dependent on a single variable, the internuclear separation, R.

2.2.2 Inner region Hamiltonian and R-matrix equation derivation

The starting point of the formulation is to choose a reference frame in which a target diatomic molecule, AB, is aligned along the z-axis with the centre of mass (C.M.) of the molecule at the origin of the coordinate system. Such a situation is shown in figure 2.2. The two nuclei labelled, A and B are separated by a distance $R = R_A + R_B$ and fixed in space. The i^{th} electron is separated from A, B and the C.M. by r_{Ai}, r_{Bi}, and r_i respectively. The target molecule has N electrons and the two nuclei have a charge Z_A and Z_B.

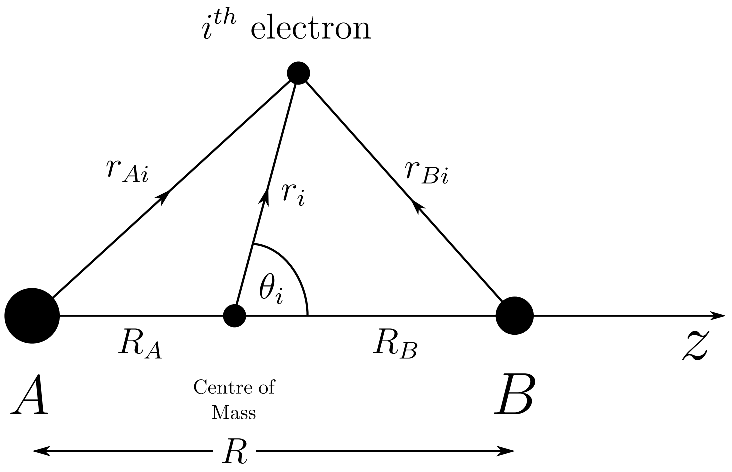

Figure 2.2: A schematic representation of an electron interacting with a molecule AB.

The scattering process is then described by the Hamiltonian,

$$H_{N+1}|\Psi\rangle = E|\Psi\rangle, \tag{2.1}$$

where the subscript $N+1$ indicates that the Hamiltonian describes the N electrons belonging to the target plus the additional scattering electron. The Hamiltonian, H_{N+1}, is defined in atomic units as,

$$H_{N+1} = \sum_{i=1}^{N+1}\left(-\frac{1}{2}\nabla_i^2 - \frac{Z_A}{r_{Ai}} - \frac{Z_B}{r_{Bi}}\right) + \sum_{i>j=1}^{N+1}\frac{1}{r_{ij}} + \frac{Z_A+Z_B}{R}, \tag{2.2}$$

where $-\frac{1}{2}\nabla_i^2$ is the kinetic energy of i^{th} electron, $-\frac{Z_A}{r_{Ai}}$, $-\frac{Z_B}{r_{Bi}}$, the Coulomb potential between the A, B atoms and the i^{th} electron, $\frac{1}{r_{ij}}$ the mutual repulsion between the i^{th} and j^{th} electron and $\frac{Z_A+Z_B}{R}$ the mutual repulsion between the two nuclei.

In the inner region, the solution to eq. (2.1) has the form,

$$|\Psi^{\Delta}\rangle = \sum_k A_k(E)|\psi_k^{\Delta}\rangle. \tag{2.3}$$

ψ_k^{Δ} are energy independent basis functions, Δ represents a set of conserved quantum numbers that correspond to a molecular symmetry.

The R-matrix sphere, see figure 2.1, introduces a spatial restriction to the system. The addition of this spatial restriction results in non-zero surface terms and the Hermicity of the Hamiltonian is lost. To solve this issue the Bloch operator $\mathcal{L}_{N+1}$ (Bloch, 1957) is added to the Hamiltonian, the result of this is the cancelling out the surface terms and a Hermitian Hamiltonian. The Bloch operator is written,

$$\mathcal{L}_{N+1} = \sum_{i=1}^{N+1}\frac{1}{2}\delta(r_i - a)\left(\frac{d}{dr_i} - \frac{b-1}{r_i}\right). \tag{2.4}$$

By adding the Bloch operator to both sides of eq. (2.1) and rearranging, the following expression is found,

$$(H_{N+1} + \mathcal{L}_{N+1} - E)|\Psi^{\Delta}\rangle = \mathcal{L}_{N+1}|\Psi^{\Delta}\rangle, \tag{2.5}$$

which has the formal solution,

$$|\Psi^{\Delta}\rangle = (H_{N+1} + \mathcal{L}_{N+1} - E)^{-1}\mathcal{L}_{N+1}|\Psi^{\Delta}\rangle. \tag{2.6}$$

Using the resolution of the identity,

$$\sum_k |\psi_k^{\Delta}\rangle\langle\psi_k^{\Delta}| = 1 \tag{2.7}$$

eq. (2.6) is rewritten,

$$\begin{aligned}
|\Psi^{\Delta}\rangle &= \sum_{k,k'} |\psi_k^{\Delta}\rangle\langle\psi_k^{\Delta}|(H_{N+1} + \mathcal{L}_{N+1} - E)^{-1}|\psi_{k'}^{\Delta}\rangle\langle\psi_{k'}^{\Delta}|\mathcal{L}_{N+1}|\Psi^{\Delta}\rangle && (2.8)\\
&= \sum_{k,k'} \frac{|\psi_k^{\Delta}\rangle\langle\psi_k^{\Delta}|\mathcal{L}_{N+1}|\Psi^{\Delta}\rangle}{E_k - E}\delta_{kk'} && (2.9)\\
&= \sum_{k} \frac{|\psi_k^{\Delta}\rangle\langle\psi_k^{\Delta}|\mathcal{L}_{N+1}|\Psi^{\Delta}\rangle}{E_k - E}. && (2.10)
\end{aligned}$$

Comparing eq. (2.10) with eq. (2.3) it can be seen that

$$A_k(E) = \frac{\langle\psi_k^{\Delta}|\mathcal{L}_{N+1}|\Psi^{\Delta}\rangle}{E_k - E}. \tag{2.11}$$

Again with the use of the identity matrix, this time using a channel basis function $|\phi_j^N Y_{l_j}^{m_j}\rangle$, the Bloch operator is expanded as,

$$\mathcal{L}_{N+1} = \sum_{i=1}^{N+1}\sum_{j=1} \frac{1}{2}|\phi_j^N Y_{\ell_j m_{\ell_j}}\rangle\delta(r_i - a)\left(\frac{d}{dr_i} - \frac{b-1}{r_i}\right)\langle\phi_j^N Y_{\ell_j m_{\ell_j}}|. \tag{2.12}$$

Two new functions are defined, the reduced radial functions

$$F_j^{\Delta}(a) = \langle\phi_j^N Y_{\ell_j m_{\ell_j}}|\Psi^{\Delta}\rangle, \tag{2.13}$$

and energy independent surface amplitudes,

$$\omega_{jk}^{\Delta}(a) = \langle\phi_j^N Y_{\ell_j m_{\ell_j}}|\psi_k^{\Delta}\rangle. \tag{2.14}$$

Where ϕ_j^N is the N-electron target wavefunction for channel j. Details of how different values of ℓ and corresponding values of m_ℓ form molecular orbitals in the $\mathrm{D}_{\infty\mathrm{h}}$ irreducible representation (the symmetry group of N_2) are given in appendix C. Substituting eq. (2.12) in to eq. (2.11) and using the definitions given in equations (2.13) and (2.14) gives the following expression for the expansion coefficients in (2.3),

$$A_k(E) = \frac{1}{2}\sum_{j=1} \frac{\omega_{jk}^{\Delta}(a)^{\dagger}\left(\frac{dF_j^{\Delta}(a)}{dr_i} - \frac{b}{a}F_j^{\Delta}(a)\right)}{E_k - E}, \tag{2.15}$$

where the integration has been performed over all $N+1$ electron space-spin coordinates, excluding that of the scattering electron. This results in a total wavefunction (from eq. 2.3),

$$|\Psi^{\Delta}\rangle = \frac{1}{2}\sum_{j=1} \frac{\omega_{jk}^{\Delta}(a)^{\dagger}\left(\frac{dF_j^{\Delta}(a)}{dr_i} - \frac{b}{a}F_j^{\Delta}(a)\right)}{E_k - E}|\psi_k^{\Delta}\rangle, \tag{2.16}$$

on the R-matrix boundary ($r = a$), see figure 2.1. Projecting the total wavefunction (eq. 2.16) on to a channel, $|\phi_j^N Y_{l_j}^{m_j}\rangle$, gives the following expression for the reduced radial functions,

$$F_i^{\Delta}(a) = \sum_j R_{ij}^{\Delta}(E)\left(a\frac{dF_j^{\Delta}(a)}{dr_i} - bF_j^{\Delta}(a)\right), \tag{2.17}$$

where the R-matrix on the boundary, $R_{ij}^{\Delta}(E)$, is defined as:

$$R_{ij}^{\Delta}(E) = \frac{1}{2a}\sum_k \frac{\omega_{ik}^{\Delta}(a)\omega_{jk}^{\Delta}(a)}{E_k - E}. \tag{2.18}$$

In practice the constant, b, is normally taken to be zero (Tennyson, 2010). The R-matrix then provides a connection between the reduced radial function and the derivative of the reduced radial function. In the outer region where exchange and correlation effects are ignored it is feasible to compute the reduced radial functions on a grid. The inner region wavefunction on the boundary provides the necessary information to construct and then propagate the R-matrix across the grid to be matched with asymptotic solutions.

2.3 The inner region

The wavefunction in the inner region is constructed using the standard close-coupling expression (Arthurs and Dalgarno, 1960),

$$\begin{aligned}\psi_k^{\Delta}(x_1,\ldots,x_{N+1},R) &= \mathcal{A}\sum_{ij} a_{ijk}^{\Delta}\phi_i^{\Delta}(x_1,\ldots,x_N)u_{ij}(x_{N+1}) \\ &+ \sum_i b_{ik}^{\Delta}\chi_i^{\Delta}(x_1,\ldots,x_{N+1}).\end{aligned} \tag{2.19}$$

for each internuclear separation R. $x_n = r_n\sigma_n$ represent the space and spin coordinates of the n^{th} electron. $\phi_i^{N\Delta}$ is the N-electron target wavefunctions of the i^{th} state. The target wavefunctions are generated by placing a basis of atomic orbitals at the centre of each nuclei. Molecular orbitals are formed by taking linear combinations of the atomic orbitals and then self-consistently optimising the molecular orbitals. The target electrons are placed in the molecular orbitals in different configurations which give a particular molecular spin multiplicity and symmetry. The expansion coefficients of the configurations are determined variationally, this gives the wavefunction of target states of a particular spin multiplicity and symmetry. This is known as a configuration interaction (CI), with the expansion coefficients known as CI coefficients. u_{ij} is an orbital used to represent the j^{th} continuum electron with a partial wave expansion up to some maximum value of ℓ, $\ell_{\max}$, the functions used to describe the continuum will be discussed in more detail in a later section. The first summation describes a situation in which the scattering electron is restricted to only the continuum orbitals and the target electrons restricted to only target orbitals, the configurations that arise are known as 'target + continuum' configurations. χ_i^{Δ} are square-integrable functions that are zero on the R-matrix boundary and are hence known as 'L^2' functions. Their role is to relax the orthogonality between target and continuum (Gillan et al., 1995). The subscript k denotes the k^{th} inner region wavefunction. $\mathcal{A}$ is an antisymmetrisation operator introduced so that the indistinguishable inner-region electrons satisfy the Pauli principle. a_{ijk}^{Δ} and b_{ik}^{Δ} are the coefficients of expansions and are found by diagonalising the operator $H_{N+1} + \mathcal{L}_{N+1}$ in the basis ψ_k^{Δ} for a fixed R in the inner region, that is,

$$\langle \psi_k^{\Delta} | H_{N+1} + \mathcal{L}_{N+1} | \psi_{k'}^{\Delta} \rangle = E_k^{\Delta} \delta_{kk'}. \tag{2.20}$$

2.3.1 Target wavefunctions

The starting point for the construction of the target wavefunctions is selecting a basis set. A basis set is a linear combination of atomic orbitals (LCAO) used to represent the molecular orbitals (MOs). The polyatomic version (Morgan et al., 1998) of the UKRmol codes (Carr et al., 2012) used in this work uses Gaussian type orbitals (GTOs); GTOs provide an approximation of the more accurate Slater type orbitals (STOs), however, GTO integrals are more numerically efficient to compute, this has led to their wide spread use in quantum chemistry calculations. A primitive set of GTOs is written in Cartesian form as,

$$g_j^{lmn} = N_{\ell mn} x^{\ell} y^m z^n e^{-\alpha r^2}, \tag{2.21}$$

N_{lmn} is a normalisation constant. When $\ell + m + n = 0$, the GTO is called an s-type Gaussian, when $\ell + m + n = 1$, p-type, when $\ell + m + n = 2$, d-type and so on. α is known as the orbital exponent which is either optimised variationally or by fitting the GTO to an STO. A basis set is built out of a linear combination of different primitive Gaussians,

$$\phi_i = \sum_j c_{ij} g_j^{\ell mn}, \tag{2.22}$$

centred on the same atom and having different values of α. ϕ_i are known as contracted Gaussians. Sets of contracted Gaussians are better suited to represent inner shell orbitals; this has lead to the development of core-valence basis sets in which a larger number of primitives are used to represent the inner shell than the valence orbitals. Polarization effects brought about by the distortion of the atomic orbitals due to the additional molecular charge density are accounted for by adding primitives of higher ℓ to a contraction. In this work the correlation-consistent polarized valence (cc-pVXZ, where X is D, T, Q, 5, 6) sets of Dunning (1989) were used for all calculations.

Once a basis set has been decided upon the orbitals are optimised using a variational principle. In this study this was carried out using a multiconfiguration self consistent field method or MCSCF. MCSCF is essentially a combination of a self consistent field or SCF calculation and a CI. In an SCF calculation a single Slater determinant is used to describe the ground state of the molecule, orbitals are self-consistently optimised using the Hartree-Fock equations (Levine, 2000). A CI calculation consists of taking a linear combination of Slater determinants to describe the mixing of configurations of electronic states of a molecule, the coefficients of expansion are varied.

In an MCSCF calculation the expansion coefficients of the determinants and the orbitals are optimised simultaneously. A complete active space (CAS) is specified which restricts the configurations included in the expansion by only allowing the electrons to occupy certain orbitals. Generally the CAS is split into two types of orbitals, frozen and active. Frozen orbitals are always occupied and form the base from which all configurations included in expansion are built upon. Electrons are allowed to move between active orbitals and all possible configurations that arise are included in the expansion. In this study the MCSCF calculation was used to provide the contraction coefficients c_{ij} in eq. (2.22).

Using the optimised MOs from the MCSCF a complete active space configuration interaction (CASCI) is performed to find N-electron target wavefunctions. To perform a CI expansion one writes the molecular wavefunction, ψ as a linear combination of configuration state functions (CSFs), ϕ_i,

$$\psi = \sum_i b_i \phi_i. \tag{2.23}$$

The CI expansion only includes CSFs that have the same symmetry properties of the state that is to be calculated by the expansion (denoted by Δ in the previous section). Coefficients b_i are then varied to find the lowest energy given by the wavefunction. Configurations are denoted as being singly, doubly, triply, ..., excited depending on whether 1, 2, 3, ..., electrons are out of the ground state configuration. In reality, including every excitation from the ground state leads to a huge number of CSFs and so is only performed on molecules with a small number of electrons, this is known as a full-CI. To make CI calculations tractable for larger molecules the number of CSFs is truncated using a CAS which restricts the number of CSFs used in the calculation. The choice of CAS is key to the development of any model which seeks to describe the electronic structure of a molecule correctly, see chapter 4.

It should be noted that carrying out an MCSCF calculation is equivalent to using MCSCF optimised orbitals with a CI calculation if the same CSFs are used, but not equivalent to a CI calculation using orbitals optimised using an SCF. The MCSCF orbitals are generated by a program external to the UKRmol suite, MOLPRO (Werner et al., 2010), and hence it is necessary to perform the calculation in this way, that is, MCSCF followed by CI.

2.3.2 Continuum wavefunctions

The inclusion of the scattering electron in the $(N+1)$-electron calculation necessitates the use of continuum orbitals to describe the scattering electron in the continuum. The continuum orbitals are centred on the centre of mass of the molecule. The continuum orbitals must be complete over the required energy range and only span the inner region. In practice this often leads to over-completeness with the wavefunctions used to describe the target and linear dependence issues arise. Linear dependence must be rigorously removed for a successful R-matrix calculation, however if performed too enthusiastically can result in important orbitals missing from the calculation.

Linear dependence errors may only become apparent in the outer region; qualitatively, they can appear as potential energy curves which are not smooth as a function of internuclear separation and eigenphases which are not smooth with increasing electron energy. In the inner region a linear dependence problem can be identified by eigenenergies that are unrealistically low, for example 1000s of Hartree below the target state energies.

Continuum basis functions are represented as,

$$\eta_{ij\ell}(r,\theta,\phi) = f_{ij\ell}(r) Y_{\ell_i m_{\ell_i}}(\theta,\phi), \tag{2.24}$$

and are combined with target orbitals to form continuum orbitals,

$$u_{ij}(r,\theta,\phi) = N_{ij}\left(\sum_{i'j'} c_{iji'j'}\eta_{i'j'} + \sum_{k} d_{ijk}\psi_k(\mathbf{x})\right) \tag{2.25}$$

N_{ij} is a normalisation factor, $\psi_k(\mathbf{x})$, are target orbitals and $c_{iji'j'}$ and d_{ijk} are constants determined by orthogonalisation. The radial functions are found by numerically solving the equation

$$\left(\frac{d^2}{dr^2} - \frac{\ell(\ell+\ell)}{r^2} + 2V_0(r) + {k_i}^2\right) f_{ij\ell} = 0, \tag{2.26}$$

where $f_{ij\ell}$ is represented by fitting Bessel or Coulomb functions with GTOs (Faure et al., 2002) depending on the charge of the target. The continuum functions, $\eta_{ij\ell}$, are Gram-Schmidt orthogonalised (Arfken et al., 2013) to the target orbitals and then the continuum orbitals are orthogonalised using symmetric or Löwden orthogonalisation (Tennyson, 2010).

In practice the continuum orbitals are also used to compute the surface amplitudes rather than the integral given in eq. (2.14):

$$\omega_{ik}^{\Delta}(a) = \sum_{j} u_{ij}(a) a_{ijk}^{\Delta} \tag{2.27}$$

where a_{ijk}^{Δ} are the coefficients of the inner region wavefunction.

2.3.3 L^2 configurations

In the first summation of eq. (2.19) the scattering electron is restricted to only the continuum orbitals. As a result a considerable number of important configurations are neglected, that is, configurations in which the scattering electron enters the target orbitals. To relax the orthogonality between the target and scattering electron extra configurations are added to the second summation in which the scattering electron is allowed to occupy the target orbitals. These configurations appear as the wavefunctions χ_i^{Δ} in eq. (2.19) are are known as the L^2 configurations (Gillan et al., 1995) as they are square integrable and hence zero on the R-matrix sphere.

The size of the $N+1$ calculation, that is the CAS, can be controlled by increasing the number of virtual orbitals used to construct the L^2 configurations. In the R-matrix method the term 'virtual orbitals' is taken to mean the target orbitals not occupied in the N or $N+1$ CAS. These virtual orbitals can either be 'contracted' or 'uncontracted' (Tennyson, 2010). Contracted virtual orbitals are included in the continuum orbitals, whereas uncontracted virtual orbitals are added to the L^2 functions.

When the virtuals orbitals are uncontracted the L^2 functions employed take two different forms; those in which the scattering electron enters the target active space, relaxing the orthogonality between the target and continuum orbitals and those in which scattering electron occupies the additional virtual orbitals introduced in to the $N+1$ CAS. Therefore the uncontracted CAS referred to below can be represented as

$$(1\sigma_g, 1\sigma_u)^4 \ (2\sigma_g, 3\sigma_g, 2\sigma_u, 3\sigma_u, 1\pi_u, 1\pi_g)^{10},$$

the scattering electron entering the active target space, and

$$(1\sigma_g, 1\sigma_u)^4 \ (2\sigma_g, 3\sigma_g, 2\sigma_u, 3\sigma_u, 1\pi_u, 1\pi_g)^9 \ (\text{additional } N+1 \text{ virtuals})^1,$$

the scattering electron occupying the additional virtual orbitals introduced in to the $N+1$ CAS. The choice of which virtual orbitals to include in the L^2 functions requires careful consideration and is integral to model development, see chapter 4 for more details.

2.4 Outer region

In the outer region where $r > a$, a, the R-matrix radius, is chosen so that electron exchange and electron-electron correlation can be neglected. The outer region wavefunction is written as an expansion of channel functions, $\phi_i^n(x_1, \ldots, x_N, \sigma_{N+1})Y_{\ell_i m_{\ell_i}}(\theta, \phi)$,

$$\psi^{N+1} = \sum_{i=1}^{n} \phi_i^n(x_1, \ldots, x_N, \sigma_{N+1})Y_{\ell_i m_{\ell_i}}(\theta, \phi)F_i(r_{N+1}), \tag{2.28}$$

where n runs over all channels, $x_j = r_j\sigma_j$ denotes the position and spin of the j^{th} target electron. ϕ_i^n are formed by coupling a target state to a scattering electron with spin σ_{N+1}. As the scattering electron is now distinct from the target electrons there is no requirement for an antisymmetrisation operator. Additionally, the L^2 functions described in the previous section vanish as there are no longer exchange or correlation effects with the target electrons. It is now possible to use reduced radial functions, $F_i(r_{N+1})$, in a single centred potential to describe the scattering electron. A table is given in appendix

Substituting this wavefunction into the Schrodinger equation (eq. (2.1)) and projecting onto the channel basis functions results in a set of coupled differential equations for the reduced radial functions,

$$\left(\frac{d}{dr^2} - \frac{\ell_i(\ell_i+1)}{r^2} + k_i^2\right) F_i(r) = 2\sum_j V_{ij}F_j(r) \tag{2.29}$$

V_{ij} is the potential matrix describing the coupling between channels i and j, and the wavenumber k^2 is given by,

$$k_i^2 = 2(E - \epsilon_i). \tag{2.30}$$

ϵ_i is the eigenenergy of the target state and E the total energy of the system. The energy of the lowest target state is taken to be zero by convention; if $k^2 \geq 0$ a channel is open and closed if $k^2 < 0$.

The potential matrix is given by,

$$V_{ij} = \langle \phi_i^n Y_{\ell_i m_{\ell_i}} | \sum_{k=1}^{N} \frac{1}{r_{N+1} - r_k} - \sum_{p=1}^{N_{nuclei}} \frac{Z_p}{r_{N+1} - R_p} | \phi_i^n Y_{\ell_i m_{\ell_i}} \rangle. \tag{2.31}$$

As r_{N+1} is always greater than that of the target electron coordinate a multipole expansion can be made resulting in,

$$V_{ij} = \frac{a_{ij}^{\lambda}}{r_{N+1}^{\lambda+1}}. \tag{2.32}$$

For a charged target, such as N_2^+, $\lambda = 0$. The coefficients of expansion dictate the coupling between the channels through Clebsch-Gordan coefficients (Tennyson, 2010).

The set of equations given in eq. (2.29) are solved by propagating the R-matrix (Baluja et al., 1982; Morgan, 1984) to the asymptotic region. Asymptotic expansion techniques (Gailitis, 1976; Noble and Nesbet, 1984) are then used to find solutions to linear combinations of reduced radial functions that satisfy the boundary conditions imposed by

$$F_{ij} \sim \frac{1}{\sqrt{k_i}}(\sin\theta_i\delta_{ij} + \cos\theta_i K_{ij}) \tag{2.33}$$

for open channels, where $\sim$ denotes an asymptotic solution, and

$$\begin{aligned}
\theta_i &= k_i\ell_i - \frac{1}{2}\ell_i\pi - \eta_i \ln 2k_i r + \sigma_{\ell i} && (2.34)\\
\eta_i &= -\frac{Z-N}{k_i} && (2.35)\\
\sigma_{li} &= \arg\Gamma(\ell_i + 1 + i\eta_i). && (2.36)
\end{aligned}$$

$$F_{ij} \sim 0 \tag{2.37}$$

for closed channels. Eq. (2.33) is the general case for an ion, for neutral molecules η_i and σ_{li}, which come about due to the Coulomb potential, are zero.

K_{ij} is the known as K-matrix and has dimensions $n_\mathrm{o} \times n_\mathrm{o}$ where n_o is an open channel; scattering observables are then calculated from the K-matrix which can be transformed into the scattering matrix, or S-matrix, by

$$\mathbf{S} = \frac{1 + i\mathbf{K}}{1 - i\mathbf{K}}. \tag{2.38}$$

2.4.1 Bound states

It is possible to use an R-matrix calculation to find bound states of the target. There are two methods currently implemented in the UKRmol code. The first method, known as quantum chemistry (QC) mode, is to completely ignore the outer region and treat the $(N+1)$-electron calculation as a standard bound state electronic structure calculation. This is achieved by not correcting the integrals for the GTO tails (Morgan et al., 1997), which go beyond the inner region boundary, allowing the target plus continuum orbital set to span an extended region. The Bloch operator is removed from eq. (2.20) and the standard $N+1$ Hamiltonian (eq. (2.2)) is diagnolised to find bound state energies. Whilst this method is sufficient for low lying valence states, diffuse states with larger orbital radii, such as Rydberg states, will not be detected as no R-matrix propagation as taken place, see chapter 4.

The second method solves this issue by taking outer region functions which tend to zero at infinity (see eq. (2.37)), that is, bound states and integrating the solution inwards to the R-matrix sphere. The solutions are then matched to the inner region solutions on the boundary.

In the inner region the total $(N+1)$-electron wavefunction can be expanded as,

$$\Psi = \sum_k C_k \psi_k^{N+1}, \tag{2.39}$$

where C_k are known as bound state coefficients. The matching condition on the the R-matrix boundary is

$$F_i = \sum_j P_{ij} X_j \tag{2.40}$$

and

$$\frac{dF_i}{dr} = \sum_j \frac{dP_{ij}}{dr} X_j \tag{2.41}$$

where F_i are reduced radial functions as in eq. (2.13), P_{ij} is an outer region function as in eq. (2.33). X_j is a column vector which is used to construct the bound state coefficients which are given by the equation,

$$C_k = \sum_i \frac{\omega_{ik}}{2(E_k - E)} \sum_j \left(\frac{dP_{ij}}{dr} - bP_{ij} \right) X_j. \tag{2.42}$$

combining eqs. (2.40) and (2.41) with the expression for reduced radial functions on the R-matrix boundary, eq. (2.17), one arrives at the matching condition:

$$\sum_j B_{ij} X_j = \sum_j \left(P_{ij} - \sum_k R_{ik}(E) \left[\frac{dP_{kj}}{dr} - bP_{kj} \right] \right) X_j = 0 \tag{2.43}$$

this equation (2.43) has the form of an eigenvalue equation and hence will have solutions when the determinant of B_{ij} is equal to zero. These zeroes appear at the energies of the bound states.

Issues arise at energies close to R-matrix pole energies, E_k. At these energies the R-matrix and resultantly the matrix B_{ij} are undefined. These poles can be eliminated from B_{ij} using a method outlined by Burke and Seaton (1984).

Bound state searching is implemented in the UKRmol codes in the module BOUND. Zeroes in the determinant are found by searching a grid of the effective quantum number, ν, given by,

$$\mu = n - \nu, \tag{2.44}$$

where n is the principal quantum number and μ the quantum defect. An initial estimate E_e of the bound state energy is found using a Newton-Raphson search. A Taylor series expansion is then used to set up the eigenvalue equation,

$$\sum_j B_{ij} X_j = \sum_j \left(B_{ij}(E_e) + (E_t - E_e) \frac{dB(E_e)_{ij}}{dE} \right) X_j = 0, \tag{2.45}$$

which is then applied recursively until the change in energy between estimated value, E_e, and true value, E_t, is below a certain threshold.

When the module was originally developed (Branchett, 1991; Sarpal et al., 1991; Rabadán and Tennyson, 1996) calculating the determinant on a dense grid took considerably longer than it does with modern computers. Therefore, for the case of ions, a dense grid was only used around integer values of n where there were likely to be many bound states. A sparse grid was used in between these regions. Additionally, to stop the module searching in regions where bound Rydberg states could not exist, the calculation was started at the lowest value of n allowed by ℓ for each molecular symmetry. The processing power of modern day computers means that it is now possible to simply calculate the effective quantum number on a dense grid for the whole range; as a result the non-linear grid and starting the search at the lowest allowed value of n were not used in this study. Indeed, it was found that strongly bound states which did not have Rydberg-like quantum defect behaviour were being ignored by the program.

Calculations using the module BOUND and QC mode are described in chapter 4.

2.4.2 Resonances

Resonances lead to large variations in the cross-sections of electron scattering processes and need to be treated carefully if these processes are to be described correctly. From a classical perspective a resonance can simply be thought of as an electron which is temporarily captured by the target, performs a few orbits and is then released. In formal scattering theory a resonance is a pole in the complex S-matrix, which has a non-zero real and imaginary part. The real and imaginary parts of the pole form the energetic position and autoionisation half-width of the resonance with the following form

$$E = E^{\mathrm{r}} - i\frac{\Gamma}{2} \tag{2.46}$$

where E is a complex energy, E^{r} is the resonance position and Γ is the autoionisation width. To elucidate the meaning of the autoionisation width it is useful to consider the probability of state that can be written as,

$$|\Psi(r,t)|^2 = \left|\Phi(r)e^{-iEt/\hbar}\right|^2 = |\Phi(r)|^2, \tag{2.47}$$

if E is real. However if E is complex like in eq. (2.46),

$$|\Psi(r,t)|^2 = \left|\Phi(r)e^{-i(E^{\mathrm{r}}-i\Gamma/2)t/\hbar}\right|^2 = |\Phi(r)|^2 e^{-\Gamma t/\hbar}, \tag{2.48}$$

meaning that a resonant state has a lifetime the length of which is dictated by the autoionisation width and is not a stationary state of the Hamiltonian of the system (Larsson and Orel, 2008).

There are three types of resonances common to electron-molecule scattering; shape resonances, Feshbach resonances and nuclear-excited Feshbach resonances.

A shape resonance (Schulz, 1973) occurs when an electron becomes trapped behind a centrifugal barrier in the electron-molecule potential; as the barrier is dependent on ℓ, s-wave scattering cannot lead to shape resonances. From a chemical perspective, a shape resonance is a situation in which the scattering electron occupies the lowest unoccupied molecular orbital. Shape resonances are often short lived and usually appear as broad features as a function of energy.

Feshbach resonances (Feshbach, 1958, 1962) occur when the scattering electron also excites the target molecule leading to a double excitation of the target molecule. The target molecule is excited into a configuration which is not its ground state, known as the parent state, and the scattering electron is temporarily captured into an unoccupied virtual orbital. At the end of the resonance's lifetime the state decays to the parent state. Feschbach resonances are prevalent in ionic targets and generally take the form of Rydberg states, there are however also valence states embedded in the continuum which appear as Feshbach resonances. These resonant valence states can become bound with increasing internuclear separation; capture into a Feshbach resonance state which becomes bound is the process which is integral to the direct mechanism of dissociative recombination, see section 1.2.1 of chapter 1.

Nuclear-excited Feschbach resonances (Morgan et al., 1990) can only occur in molecules and in general occur when there is a weakly bound state just below the ionisation threshold of the molecule. The electron collision excites the molecule to a high vibrational level in the weakly bound state. Resonances of this type are responsible for the indirect process in dissociative recombination, see section 1.2.1 of chapter 1.

There are a number of ways of finding the resonance position and widths (Sochi and Storey, 2013). The most commonly used method is fitting the eigenphase sum. The eigenphase sum is calculated directly from the diagonalised K-matrix,

$$\delta(E) = \sum_i \arctan(K(E)^D_{ii}). \tag{2.49}$$

Resonances appear as rapid increase in π radians and are fitted with the Breit-Wigner form,

$$\delta(E) = \delta_0(E) + \arctan\frac{\Gamma}{2(E^r - E)}, \tag{2.50}$$

This form is explicitly appropriate for a single, isolated resonance. Eigenphases are not suitable to be fitted when there are many overlapping or closely spaced resonances. See chapters 3 and 5. Fitting the eigenphase sum is implemented in the UKRmol code suite in the program RESON (Tennyson and Noble, 1984). RESON scans $\delta(E)$ for points in which there is a change in sign of the numerically computed second derivative $\frac{d^2E}{d\delta^2}$. A new finer grid is constructed around the point of inflection and fitted with the Breit-Wigner form.

An alternative method of detecting and fitting resonances is the time-delay method of Smith (1960). The time-delay matrix, Q, given by

$$\mathbf{Q} = -i\hbar\mathbf{S}^* \frac{d\mathbf{S}}{dE}. \tag{2.51}$$

is calculated as a function of energy. Resonances appear as Lorentzians when plotted against energy. The time-delay method is more suitable for fitting the close-spaced and overlapping resonances which are common in charged targets. The time-delay method is implemented in the UKRmol codes in the module TIMEDEL (Stibbe and Tennyson, 1998).

Finally there is the R-matrix specific resonance characterisation procedure, the 'QB' method of Quigley and Berrington (Quigley and Berrington, 1996; Quigley et al., 1998). This method was originally developed for charged atomic targets and is based on the neglect of the outer region potential. These potentials are significantly stronger in molecular ions so the QB method is not necessarily as accurate for molecules. In favourable circumstances the QB method should produce results similar to that of RESON and TIMEDEL (Ballance et al., 1998). The QB method benefits from the fact that it is analytic and does not suffer from the numerical problems of the two methods mentioned above.

These three methods of detecting and fitting resonances will be discussed in detail in chapters 3 and 5.

2.5 The UK R-matrix molecular codes

All of the R-matrix calculations described in this thesis were carried out using the polyatomic UK R-matrix molecular codes (UKRmol) (Carr et al., 2012). The codes are a series of modules which, when run in the correct order perform a full electron-molecule scattering calculation. The UKRmol codes are split into two sections, UKRmol-in and UKRmol-out. UKRmol-in contains the programs necessary to perform the target and inner region calculations and are compiled as separate modules which are run in turn. UKRmol-out contains modules necessary to run the outer region part of the calculation. UKRmol-out modules are written as subroutines which are then called in turn from a single executable; this makes the sharing of routines between modules more practical.

The actual R-matrix calculation is split up into three separate stages: target, inner and outer.

The target and inner calculations require modules to be run in a specific order, most R-matrix calculations are identical up to the outer region in terms of the modules that are required to be executed. In the outer region the user selects which modules they will run depending on which scattering properties they wish to calculate. Flow charts in figs. 2.3, 2.4 and 2.5 show the structure of the codes for each stage of the calculation.

2.5.1 Target calculation

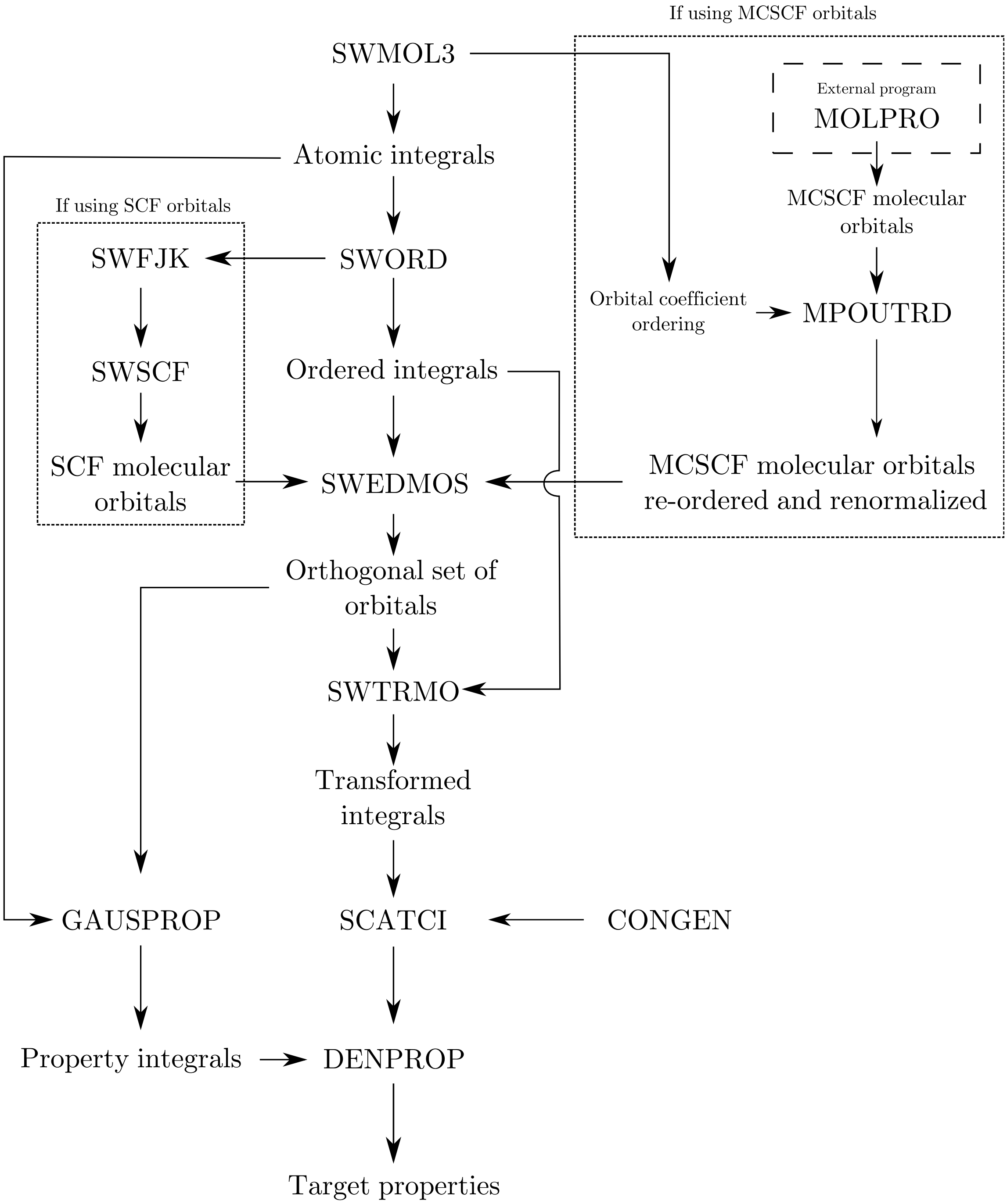

Figure 2.3: Flow chart showing the modules used in the target stage of an R-matrix calculation using the UKRmol codes.

SWMOL3 performs one and two-electron integrals using the GTO basis set specified by the user.

This is also the point at which the positions of the nuclei which make up the molecule are specified.

SWORD orders the integrals calculated by SWMOL3.

The default option in the UKRmol codes is to use SCF orbitals. If the user wishes to use SCF orbitals the following modules are run:

SWFJK forms combinations of Coulomb and exchange integrals for the Fock matrix used in the SCF calculation.

SWSCF Performs a SCF calculation to optimise molecular orbitals.

If the user wishes to use MCSCF orbitals the following package and module are run:

MOLPRO MOLPRO (Werner et al., 2010) is a commercial quantum chemistry package which is not part of the UKRmol codes and is used to calculate the MCSCF orbitals. The same basis set and geometry information as for SWMOL3 is input and molecular orbital coefficients are produced.

MPOUTRD takes the orbitals from the MOLPRO output file and the molecular orbital coefficient ordering from SWMOL3 and reorders and renormalises the molecular orbitals for use in the UKRmol codes. An input is produced for SWEDMOS.

SWEDMOS produces a set orthonormal molecular orbitals using the atomic basis sets specified in SWMOL3 and the molecular orbitals produced by either SWSCF or MOLPRO.

SWTRMO transforms the set of integrals over atomic orbitals produced by SWMOL3 to a set of integrals over the molecular orbitals produced by SWEDMOS.

CONGEN creates configuration state functions (CSFs) for the target CI expansion. This is where the user specifies the target CAS to be used and the frozen and active electrons.

SCATCI constructs and diagonalises the target molecular Hamiltonian using the CSFs generated by CONGEN and integrals transformed by SWTRMO. The CI coefficients and corresponding energy eigenvalues are calculated.

GAUSPROP calculates the molecular property integrals required by DENPROP.

DENPROP finds the transition density matrix from the target states calculated by SCATCI and uses it to calculate the multipole transition moments required in the outer region.

2.5.2 Inner region calculation

SWMOL3 performs one and two-electron integrals using the GTO basis set specified by the user but this time including the continuum orbitals.

GAUSTAIL; as SWMOL3 performs integrals over all space it is necessary to subtract the tails of the Gaussians which protrude out of the R-matrix sphere. These tail integrals are calculated by GAUSTAIL (Morgan et al., 1997). This is also the point where the size of the R-matrix sphere

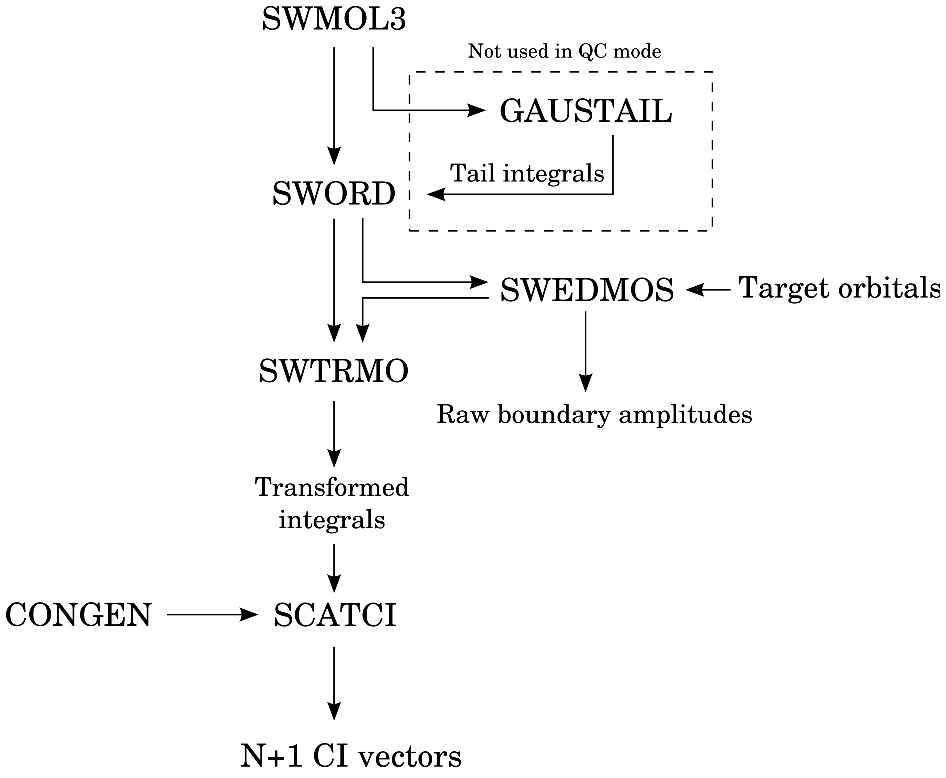

Figure 2.4: Flow chart showing the modules used in the inner region stage of an R-matrix calculation using the UKRmol codes.

is first specified. When running the R-matrix codes in quantum chemistry mode this module is ignored as the spatial restriction of the R-matrix sphere is removed.

SWORD orders the integrals from SWMOL3 and subtracts the tail integrals produced by GAUSTAIL.

SWEDMOS orthogonalises the molecular orbitals this time including the continuum orbitals. As the orthogonalisation is a numerical procedure linear dependent orbitals have small but not zero eigenvalues in the overlap matrix. A deletion threshold is set (normally 10^{-7}) for which any eigenvalue below is considered to belong to a linearly dependent continuum orbital and is deleted. SWEDMOS also calculates the boundary amplitudes of the continuum orbitals often referred to as the 'raw' boundary amplitudes.

SWTRMO performs the same function as in the target calculation.

CONGEN Generates CSFs for the inner region CI calculation. This is where user can specify the L^2 configurations to be used in the inner region wavefunction.

SCATCI constructs and diagonalises the $N+1$ inner region Hamiltonian using a specially adapted algorithm (Tennyson, 1996). The eigenenergies computed at this point are the R-matrix poles in eq. (2.18). In QC mode this is the end of the calculation and the final eigenenergies are used to construct potential energy curves.

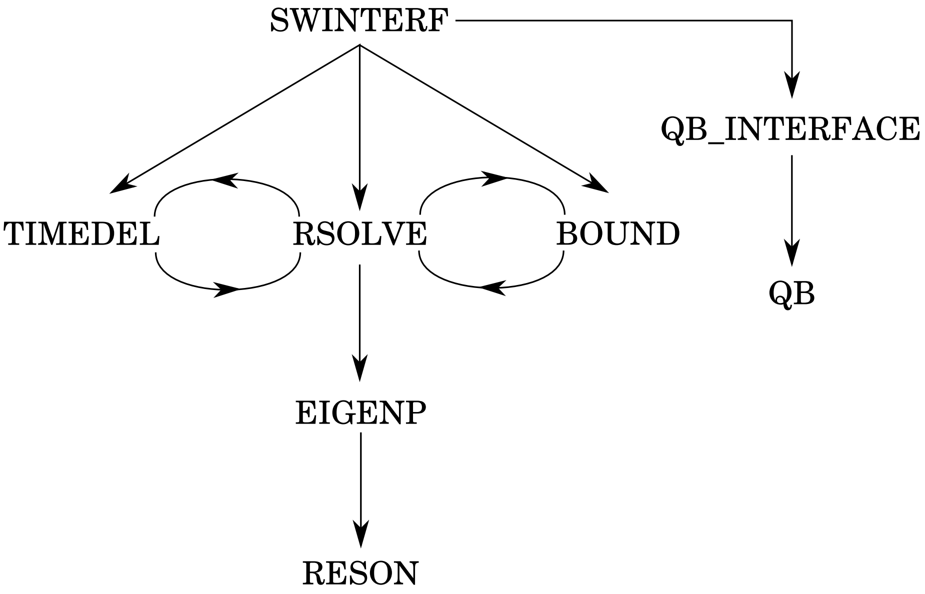

Figure 2.5: Flow chart showing the modules used in this work in the outer region stage of an R-matrix calculation using the UKRmol codes.

2.5.3 Outer region calculation

SWINTERF provides the interface between the inner and outer regions of the code. Taking the $N+1$ eigenpairs, target properties and boundary it produces the data required to construct the R-matrix on the R-matrix sphere.

RSOLVE constructs the R-matrix on the boundary and propagates it to a distance set by the user. It then performs an asymptotic expansion and the results are matched to asymptotic scattering solutions. K-matrices are calculated on an energy gird set by the user. Once the K-matrices have been calculated a number of different modules can be used to calculate scattering observables.

BOUND searches for bound states using a non-linear quantum defect grid using the method described in the previous section. BOUND can be run immediately after SWINTERF as it calls RSOLVE internally.

TIMEDEL calculates the time-delay matrix on an adaptive energy grid then searches for resonances and fits them. As the grid is adaptive, TIMEDEL calls routines from RSOLVE to calculate K-matrices at specific energies and can be run immediately after SWINTERF. TIMEDEL is described in detail in chapter 3.

EIGENP calculates the eigenphase sum using the K-matrices produced by RSOLVE.

RESON automatically searches and fits resonances in the eigenphase sum. A more in depth description of RESON is given in chapter 5.

QB_INTERFACE transforms the files produced by SWINTERF to be used by the atomic code based module QB.

QB calculates resonances using the QB method of Quigley and Berrington (1996). A more in depth description of QB is given in chapter 5.

2.6 Contributions to UKRmol codes

All updates to the UKRmol codes discussed in this thesis have been uploaded to the CCPForge repository accessible at `http://ccpforge.cse.rl.ac.uk/gf/project/ukrmol-in/`.

2.6.1 STATESKIP

In the current implementation of UKRmol all target states included in the target and inner region calculations are by default included in the outer region calculation. The result of this is that, if one desires to use many target states in the inner region, all of these states must then be included in the outer region calculation as well. This results in a large number of channels most of which are strongly closed, these channels lead to increased numerical instability and a significant slowing of the outer region calculation.

Therefore a subroutine was developed for SWINTERF, ‘STATESKIP’ which automatically skips the target states which the user does not require in the outer region calculation. The routine works by using the input parameter `nvo`; `nvo` stands for ‘number of virtual orbitals’ and is set in the outer region if using contracted virtual orbitals (see section 2.3.3). As `nvo` is essentially just an orbital counter, by setting it to the correct value it can be used to skip the continuum orbitals for entire target states. A new input parameter, `ntarg0`, was created so that a user could specify the number of target states which they wished to use in outer region. SWINTERF then returns the new inputs needed to re-run SWINTERF with a reduced number of target states. The rest of the outer region calculation can then be performed. A detailed description of the workings of the subroutine is given in appendix B.

2.6.2 BOUND

The module BOUND, see section 2.4.1, was updated to work with the latest version of RSOLVE. This largely involved updating calls to subroutines which had been adjusted in RSOLVE for the partitioned R-matrix method (Tennyson, 2004).

As mentioned in section 2.4.1, the module was adjusted so that when calculating bound states of an ion it always used a dense quantum defect grid. Additionally, the module was adjusted so that it always started to search for bound states below the lowest pole of the R-matrix as it was found that it was missing low-lying states that did not have Rydberg-like quantum defect characteristics, again see section 2.4.1).

2.6.3 TIMEDEL

A substantial amount of work was performed on the module TIMEDEL to rewrite its fitting method to include additional eigenvalues of the time-delay matrix. These improvements are discussed in detail in chapter 3.

2.6.4 Automating R-matrix calculations

Changing the inputs of the UKRmol codes is not a trivial task. Each module has a namelist input file which varies between a single line, to around 200 lines, long. Modules which must be run separately for each molecular symmetry each require an individual input file for each symmetry. Many of the inputs are now defunct but are still required to be input correctly for the codes to run. The development of Quantemol-N (Tennyson et al., 2007), which is a graphical user interface with the UKRmol codes has accelerated the speed with which R-matrix calculations can be performed. Quantemol-N generates a set of inputs systematically (which was originally done by hand) using Java scripts which can then form the basis for an R-matrix calculation. The original inputs for UKRmol codes for this work were taken from Quantemol-N and then changed by hand during model development.

The inputs then need to be run outside Quantemol-N, this involved developing sophisticated bash scripts (http://www.gnu.org/software/bash/) to automatically run the UKRmol codes. Calculations were performed on a dense grid of internuclear separations (see chapters 4 and 5); although some inputs are independent of internuclear separation, many need to be adjusted for each grid point; changing the inputs by hand for 1199 internuclear separations per molecular symmetry (of which there were 12) was intractable and subject to a significant amount of human error. Therefore bash scripts were developed which completely automated the process. The bash scripts also exploited the use of machines with multiple processors so that many internuclear separations could be calculated in parallel.

Chapter 3

Resonance detection and fitting with TIMEDEL

3.1 Introduction

This chapter gives a description of resonance detection and fitting using the time-delay method as implemented in the module TIMEDEL. The original module written by Stibbe and Tennyson (1998) was updated for this work to improve the fitting of overlapping resonances. A description of the update and the improved fitting method is given below.

The time-delay method was originally proposed by Smith (1960) as an alternative method of characterising resonances to the *de facto* fitting of the eigenphase sum. In classical terms the time-delay can be thought of as the difference in time an electron experiences with or without an interaction with the target. The time-delay matrix is formed from the scattering matrix, $\mathbf{S}$, and the time operator, $-i\hbar\frac{d}{dE}$:

$$\mathbf{Q} = -i\hbar\mathbf{S}^*\frac{d\mathbf{S}}{dE}, \tag{3.1}$$

and has dimensions $n_o \times n_o$ where n_o is the number of open channels. By diagonalising the time-delay matrix eigenvalues, q_i, and eigenvectors, $|\psi_{q_i}\rangle$ can be found, that is,

$$\mathbf{Q}|\psi_{q_i}\rangle = q_i|\psi_{q_i}\rangle. \tag{3.2}$$

The largest eigenvalue of $\mathbf{Q}$, q_1, represents the longest time-delay of the incident electron. If q_1 is plotted against energy, resonances appear as Lorentzians which can be fitted for position and width. Smith also showed that it was possible to calculate the branching ratios β_i, the probability of decay into a different asymptotic channel, using the square of the eigenvector associated with q_i, that is,

$$\beta_i = |\langle\psi_{q_i}|\psi_{q_i}\rangle|^2. \tag{3.3}$$

This method has come under scrutiny recently (Shimamura et al., 2006; Shimamura, 2011, 2012) and has been applied successfully to a number a systems with many overlapping resonances (Rabadán et al., 1998; Baccarelli et al., 2009; Masin and Gorfinkiel, 2012).

Resonance detection and fitting is complicated in charged targets such as N_2^+, as there are often many resonances associated with the Rydberg states of the excited states of the ion which overlap considerably with each other and valence states. Resonances in an eigenphase sum have a Breit-Wigner form (Hazi, 1979), which has the appearance of an arctan function. Separating the behaviour of resonances of this form becomes increasingly difficult as their width and energy separation decreases, see figure 5.2, chapter 5. The Lorentzian form of resonances in a time-delay means that isolating a single resonance out of many overlapping resonances is greatly simplified. Multiple eigenvalues of the time-delay matrix can be used so that resonances can be tracked as they move from being the longest time-delay (the largest eigenvalue) to the shortest (the smallest eigenvalue). Indeed, this is the principal on which the newly developed fitting method was based. Additionally, the fitting of the time-delay removes the majority of the background which can be significant in molecular problems with many channels.

3.2 Implementation in the UKRMol code suite

The time-delay method was originally implemented in the R-matrix method by Stibbe and Tennyson (1996) using the module TIMEDEL (Stibbe and Tennyson, 1998). TIMEDEL is an outer region module and follows SWINTERF. The module has to two distinct sections; the first computes the time-delay matrix over a given energy range and requires the input of K-matrices, the second fits the computed time-delay matrix for position and width and finds branching ratios. In this study the fitting section was rewritten, the first section was altered to automatically handle thresholds if the threshold energies are provided. Additionally a number of compatibility issues with a new version of RSOLVE were solved. The NAG (Numerical Algorithms Group, www.nag.co.uk) routines used in the original codes were replaced with LAPACK routines (Anderson et al., 1999) by Natalia Vinci. A description of the workings of the updated code follows.

Initially an energy range is defined for which the time-delay will be computed and fitted. This energy range is split up into energy ranges within thresholds. This is important for ionic targets due to issues that arise when the calculation approaches a threshold. As there are an infinite number of Rydberg states converging on each threshold of the ion, the calculation will never 'reach' the threshold itself if a cut-off energy is not defined. Additionally, close to the threshold the width of the Rydberg states becomes increasingly narrow, this is an issue as the time-delay matrix is calculated using a numerical derivative with respect to the energy. There will come a point at which the width of the resonance is smaller than the energy gap with which the numerical derivative is calculated. Therefore to avoid these issues a maximum principle quantum number is set (default $n = 10$) at which the calculation stops before it reaches the threshold. The calculation then restarts above the next threshold. Above a threshold an electron leaves the resonance with very little kinetic energy; the time-delay of an electron with zero kinetic energy is infinite. This presents a problem for finding the time-delay just above a threshold. Therefore the time-delay calculation is started at some energy above a threshold (default 0.05 eV) where this is no longer an issue. The time-delay is found for each threshold energy range and then fitted. The calculation is stopped when it reaches the final energy of the overall range to be calculated.

The time-delay matrix $\mathbf{Q}$ is found using a numerical derivative of the S-matrix, see eq. (3.1). The S-matrix is found from the K-matrix by the way of

$$\mathbf{S} = \frac{1 + i\mathbf{K}}{1 - i\mathbf{K}}. \tag{3.4}$$

K-matrices are calculated using routines from the UKRMol module RSOLVE, as described in chapter 2. For each energy, E, at which $\mathbf{Q}$ is to be calculated routines from RSOLVE are called to return a K-matrix at energies $E + dE$ and $E - dE$ where dE is at most 10^{-5} eV, tests showed that this gave smooth time-delays for each threshold energy range. The derivative of the S-matrix with respect to energy is found using the K-matrices and is multiplied by the complex conjugate of the average of the two S-matrices to find $\mathbf{Q}$, see eq. (3.1). Only the eigenvalues of $\mathbf{Q}$ are saved at this point; the eigenvectors are recalculated in the fitting process to find branching ratios once the position of a resonance has been determined. An adaptive grid of energies is used across each range. The energy separation of each grid point is proportional to the inverse of the time-delay; the narrowest resonances therefore have the highest density of points and areas where there are no resonances are skipped over. The grid is limited by default to having a minimum spacing of 10^{-15} Ryd.

Once the eigenvalues have been found over an entire threshold range the module enters the fitting routine. Multiple resonances appear as interspersed Lorentzians in the highest eigenvalue, see figure 3.1.

Discontinuities occur when the length of the time-delay of one resonance overtakes that of another; the eigenvalues associated with each resonance switch. Consequently, if only the first eigenvalue is fitted, information is lost when a resonance becomes the second and third eigenvalue. An example of this is given in figure 3.1. The original version of TIMEDEL (Stibbe and Tennyson, 1998) only fitted the longest eigenvalue, this eigenvalue is plotted against energy in panel (a) of figure 3.1. Only two resonances, one at $\sim$ 0.527 eV and another at $\sim$ 0.595 eV, are completely apparent. Another resonance at $\sim$ 0.52725 eV is partially obscured by the resonance at $\sim$ 0.527 eV. If the second and third eigenvalues are included then structure of the wider resonances obscured by the narrow resonance $\sim$ 0.527 eV is elucidated. Although this extra information is often unnecessary as Lorentzians are symmetric functions, it becomes important when the peak of the resonance is

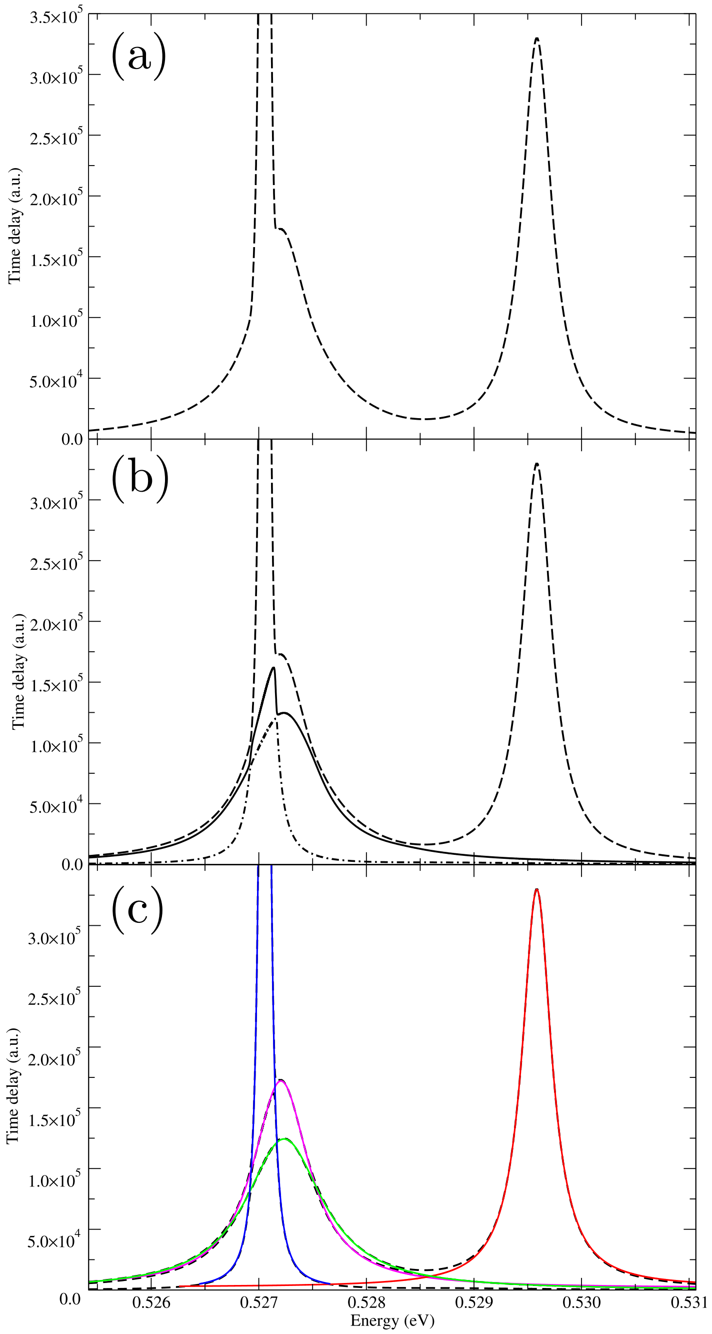

Figure 3.1: An example of fitting overlapping resonances using multiple eigenvalues. The original version of TIMEDEL only fitted the longest eigenvalue (dashed line) of the time-delay matrix, this eigenvalue is plotted against energy in panel (a). If the second (solid line) and third (dashed-dot line) longest eigenvalues are included, as shown in panel (b), it becomes clear that a significant amount information is being ignored if only the longest eigenvalue is fitted. That is, the green and magenta resonances shown in panel (c) would have been badly fitted or missed entirely.

in one of the lower eigenvalues.

Indeed, this development reveals resonances that would have been previously left completely unidentified, those which have a similar position and marginally larger width to that of another resonance. Finding these resonances becomes particularly important when working in a lower symmetry group to that of the molecule being studied; resonances that appear in the same (lower) symmetry group but actually have different symmetries may be obscured by one another. The peak of a resonance of this type is within the second eigenvalue and only the tails switch into the first eigenvalue, for example the magenta resonance shown in panel (c) of figure 3.1.

A new subroutine, EIGSORT, was written to track the resonances as they switched between eigenvalues by finding avoided crossings. Avoided crossing are detected as a minimum in the difference between two eigenvalues. When a minimum is detected the eigenvalues associated with each resonance are switched. Resonances are detected by searching for maxima, checks are performed to ensure the maximum is the peak of a resonance and not a discontinuity left by the EIGSORT routine or a numerical noise. Fitting limits are set by a change in sign of the derivative $\frac{dq}{dE}$ on either side of the resonance peak. The resonances are then fitted with the form:

$$q(E) = \frac{\Gamma}{\left(E - E^r\right)^2 + \left(\Gamma/2\right)^2} + \mathrm{bg}(E). \tag{3.5}$$

where $q(E)$ is the sorted time-delay eigenvalue to be fitted, Γ is the width and $\mathrm{bg}(E)$ is the background. If the fitted peak of the resonance is outside the fitting limits then it is clear that this is false detection or a bad fit and the fit is ignored. Panel (c) of figure 3.1 gives an example of fitting the sorted eigenvalues. Although this method is subject to occasional false detections, extensive testing on N_2^+ showed that it was robust and produced excellent fits. When the position of a resonance has been determined the time-delay matrix is recomputed at this energy and the branching ratios are found by computing the square of the eigenvectors. The branching ratio gives the probability of the autoionisation of the resonant electron to a specific partial wave associated with an electronic state of the ion. Having autoionisation widths resolved in this way is necessary for a dissociative recombination cross-section calculation which includes core-excited bound states, see chapter 6.

Extending the fitting method in this way is a similar concept as that introduced by Shimamura et al. (2006). In their approach resonances are parametrised by a mixing parameter β which describes the level of avoidance between two eigenvalues of $\mathbf{Q}$. An expression is then derived to fit these two resonances as they overlap with each other. The method described here differs in that it is purely numerical and an expression was not formally derived to describe overlapping resonances. The fitting routine simply searches for minima in the difference between the eigenvalues and switches when one is found.

3.3 Program structure and documentation

The structure of TIMEDEL is shown in figure 3.2. It should be noted that the current implementation of the program only works within the UKRmol code suite and requires the additional module K_ADAPT. This module is essentially a stripped down version of RSOLVE and contains the necessary routines to set up the K-matrix calculation (SETUPKMAT, see figure 3.2) and calculate the K-matrices at the energies required by the adaptive grid (GETKMAT, see figure 3.2). This module also reads in the target state energies used to calculate thresholds. K_ADAPT requires the RSOLVE namelist RSLVIN to run. The namelist should be placed after the TIMEDEL namelist TIME in the input file (logical unit 5).

The program starts by reading in the namelist TIME (see description of inputs below), the user is required to input an initial and final energy; all other inputs have default values. The K-matrix calculation is then set up by the subroutine SETUPKMAT by reading in the target and channel dataset (by default fort.10) and the R-matrix poles, amplitudes and the multipole expansion of asymptotic potentials (by default fort.21). TIMEDEL then finds threshold energy ranges using the target state energies. The time-delay calculation then begins with the first energy point in the first threshold.

The first set of K-matrices are calculated by passing the first two energy values ($E + dE$ and $E - dE$, see previous section) to the subroutine GETKMAT, which returns two K-matrices. FINDTIMEDEL takes the K-matrices and passes them to the subroutine KTOSMAT which converts them to S-matrices (see eq. (3.4)) using the LAPACK routine ZGESV. Using the S-matrices the subroutine TIMED then finds and diagonalises the time-delay matrix (see eq. (3.1)) using the LAPACK routine ZHEEV. The first five eigenvalues (or n_{o} if $n_{\mathrm{o}} < 5$) are stored. The program then recalculates the grid-spacing based on the size of the longest time-delay (the first eigenvalue) using an inversely proportional relationship and moves on to the next energy point. Once all the energy grid points have been found for the given threshold energy range, all of the eigenvalues (five or n_{o} per point) are passed to the subroutine EIGSORT. EIGSORT tracks resonances as they move through different eigenvalues by switching every time an avoided crossing is detected (see figure 3.1). Once the eigenvalues are sorted they are passed to DISCONRM which removes discontinuities left by the sorting process by replacing them with a linear interpolant, this reduces the number of false resonance detections.

The eigenvalues are now ready to be fitted and are passed to the fitting subroutine FITTING. By default TIMEDEL considers the first three eigenvalues for fitting; testing showed this to be sufficient. The number of eigenvalues can be increased to five or n_{o} (if $n_{\mathrm{o}} < 5$) but this should not be necessary. FITTING searches the sorted eigenvalues for maxima and performs a number of checks to ensure that the maxima is not numerical noise or an artefact left by EIGSORT. The position of the maxima is then passed to FOUNDRES. FOUNDRES finds fitting limits by looking for a change in sign of the gradient either side of the maxima; FITLORS then fits the resonance with the form given in eq. (3.5) using the LAPACK routine LMDIF1. The branching ratios are then found at the fitted resonance position using GETKMAT and FINDTIMEDEL. Once the FITTING subroutine has completed, TIMEDEL moves onto the next threshold. When all thresholds have been calculated the program ends.

3.3.1 Input data

The input for TIMEDEL is provided as the namelist TIME. Below is a description of each of the input parameters. It should be noted that many of the namelist inputs from the first iteration of the code (Stibbe and Tennyson, 1998) are now defunct and should be ignored.

The format of the following is, name [default (left empty for no default)]: description.

einit [ ]: The initial energy of the calculation.

efinal [ ]: The final energy of the calculation.

gridinit [0.1]: Initial grid spacing.

ieunit [2]: Units used for all input energies. 0=Hartree, 1=Rydberg, 2=eV.

delemax [10^{-5}]: Maximum allowed value of dE.

savekmt [TRUE]: Toggle to output calculated K-matrices.

lukmt [20]: Logical unit for output of K-matrices.

neig [3]: Number of eigenvalues considered for fitting (maximum 5).

lutd [40]: Logical unit for output of time-delays. Fist eigenvalue is outputted to lutd, second to lutd+1, third to lutd+2, and so on.

maxn [10]: Maximum principle quantum number, n, of a Rybderg series to be calculated. This parameter controls the cut-off before reaching a threshold.

epsab [0.05]: Energy above a threshold at which the calculation will be restarted.

3.4 Conclusion

The inclusion of additional eigenvalues in the resonance fitting process results in a method of detecting and fitting resonances which can deal with complex overlapping resonances, such as those prevalent in ionic targets. There are, however, some drawbacks to the time-delay method as implemented here. That is, there is no option but to scan an energy range to find the resonance positions and then only calculate the necessary points; the time-delay is simply calculated for a continuous range of energies to correctly locate and characterise the resonances. As a result, when compared to fitting eigenphase sums as implemented in the program RESON (Tennyson and Noble, 1984), it is significantly more computationally expensive. However, if one is only interested in a particular dissociative curve the eigenphase sum can be quickly scanned at a number of internuclear separations to determine positions which can then be fitted to 'guide' a time-delay calculation. This combines the speed of eigenphase fitting and accuracy of the time-delay method. A detailed comparison of the methods investigated to detect and fit resonances is given in chapter 5.

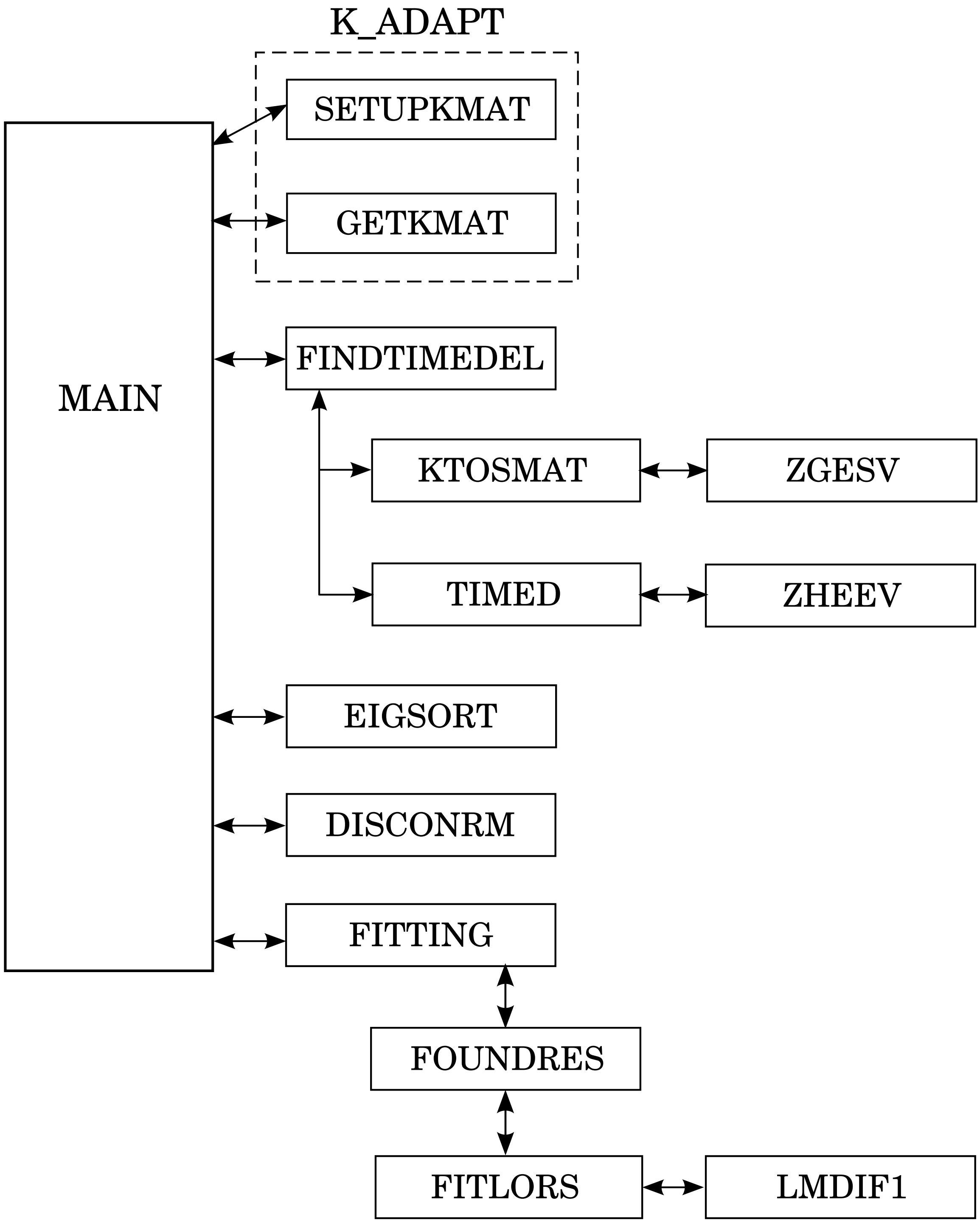

Figure 3.2: The structure of TIMEDEL. The routines in the dashed line box are in the module K_ADAPT.

Chapter 4

Computing bound states

4.1 Introduction

In this chapter, using the theoretical methods described in chapter 2, the computation of bound states to find potential energy curves of N_2 is described. Considering the importance of N_2 to the earth's atmosphere, other than studies of states of $^1\Sigma_u^+$ and $^1\Pi_u$ symmetry, the literature on electronic excited states is surprisingly brief. Few experimental studies have probed the Rydberg series of triplet and gerade symmetry that underlie the first ionisation limit with a similar paucity of theoretical treatments. Lofthus and Krupenie (1977) gave a comprehensive summary of the observed electronic spectra of N_2 considering the lowest fifteen or so electronic states, later updated by Huber and Herzberg (1979). Since, there have been numerous experimental studies; Suzuki and Kakimoto (1982); Stahel et al. (1983); Roncin et al. (1984); Verma and Jois (1984); Roncin et al. (1989); Huber and Jungen (1990); Roncin et al. (1991); Levelt and Ubachs (1992); Edwards et al. (1993); van der Kamp et al. (1994); Whang et al. (1996); Kawamoto et al. (1997); Roncin et al. (1998); de Lange and Ubachs (1999); Sprengers et al. (2004); Cossart and Cossart-Magos (2004); Hashimoto and Kanamori (2006); Lewis, Heays, Gibson, Lefebvre-Brion and Lefebvre (2008); Lewis, Baldwin, Heays, Gibson, Sprengers, Ubachs and Fujitake (2008); Salumbides et al. (2009). All but a few of these studies are measurements of transitions involving the $^1\Sigma_u^+$ and $^1\Pi_u$ states. More recently, Hashimoto and Kanamori (2006), Lewis, Heays, Gibson, Lefebvre-Brion and Lefebvre (2008) and Lewis, Baldwin, Heays, Gibson, Sprengers, Ubachs and Fujitake (2008) have measured the $^3\Sigma_u^+$ and $^3\Pi_u$ states. Cossart and Cossart-Magos (2004) measured the d_3 $^1\Sigma_g^+$ state for the first time.

There have been a number of theoretical calculations, most notably Ermler et al. (1982); Spelsberg and Meyer (2001); Michels (2007); Ndome et al. (2008); Hochlaf, Ndome, Hammoutène and Vervloet (2010); Hochlaf, Ndome and Hammoutène (2010). Studies attempting to model the Rydberg states or Rydberg components of states are isolated to Spelsberg and Meyer (2001); Hochlaf, Ndome, Hammoutène and Vervloet (2010). Spelsberg and Meyer (2001) give a particularly detailed *ab initio* study of the interaction between N_2 Rydberg and valence states, albeit only for two symmetries. Guberman (1991, 2003, 2007, 2012, 2013) has presented curves for the same purpose as this work, that is for the study of dissociative recombination (DR) of the N_2^+ ion . Comparisons are made with the theoretical and experimental work below.

The aim of the work presented in this chapter was to characterise as many excited states of N_2 as possible for all singlet and triplet symmetries. States up to g-wave character are considered. This is not a severe restriction as one can expect that states with $\ell \geq 5$ to have quantum defects which are very close to zero. The resulting calculation constitutes a comprehensive set of curves for the singlet and triplet states of N_2; these curves provide a comprehensive 'map' of the electronic structure. Mapping out the electronic structure in this way means that states which favour dissociative recombination can then easily be selected without ambiguity. The Rydberg states and the valence states, many of which were previously unknown, are characterised by equilibrium internuclear separation, energy and quantum defect. Extensive comparisons between the characterised states and previous experimental and theoretical work are made.

The chapter is structured as follows; starting from the target calculation, the development and testing of the model used for the R-matrix calculations is discussed; this model is also used for the resonant state calculations in chapter 5. In the model development process three different *ab initio* procedures were tested; multi-reference configuration interaction (MRCI) using the quantum chemistry package MOLPRO (Werner et al., 2010), a quantum chemistry mode (QC mode) calculation and the full R-matrix based bound state calculation. The QC mode calculation and the R-matrix bound state calculation are both discussed in section 2.4.1 of chapter 2. The final results use the R-matrix method bound state finding method. Results and a discussion are given with a comparison with previous work. Conclusions are made at the end of the chapter.

In the following discussion the reader should note that the polyatomic implementation of the UK molecular R-matrix codes discussed in chapter 2 use only Abelian symmetries, calculations were actually performed using D_{2h} symmetry. In most cases it is straightforward to transform these results to the higher linear-molecule, $D_{\infty h}$ symmetry and $D_{\infty h}$ symmetry designations are used for the description of states where these can be assigned unambiguously.

All of the data presented in this chapter is available in the supplementary data of Little and Tennyson (2013).

4.2 Theoretical model: Method, development and testing

4.2.1 Target calculation

The first step in an R-matrix calculation is to calculate the properties of the target molecule. If one wishes to find accurate bound Rydberg states, which can be represented as an electron interacting with a particular target state of the ion, then a good representation of the target is essential. Additionally, for the inclusion of core-excited state in a DR model, a target model is needed that also gives a good representation of excited states. A number of target models were tested.

There are two variables that need to be explored in a target calculation, the basis set, and complete active space (CAS) which is used to generate molecular orbitals and to perform the target state configuration-interaction (CI). The starting point of the calculation is generating molecular orbitals (MOs). In this case MOs were generated using a multi-configuration self-consistent field (MCSCF) calculation averaged over the first four states using MOLPRO. Three different Gaussian type orbital (GTO) cc-pVXZ (where X is D,T or Q) bases of Dunning (1989) were tested with the MCSCF calculation. A CAS of 9 electrons distributed between three σ_g, three σ_u, one π_u and one π_g orbitals with four electrons frozen in the first two σ orbitals was used. This CAS can be denoted $(1\sigma_g, 1\sigma_u)^4$ $(2\sigma_g, 3\sigma_g, 2\sigma_u, 3\sigma_u, 1\pi_u, 1\pi_g)^9$. Other CASs were tested in conjunction with the $N+1$ electron inner region calculation tests and will be described in the next section.

The 110 MOs generated in the MOLPRO calculation were then reordered and renormalised to be used with the UKRMol code suite using the module MPOUTRD (see section 2.5 of chapter 2). The target state wavefunctions were calculated using a CI expansion of individual N electron configurations using the CI program SCATCI (see section 2.5 of chapter 2 and Tennyson (1996)). To keep the calculation consistent, the same CAS was used for the target state CI calculation as the MOLPRO calculation. 8 target states were calculated for each of the 16 symmetries (singlet and triplets in $\mathrm{D_{2h}}$ representation) resulting in 128 target states. However, this was reduced to the lowest 100 for the $N+1$ electron inner region calculation. The number of target states included in the calculation is arbitrary; as the internuclear separation changes the energy order of the target states changes. The effects of this are minimised by using a large number of states. It also ensures that no state is generated in $\mathrm{D_{2h}}$ symmetry without its $\mathrm{D_{\infty h}}$ degenerate pair, for example an $\mathrm{A_g}$ state and a $\mathrm{B_{1g}}$ state are needed to form a Δ_g state. Despite taking these measures, there are still minor discontinuities in a small number of calculated curves, the most significant in the G $^3\Delta_\mathrm{g}$ state ($\sim$ 0.04 eV) at 1.614 Å.

The agreement with the experimental ionic curves given in Lofthus and Krupenie (1977) when using the ccp-VQZ basis was good enough that further tests seemed superfluous (see figure 4.1). In any case the size of the basis set that can be used with the R-matrix method is limited by the spatial restriction of the R-matrix sphere. Going beyond the cc-pVQZ basis set resulted in the target basis functions being too diffuse and crossing the inner region boundary. The agreement between the vertical excitation energies of the target model for the first two excited states (A $^2\Pi_\mathrm{u}$ and B $^2\Sigma_\mathrm{u}^+$) at equilibrium internuclear separation is very good (see table 4.1). The general agreement of the potential energy curves for these three states with the RKR curves given by Lofthus and Krupenie (1977) and extended by Guberman (2012) is good, see figure 4.1.

Table 4.1: Vertical equilibrium excitation energies (eV) and equilibrium positions (Å) for the ground state and first two excited states of the ionic target.

State	This work		Experiment		Comparison	
	T_e	R_e	T_e	R_e	ΔT_e [a]	ΔR_e [a]
X $^2\Sigma_g^+$	0.0	1.125	—	1.11642	—	−0.00858
A $^2\Pi_u$	1.215	1.181	1.1365	1.174	−0.0785	−0.0061
B $^2\Sigma_u^+$	3.165	1.082	3.1568	1.074	−0.0082	−0.0080

[a] Obs. − Calc.

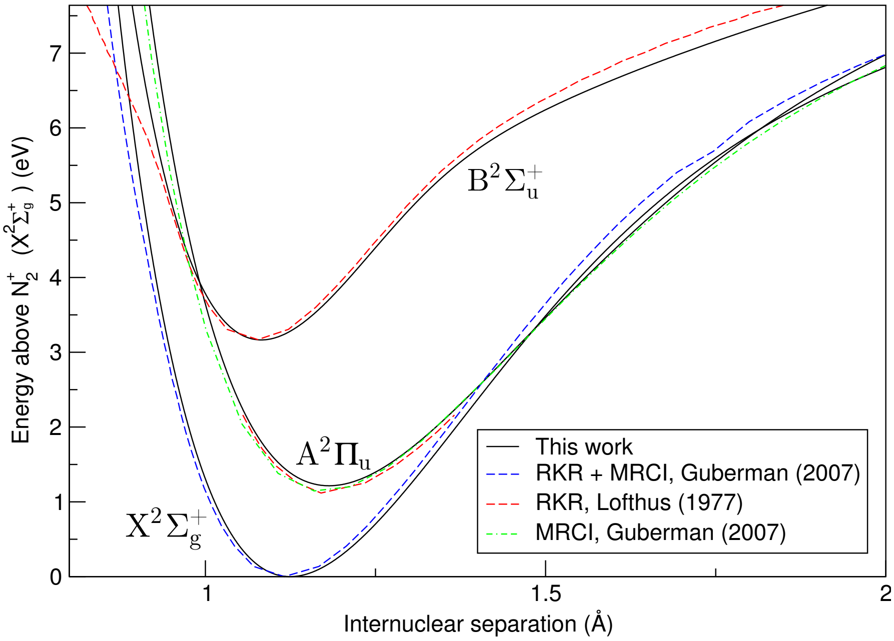

Figure 4.1: Potential energy curves of the ground state and first two excited states of N_2^+ used as the representation of the target. A comparison is given with empirical RKR curves given by Lofthus and Krupenie (1977) and those extended and calculated by Guberman (2007).

4.2.2 $N + 1$ electron inner region calculation

As described in chapter 2 the $N+1$ calculation is essentially an extension of the target calculation in which the scattering electron is introduced into the CI. There are two important things to consider in this stage of the model development; firstly the end result of an R-matrix calculation is a combination of two different variational electronic structure calculations, the target and $N+1$ electron. This brings about the issue of balance between the two calculations. 'Improving' the $N+1$ electron calculation, that is including more configuration state functions in the calculation, results in the lowering of energies of R-matrix poles and henceforth increases the binding energies of bound states, potentially moving resonant scattering states to bound states. Conversely, lowering the target state energies results in R-matrix poles moving up in energy relative to the ground state of the target. Therefore, correctly balancing a model is integral to its development and reliability when using the R-matrix method and the inner region CAS needs to be chosen carefully. For a more detailed discussion on balance see Tennyson (2010). Secondly the scattering electron must be accommodated by orbitals that represent the continuum; often the inclusion of these continuum orbitals lead to overcompleteness causing linear dependence issues. Therefore one must be be sure to remove the linear dependence from the basis set describing the orbitals. Both of these issues are discussed below in the context of the model development.

Choosing the $N+1$ complete active space (CAS)

Choosing the $N+1$ complete active space (CAS) is a process in which the the number of virtual orbitals (see section 2.3.3 of chapter 2) included in the CAS is varied. Increasing the number of virtual orbitals, that is, increasing the size of the CAS, means that more configuration state functions are included in the CI expansion resulting in a lowering of energy of the calculated electronic states. Balancing the size of the $N+1$ calculation with the target calculation is achieved by adding and removing virtual orbitals from the CAS. Changing the number of virtual orbitals and then comparing the ionisation energy with the experimental value indicates whether or not the $N+1$ calculation is correctly balanced with the target calculation. It is by this process of trial and error than an $N+1$ CAS can be chosen.

Initial tests involved contracted virtual orbitals (see section 2.3.3 of chapter 2) with an $N+1$ CAS of $5\sigma_g$, $3\sigma_u$, $2\pi_u$ and $1\pi_g$ orbitals. Calculations showed that this was unbalanced with respect to the target, and the valence states were too high in energy. The virtual orbitals were then uncontracted (see section 2.3.3 of chapter 2) and the CAS extended to sensible sizes dictated by the energy ordering of the orbitals given by the MCSCF calculation. Following this the inner region CAS was increased to $(14\sigma_g, 14\sigma_u, 7\pi_u, 6\pi_g, 3\delta_u, 3\delta_g)$, giving an ionisation energy that was much too high. With the view to improve the overall balance the target CAS was expanded; however, this merely made the calculation intractably large and slow for very little gain in accuracy. Efforts were made throughout the model development process to keep the calculation times short, without diminishing the accuracy, meaning that many internuclear separations could be calculated in a reasonable amount of time.

An attempt was made to increase the size of the target calculation without significantly increasing the size of the $N+1$ calculation. The target calculation was extended to allow a single electron only to occupy the $4\sigma_g$, $4\sigma_u$ and $2\pi_g$ orbitals; this can be thought of as having the original target CAS described in section 4.2.1, with an additional $(1\sigma_g, 1\sigma_u)^4$ $(2\sigma_g, 3\sigma_g, 2\sigma_u, 3\sigma_u, 1\pi_u, 1\pi_g)^8$ $(4\sigma_g,\ 4\sigma_u,\ 2\pi_g)^1$. This gave less accurate results, largely due the difficulties in finding a CAS for the MCSCF calculation that was consistent with the target calculation and also converged. Rotating orbitals after the MCSCF calculation was also explored in an attempt to better represent the valence states, these rotations severely disrupted the representation of the target states and this approach was abandoned.

The $N+1$ CAS was then reduced in steps, again dictated by the MCSCF orbital energies, having the effect of decreasing the overestimated ionisation energy until the best agreement with experiment was found. This resulted in the following model; the target calculation CAS given in section 4.2.1 was augmented with 14 virtual orbitals to $(5\sigma_g, 5\sigma_u, 3\pi_u, 2\pi_g, 1\delta_u, 1\delta_g)$. There are then three types of configurations making up the $N+1$ CAS: those in which the scattering electron is only allowed to occupy continuum orbitals, the first summation in eq. (2.19), and two types of L^2 configurations, the second summation in eq. (2.19). The two types of L^2 configurations are those in which the scattering electron occupies the target orbitals, which can be represented as $(1\sigma_g, 1\sigma_u)^4\ (2\sigma_g, 3\sigma_g, 2\sigma_u, 3\sigma_u, 1\pi_u, 1\pi_g)^{10}$ and those in which the scattering electron occupies the additional $N+1$ virtual orbitals given by $(1\sigma_g, 1\sigma_u)^4\ (2\sigma_g, 3\sigma_g, 2\sigma_u, 3\sigma_u, 1\pi_u, 1\pi_g)^9$ $(4\sigma_g, 5\sigma_g, 4\sigma_u, 5\sigma_u, 2\pi_u, 3\pi_u, 2\pi_g, 1\delta_u, 1\delta_g)^1$. Although a significant amount of effort was put into producing valence states as accurately as possible, the ionisation energy in the final model is 0.407 eV too high. This leads to poorly represented equilibrium energies when compared with experimental data or MRCI calculations. This problem can be attributed to the top down approach of the R-matrix bound state calculation method used, the calculation accuracy decreases with energy relative to the ion ground state. Low-lying valence states are best represented using standard quantum chemistry methods such as MRCI. However, these methods struggle to represent genuine Rydberg states, see figure 4.7.

Continuum orbitals and orthogonalisation

As mentioned above, the $N+1$ calculation is essentially an extension of the target calculation in which the scattering electron is introduced into the CI. To accommodate the scattering electron continuum orbitals must be included in the calculation. These continuum orbitals take the form of bond-centred GTOs fitted to Bessel functions for $\ell \leq 4$ taken from Faure et al. (2002). Although it would be expected that GTOs fitted to Coulomb functions would give better results for an ionic target, this was not found to be the case; the completeness of the cc-pVQZ basis resulted in some linear dependence between target and continuum orbitals when the Coulomb functions were used.

Once the one and two-electron integrals are calculated, now including continuum orbitals, the continuum orbitals are orthogonalised to the target MOs. The continuum orbitals are then symmetric-orthogonalised so all orbitals are orthonormal. The MOs calculated for the target were also used in the $N+1$ calculation. Due to the numerical nature of the orthogonalisation procedure, orbital combinations which are effectively linear dependent have small but not precisely zero eigenvalues of the overlap matrix. Therefore a deletion threshold is set below which all eigenvalues are assumed to represent linearly-dependent combinations which can safely be removed from the basis. Initially this threshold was set at the default value of 10^{-7}. Although ideally this deletion threshold would have been sufficient for all symmetries, it was found that when the calculation was extended into the continuum (the description of which is given in chapter 5), there were significant linear dependence errors in the final positions and widths of the resonant states of Σ_u^+ and Δ_u symmetry as well as the resonance states of Π_g and Φ_g symmetry. It was found that increasing the deletion threshold to 10^{-5} from the default value of 10^{-7} used for all other symmetries eliminated the linear dependence errors. Increasing the deletion threshold reduces the number of MOs used in the calculation, effectively reducing the size of the basis set. As this is a variational calculation the result of this is that the energy positions of the bound states increase slightly relative to their position when calculated with 10^{-7} threshold resulting in a largely uniform shift of $\lesssim 0.01$ eV. However, Rydberg states with the lowest symmetrically allowed value of ℓ for a given n shifted by a more significant amount, around 0.1 eV. The stability and smoothness of these curves also improved indicating that the linear dependence errors had been removed.

Beyond the smaller basis sets described in section 4.2.1 the more diffuse basis set aug-ccp-VQZ was tested; this led to significant linear dependence errors in the orbital orthogonalisation step and it was concluded the ccp-VQZ basis was sufficiently diffuse, and complete for an accurate description of the Rydberg states. Natural orbitals (NOs) calculated using an multi-reference configuration interaction (MRCI) were also tested as alternative to MCSCF orbitals. The NOs gave very similar results to the the MCSCF orbitals and their generation slowed the calculation significantly so were not used. Other tests involving the orbitals used included adding more states to the MOLPRO calculation with different weightings and averaging across the orbitals of two separate N_2^+ and N_2 MCSCF calculations. The former made little difference to energies as long as sensible weightings were used, and the latter again disrupted the target making it redundant.

4.2.3 Outer region bound state calculations

After solving for the inner region wavefunctions the target properties, the $(N+1)$-eigenpairs and raw boundary amplitudes are combined in the interface program SWINTERF (see section 2.5 of chapter 2) to produce the information necessary to compute the R-matrix on the boundary. At this point all but the first five (four in $D_{\infty h}$) target states ($^2\Sigma_g^+,^2\Pi_u,^2\Sigma_u^+$ and $^4\Sigma_u^+$ at equilibrium) are dispensed with. This reduces the number of channels leading to an increase in speed of the outer region calculation tenfold, and greater numerically stability as the channels associated with the highly excited target states are strongly-closed, see section 2.6.1 of chapter 2 and appendix B for more details. The R-matrix is then built on the boundary and the wavefunction integrated to a distance of 30.1 a_0 from where an asymptotic expansion due to Gailitis (1976) is used. The bound state energies were calculated using the program BOUND and the method described in section 2.4.1 of chapter 2. Despite the use of an improved Runge-Kunta-Nystrom integration procedure (Baker et al., 1999), as implemented by Zhang et al. (2011), the bound state routine still gave a considerable number of false detections. These were easily removed as they did not form curves.

4.2.4 Quantum chemistry-style calculations

Another option within the UKRMol code suite is to completely ignore the outer region and treat the $N+1$ calculation as a standard bound state electronic structure calculation, the so-called quantum chemistry (QC) mode, described in section 2.4.1 of chapter 2. These calculations were performed for the same number of symmetries and internuclear separations as the full, bound state R-matrix calculation described above as a means of comparison, an example of this can be seen in figure 4.2.

Attempts were made to follow the recipe provided by Spelsberg and Meyer (2001) for the b′ $^1\Sigma_u^+$, c_4' $^1\Sigma_u^+$, c_5' $^1\Sigma_u^+$, b $^1\Pi_u$, c_3 $^1\Pi_u$ and o_3 $^1\Pi_u$ states. This involved performing repeated MCSCF calculations for the orbital generation in which the CAS was built up in each repetition with single occupancy orbital occupation restrictions being applied. Higher energy orbitals beyond the CAS were also rotated down, for example, the first pair of δ_g orbitals. Although orbitals in the MOLPRO calculation could be correctly generated to repeat the essentials of the MRCI calculation given by Spelsberg and Meyers, implementing these orbitals within the R-matrix calculation in a meaningful and consistent way proved difficult. Firstly, these orbitals were generated for N_2 and not N_2^+ meaning that the target calculation suffered; it proved difficult to include the orbitals generated using the method of Spelsberg and Meyer (2001) in a MCSCF N_2^+ calculation which would converge. Secondly, central to Spelsberg and Meyer's method is the inclusion of diffuse bond-centred s and p orbitals, and an augmented basis set; these types of orbitals are not usually included in an R-matrix calculation until the $N+1$ stage; and as mentioned above the use of the aug-ccp-QVZ created linear dependence problems. Lastly, Spelsberg and Meyer's calculation was a specific attempt to calculate three states for two different symmetries, hence could afford to tailor the orbitals to optimise the representation of particular states. As the aim was to create a model which gave reasonable results for all symmetries this was not an option. As a result it is not expected that the model will produce valence state curves on a similar scale of accuracy to Spelsberg and Meyer (2001).

4.3 Calculation details

Bound state calculations were performed for singlet and triplets for all D_{2h} symmetries. Given the constraint that $\ell \leq 4$, this gives $D_{\infty h}$ states of $\Sigma_{g/u}^{+/-}$, $\Pi_{u/g}$, $\Delta_{g/u}$, $\Phi_{u/g}$, Γ_g symmetries. Calculations were performed at a dense grid of 1199 points in the range 0.8 Å $\leq R \leq$ 1.999 Å, where R is the internuclear separation.

4.4 Results

4.4.1 Ionic target calculation

Table 4.1 presents vertical equilibrium excitation energies and equilibrium positions for the ground state and first two excited states of the N_2^+ target calculation; a comparison with experimental values is given. The agreement with experimental data is very good. Potential energy curves for the target can be seen in figure 4.1, where a comparison is made with the RKR curves given in Lofthus and Krupenie (1977) as well as those which were then extended and supplemented with MRCI curves by Guberman (2007). The agreement is good in the region around equilibrium for all three states and a divergence is only seen at longer bond lengths. The irregularity of the B state RKR potential is explained by an interaction with the C $^2\Sigma_u^+$ state not shown on the figure Singh and Rai (1966).

For a scattering calculation of the type presented here, it is expected that for only a limited number of target states that is, one or two, will the energies and wavefunctions approach anything like the exact solution of the problem. There are number of reasons for this: the basis set used in the R-matrix calculation must not go beyond the R-matrix boundary, this limits the size of basis set that can be used. The target calculation must be kept to a modest size as the the inner region calculation scales significantly with the size of the target, therefore a CASCI is used. A common orbital set must be used for all symmetries, this removes the option of tailoring each orbital set to each symmetry. All of these factors place limitations on the accuracy of the target calculation. Therefore, as this is the case, the C state in our calculation is not close enough in energy for this irregularity to be reproduced. However from the point of view of characterising the bound states of interest, that is highly excited dissociative states and Rydberg states of the first three states, this representation of the target should be more than adequate.

4.4.2 Bound states

Figure 4.2 compares the ^1A_g data set of scattering bound states with a QC mode $N+1$ calculation as described in section 4.2.4. Use of a dense grid of points removed any need to fit the curves. For the lower-lying states the two methods give near-identical results. However it is apparent that only the scattering calculations characterise the high-lying Rydberg states. The states predicted by the quantum chemistry calculations which lie above the N_2^+ ion ground state curve cannot be regarded as reliable (Stibbe and Tennyson, 1999). At low energies however, for valence type states, the quantum chemistry-style calculation gives very similar, within 0.02 eV, energies to the scattering calculation.

A convenient way of matching the raw data points to make up the potential energy curves is to use quantum defects, in this study defined by

$$E^B(R) - E^T(R) = -2\frac{Z^2}{\nu^2(R)} = -2\frac{Z^2}{(n-\alpha(R))^2} \tag{4.1}$$

with energies in Hartrees. E^B is the bound state energy, E^T is the energy of the target state of the ion on which the Rydberg series is converging and Z is the charge of the ionic core, so equals one here. n is the principle quantum number, ν the effective quantum number and α the quantum defect of the Rydberg electron. Quantum defects account for the unshielded Coulombic and non-Coulombic interaction an electron in a Rydberg state will experience when close to the nuclei and inner shell electrons of its parent molecule.

Quantum defects associated with Rydberg states are linear, smooth functions of R when calculated relative to the state on which the Rydberg state is converging, (Rabadán and Tennyson, 1997). Plotting ν against R gives what is known as an Edlén plot (Edlén, 1964), see figure 4.3, and provides a useful tool for matching the states when they become close in energy. Two examples are given in the figure, in (a) ν has been calculated relative to the ion ground state and (b) to the first excited state. In (a) the Rydberg states associated with the A state appear as what are known as 'intruder states' passing through the linear states associated with the ground state; whereas in (b) the opposite is true and these states now appear to be linear, an example of this has been highlighted in the figure.

All states were matched by quantum defect without a fitting function. Particularly for weakly bound states, there is a complicated mix of avoided and unavoided crossings brought about respectively by the mix of higher symmetries in the $\mathrm{D}_{\infty\mathrm{h}}$ being contained within the $\mathrm{D}_{2\mathrm{h}}$ outputs and valence states passing through the Rydberg series. The numerical instability of the bound state searching algorithm described in section 2.4.1 leads to two minor issues. Firstly, occasionally the algorithm misses points, leading to gaps in the curves; however, if the missed bondlengths are of particular interest the possibility of fitting the curve still remains. Secondly, the data becomes increasingly noisy at low binding energies and longer bond lengths, or when there are several states interacting. This problem is exacerbated by the proximity of the A state to the ground state which cross at around 1.4 Å. The result of this is that valence, ground state Rydberg states and A state Rydberg states are all present making it difficult to extract meaningful data at energies close to, or above, the equilibrium energy of the ion ground state. It is recommended that data above the line of reliability formed by (R = 1.355 Å, E_e = 1.639 eV) and (R = 1.905 Å, E_e = 6.778 eV) be treated with caution.

The curves were systematically identified by matching their quantum defects and total symmetry. Although every effort was made was to match the curves as consistently as possible with regards to symmetry, occasionally an avoided crossing appears as a crossing or *vice versa*. This occurs at points where many curves are interacting and is attributed to numerical noise; in some cases avoided crossings are so narrow they are ignored. An example of a matched set of curves with diabats highlighted in colour is given in figure 4.4 for $^1\Sigma_g^+$ total symmetry. The figure highlights the complexity of the avoided crossing structure inherent in the system as three different types of states (Rydberg converging on X $^1\Sigma_g^+$ and A $^2\Pi_u$ respectively and valence) interact close to the ionisation threshold.

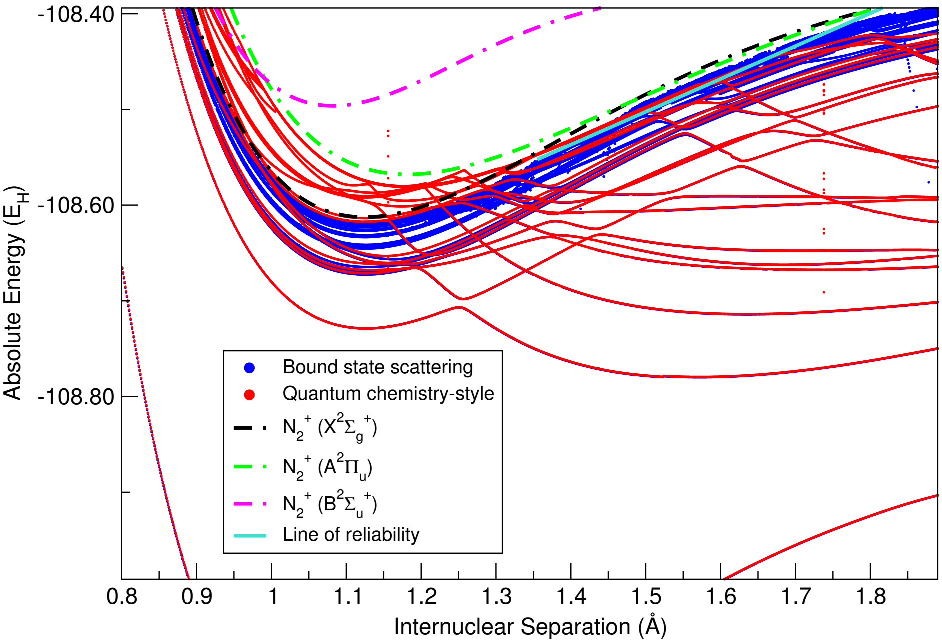

Figure 4.2: Comparison of a bound state scattering calculation with a quantum chemistry-style calculation as described in the text for ^1A_g symmetry. As this is a calculation in the lower symmetry group D_{2h}, states with symmetries $^1\Sigma_g^+$, $^1\Delta_g$ and $^1\Gamma_g$ all appear on this plot. Spurious data points have been removed. Note that for the lower-lying states the scattering and quantum chemistry-style results coincide.

4.5 Comparison with other work

4.5.1 Valence states

Due to the complexity of the interaction between the valence states and the Rydberg states at low binding energies $\lesssim 5$ eV attempting to separate the behaviour for fitting of spectroscopic constants becomes difficult. Therefore, only equilibrium energies (E_e) and positions (R_e) are tabulated in table 4.2 with a comparison to experimental data and previous theoretical calculations. All energies are given relative to the equilibrium energy of the N_2^+ ground state. Table 4.2 also gives a comparisons with other electronic states of N_2 that have been previously characterised. Due to the interaction with valence states some of the equilibrium positions of the Rydberg states are

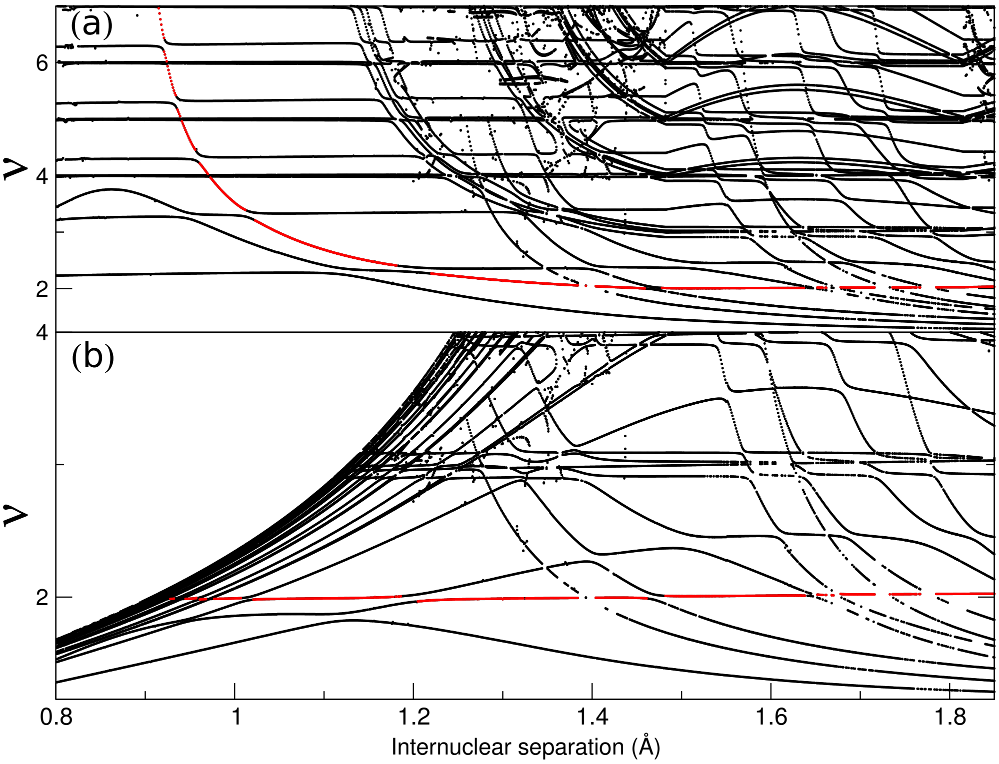

Figure 4.3: Edlén plots for $^1\mathrm{B}_{2\mathrm{u}}$ symmetry: (a) effective quantum numbers calculated relative to the ground state, X $^1\Sigma_\mathrm{g}^+$; (b) relative to the first excited state A $^2\Pi_\mathrm{u}$. Effective quantum numbers of Rydberg states are nearly constant with R if calculated relative to the state they are converging upon and so appear as straight lines on the plot. The red curve illustrates the behaviour of the A $^2\Pi_\mathrm{u}(3\mathrm{s}\sigma_\mathrm{g})$ state in the two cases.

strongly perturbed. This contributes to the disparity with spectroscopic values if this coupling was not included when the original spectroscopic constants were fitted to the experimental data. Due to the top down approach of the calculation the energies are presented as relative to the ion ground state as this gives the best comparison with experimental data. The ionisation energy is defined as $T_e(\mathrm{N}_2^+\ \mathrm{X}) = T_0(\mathrm{N}_2^+\ \mathrm{X}) - \frac{\omega_e}{2}(\mathrm{N}_2^+\ \mathrm{X}) + \frac{\omega_e}{2}(\mathrm{N}_2\ \mathrm{X}) = 15.590$ eV, where $T_0(\mathrm{N}_2^+\ \mathrm{X})$ has been defined relative $T_0(\mathrm{N}_2\ \mathrm{X})$. The spectroscopic parameters are taken from Lofthus and Krupenie (1977). If only T_0 is available then the energy has been is given relative to T_0 of N_2^+, as this is only the case for comparisons with Rydberg states, the relative correction to T_e is smaller than the accuracy with which the comparison is made, a note has been on the table if this is the case. As MRCI calculations are optimised relative to the neutral ground state rather the ion state, this way of presenting data is less favourable to such calculations.

The agreement in equilibrium position with experiment is good, all being within 5% of the experimental value and the majority within 1.5%. As mentioned in section 4.2.2, the ionisation energy produced by the model is too high, resulting in poor comparisons with experimental values for some of the valence states; such states largely lie at low energies. This problem arises as the low-lying states are more sensitive to valence shell correlation effects which are difficult to model in

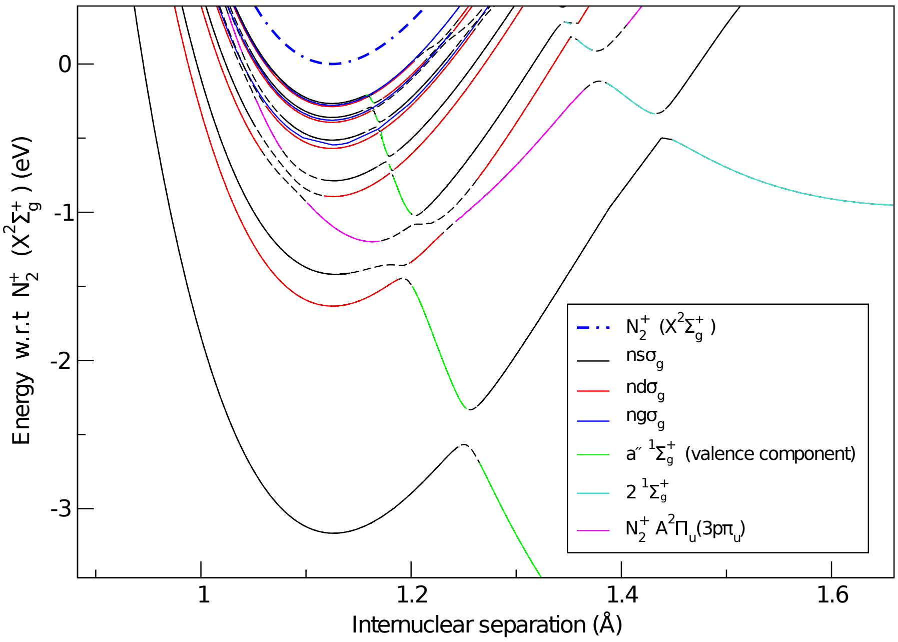

Figure 4.4: Calculated potential energy curves for the $^1\Sigma_g^+$ symmetry. Coloured are the Rydberg series nsσ_g, ndσ_g and ngσ_g as well as A $^2\Pi_u$(3pπ_u) and valence states a″ $^1\Sigma_g^+$ and 2 $^1\Sigma_g^+$. The lowest state in the ndσ_g series is that assigned by Cossart and Cossart-Magos (2004) to be d_3 $^1\Sigma_g^+$.

a scattering calculation. Despite this the majority of valence state equilibrium energies are within 5% of their experimental values.

With regards to other theoretical calculations, a comparison is made with three studies of similar sophistication, due to Spelsberg and Meyer (2001), Hochlaf, Ndome, Hammoutène and Vervloet (2010) and Guberman (2012), all of whom employed MRCI models. Comparisons with Hochlaf *et al* and Guberman are given in table 4.2. The agreement between calculated equilibrium positions is reasonable. However, as expected, the agreement with equilibrium energy is less favourable. Comparisons with the previous potential curves are given, figures 4.5 and 4.6 for Spelsberg and Meyer (2001), figure 4.7 for Hochlaf, Ndome, Hammoutène and Vervloet (2010) and figure 4.8 for Guberman (2012) and Hochlaf, Ndome, Hammoutène and Vervloet (2010). These figures also act as a comparison for the Rydberg states, where they exists, which will be discussed in the following section.

As Spelsberg & Meyer only report equilibrium energies for diabats, their calculated adiabats are placed at the given equilibrium energy of the lowest diabat in figures 4.5 and 4.6. For $^1\Pi_u$ the valence state, b $^1\Pi_u$ is poorly described by the model at long bond lengths, this is likely to be due to an under representation of the configuration $(\sigma_g{}^2, \sigma_u{}^2)(\sigma_g{}^3, \sigma_u{}^2, \pi_u{}^3, \pi_g{}^2)$. The o $^1\Pi_u$ state produced by the model is $\sim$ 0.2 eV too high, a result of the A ion state also being slightly too high. The agreement with the states of $^1\Sigma_u^+$ total symmetry is good with a favourable comparison with the general shape of the valence state curve; the equilibrium energies are slightly too low.

There appears to be no experimental data on the equilibrium energy or internuclear separation of the outer well of the a″ $^1\Sigma_g^+$ state, the state has come under some scrutiny recently due to the experimental studies of Bominaar et al. (2007) and Salumbides et al. (2009). Both studies make tentative spectroscopic assignments of high vibrational levels (Bominaar et al. $v = 32$, and Salumbides et al. $v = 22$ or $v = 23$) of the outer well of the $a'' \, ^1\Sigma_g^+$ state using the *ab initio* potential energy curve calculated by Ermler et al. (1982). The authors of both studies note that the potential energy curve calculated by Ermler et al. is not satisfactorily accurate to make confident assignments of the vibrational levels. Therefore the potential energy curve calculated in this study may be useful in making a more confident spectroscopic assignments for the vibrational levels of the outer well of this state.

In terms of theoretical data on the $a'' \, ^1\Sigma_g^+$ state, the results from this study agrees very well with the values calculated by Guberman, and are 0.195 eV lower than Hochlaf *et al.* Figure 4.7 compares the adiabat describing the $^1\Sigma_{\mathrm{g}}^+$ Rydberg and valence states with Hochlaf *et al.* Hochlaf *et al*'s representation of the $\mathrm{a}'' \, ^1\Sigma_{\mathrm{g}}^+$ valence component appears to have somewhat unphysical shape; furthermore, the Rydberg component found in this study traces the shape of the ion ground state curve, as would be expected. This figure again illustrates the suitability of a scattering calculation methodology over MRCI calculations for characterising Rydberg states.

Figure 4.8 compares calculations performed in this work with Guberman and Hochlaf *et al* for the $^3\Pi_{\mathrm{u}}$ states, important for the dissociative recombination of N_2^+ (see chapter 6). The agreement with Guberman is again good. The curves of Hochlaf *et al* are again higher than both ours and Guberman's.

4.5.2 Rydberg states

Tables 4.3–4.7 give equilibrium positions, energies and quantum defects for Rydberg series converging on the ground state of the ion. Table 4.8 lists those states which are bound in the N_2 equilibrium region and converge on the excited A $^2\Pi_{\mathrm{u}}$ ion state. A note is made if the equilibrium position of the Rydberg state has been perturbed by another Rydberg series or a valence state. A comparison is given with the rather limited data available on quantum defects, with general good agreement. As this is the first comprehensive calculation on Rydberg states of N_2, the comparison with other theoretical data is limited to that already discussed in section 4.5.1, apart from average quantum defects calculated by Guberman (2012) where the agreement is good. For Rydberg states converging on the ground state with $n \geq 4$ the agreement with spectroscopic data is good, in particular the $\mathrm{c}'_{\mathrm{n}} \, ^1\Sigma_{\mathrm{u}}^+$ or $^1\Sigma_{\mathrm{u}}^+(\mathrm{ns}\sigma_{\mathrm{u}})$ series. The assignment of the $\mathrm{d}_3 \, ^1\Sigma_{\mathrm{g}}^+$ by Cossart and Cossart-Magos (2004) is also confirmed. For $n = 3$ the agreement is generally good with the highest percentage difference being 5.58% for $\mathrm{c}_3 \, ^1\Pi_{\mathrm{u}}$. These discrepancies can be accounted for by two factors: a perturbed equilibrium position, the equilibrium position of $\mathrm{c}_3 \, ^1\Pi_{\mathrm{u}}$ is strongly perturbed, and the overestimation of the ionisation energy. The comparison with experimental values for Rydberg states converging on the A state is less favourable with a ∼12.5% difference for

Table 4.2: Equilibrium binding energies (eV) and equilibrium positions (Å) for valence states and Rydberg states for which experimental data is available. A comparison with spectroscopic data is given when available, all values are from Huber and Herzberg (1979) unless otherwise specified. A comparison is also given with Hochlaf, Ndome, Hammoutène and Vervloet (2010) (in-line entry) and Guberman (2012) (entry below in-line).

State	This work		Experiment		Comparison[a]		Other theory		Comparison[b]	
	E_B	R_e	E_B	R_e	ΔE_B	ΔR_e	E_B	R_e	ΔE_B	ΔR_e
$c'_{11}\ {}^1\Sigma_u^+$	−0.1258	1.125	−0.1264[h]		−0.0006					
$c'_{10}\ {}^1\Sigma_u^+$	−0.1539	1.125	−0.1541[h]		−0.0002					
$c'_9\ {}^1\Sigma_u^+$	−0.1927	1.125	−0.1933[h]		−0.0006					
$c'_8\ {}^1\Sigma_u^+$	−0.2481	1.125	−0.2490[h]		−0.0009					
$c'_7\ {}^1\Sigma_u^+$	−0.3315	1.124	−0.3351[h]		−0.0036					
$2\ {}^1\Pi_u$	−0.340	1.590								
$3\ {}^3\Sigma_g^-$	−0.456	1.518								
$c'_6\ {}^1\Sigma_u^+$	−0.465	1.125	−0.471[h]		−0.006					
$c_6\ {}^1\Pi_u$	−0.477	1.125	−0.480[e]		0.003					
$c_5\ {}^1\Pi_u$	−0.722	1.125	−0.730[e]		0.008					
$2\ {}^1\Pi_g$	−0.893	1.886								
$2\ {}^1\Sigma_g^+$	−0.959	1.700								
$c'_5\ {}^1\Sigma_u^+$	−0.700	1.127	−0.710[h]		−0.01					
$c'_4\ {}^1\Sigma_u^+$	−1.150[c]	1.138[c]	−1.217[h]		0.067					
$c_4\ {}^1\Pi_u$	−1.222	1.123	−1.253	1.116	0.031	−0.007				
$2\ {}^3\Delta_g$	−1.277	1.736								
							−1.195	1.692	−0.082	−0.044
$y\ {}^1\Pi_g$	−1.219[c]	1.179[c]	−1.418	1.177	0.199	0.002				
${}^1\Phi_u$	−1.314	1.580								
							−1.629	1.565	0.315	−0.015
$z\ {}^1\Delta_g$	−1.331[c]	1.155[c]	−1.278	1.169	0.053	0.014				
$2\ {}^1\Delta_g$	−1.361	1.684								
$2\ {}^3\Sigma_g^-$	−1.438	1.729					−1.375	1.821	−0.063	0.092
$k\ {}^1\Pi_g$	−1.465	1.128	−1.480	1.109	0.015	−0.019				
$1\ {}^1\Delta_g$	−1.504	1.732								
$x\ {}^1\Sigma_g^-$	−1.539	1.179	−1.526	1.173	0.013	−0.006				
$d_3\ \Sigma_g^+$	−1.633	1.125	−1.699[g]		0.066					
$o_3\ {}^1\Pi_u$	−2.182[c]	1.170[c]	−2.464	1.178	0.282	0.008				
$H\ {}^3\Phi_u$	−2.358	1.512	−2.483	1.488	0.125	−0.024	−2.210	1.499	−0.148	−0.013
							−2.534	1.506	0.176	−0.006
$c_3\ {}^1\Pi_u$	−2.488[c]	1.140[c]	−2.637	1.116	0.149	−0.024				
$F\ {}^3\Pi_u$	−2.254	1.168	−2.555[f]	1.176[f]	0.301	0.008				
$c'_3\ {}^1\Sigma_u^+$	−2.585	1.127	−2.635[h]		−0.050					
$G\ {}^3\Pi_u$	−2.660	1.127	−2.696[f]	1.113[f]	0.036	−0.014				
$b'\ {}^1\Sigma_u^+$	−2.780	1.463	−2.634	1.444	−0.146	−0.019				
							−2.794	1.499	0.014	0.036
$D\ {}^3\Sigma_u^+$	−2.680	1.125	−2.603	1.108	−0.077	−0.017				
$b\ {}^1\Pi_u$	−3.200	1.340	−2.984	1.284	−0.216	−0.056				
							−3.158	1.381	−0.042	0.041
$1\ {}^1\Gamma_g$	−2.765	1.636					−2.821	1.609	0.046	−0.027
							−3.100[d]	1.600[d]	0.335	−0.036
$a''\ {}^1\Sigma_g^+$										
Inner	−3.165	1.128	−3.190	1.122	0.025	−0.006	−3.698	1.114	−0.532	−0.014
Outer	−4.553	1.572					−4.367	1.557	−0.195	−0.015
							−4.570	1.574	0.017	0.002
$1\ {}^3\Sigma_g^-$	−3.659	1.631					−3.467	1.619	−0.192	−0.012
$C'\ {}^3\Pi_u$	−3.755	1.534	−3.396	1.514	−0.359	−0.020	−3.286	1.527	−0.469	−0.007
							−3.698	1.535	−0.057	0.001
$E\ {}^3\Sigma_g^+$	−3.575	1.127	−3.705	1.117	0.130	−0.010	−3.700	1.127	0.125	0.000
$C\ {}^3\Pi_u$	−4.703	1.162	−4.539	1.149	−0.164	−0.013	−4.401	1.154	−0.302	−0.008
							−4.583	1.160	−0.120	−0.002
$G\ {}^3\Delta_g$	−4.876	1.637	−4.692	1.611	−0.184	−0.026	−4.466	1.618	−0.410	−0.019
							−4.608	1.618	−0.268	−0.019
$w\ {}^1\Delta_u$	−6.786	1.282	−6.651	1.268	−0.135	−0.014	−6.47	1.295	−0.308	0.013
							−6.763	1.280	−0.023	−0.002
$a\ {}^1\Pi_g$	−7.088	1.235	−7.000	1.220	−0.088	−0.015	−6.915	1.223	−0.173	−0.012
							−7.043	1.226	−0.045	−0.009
$a'\ {}^1\Sigma_u^-$	−7.274	1.292	−7.140	1.276	−0.134	−0.016	−7.031	1.278	−0.243	−0.014
$B'\ {}^3\Sigma_u^-$	−7.667	1.292	−7.373	1.278	−0.294	−0.014	−7.349	1.283	−0.318	−0.009
$W\ {}^3\Delta_u$	−8.499	1.293	−8.175	1.300	−0.324	0.007	−8.147	1.283	−0.352	−0.010
							−8.243	1.285	−0.256	−0.008
$B\ {}^3\Pi_g$	−8.494	1.227	−8.198	1.213	−0.296	−0.014	−8.106	1.220	−0.388	−0.007
							−8.242	1.218	−0.252	−0.009
$A\ {}^3\Sigma_u^+$	−9.946	1.310	−9.366	1.287	−0.580	−0.023	−9.392	1.292	−0.554	−0.018
							−9.460	1.291	−0.486	−0.019
$X\ {}^1\Sigma_g^+$	−15.997	1.107	−15.590	1.098	−0.407	−0.009	−15.590	1.104	−0.407	−0.003

[a] Obs. − Calc.

[b] Other − This work

[c] Perturbed equilibrium position.

[d] Michels (2007)

[e] Lofthus and Krupenie (1977), only T_0 available.

[f] Lewis, Heays, Gibson, Lefebvre-Brion and Lefebvre (2008)

[g] Cossart and Cossart-Magos (2004), only T_0 available.

[h] Huber and Jungen (1990), only T_0 available.

Table 4.3: Equilibrium binding energies (eV), equilibrium positions (Å) and quantum defects for Rydberg states of ${}^1\Sigma$ and ${}^1\Pi$ symmetry. Experimental quantum defects are from Lofthus and Krupenie (1977).

	${}^1\Sigma_g^+$			${}^1\Sigma_u^+$			${}^1\Pi_g$			${}^1\Pi_u$		
n	E_e	R_e	α	E_e	R_e	α	E_e	R_e	α	E_e	R_e	α
		$s\sigma_g$			$p\sigma_u$[b]			$d\pi_g$			$p\pi_u$[d]	
3	−3.165[a]	1.128[a]	0.927	−2.585	1.127	0.706	−1.465[c]	1.128[c]	−0.047	−2.488[f]	1.140[f]	0.668[f]
4	−1.419	1.127	0.904	−1.150[f]	1.138[f]	0.577[f]	−0.820	1.125	−0.074	−1.222	1.124	0.663
5	−0.788	1.126	0.844	−0.700	1.127	0.591	−0.528	1.125	−0.078	−0.722	1.125	0.658
6	−0.514	1.125	0.853	−0.465	1.125	0.593	−0.368	1.125	−0.080	−0.477	1.125	0.657
7	−0.360	1.125	0.855	−0.332	1.124	0.593	−0.271	1.125	−0.081	−0.338	1.125	0.659
8	−0.267	1.125	0.857	−0.248	1.125	0.595				−0.254	1.125	0.676
9				−0.193	1.125	0.596						
10				−0.154	1.125	0.598						
11				−0.126	1.125	0.600						
		$d\sigma_g$			$f\sigma_u$			$g\pi_g$			$f\pi_u$	
3	−1.633[e]	1.125[e]	0.114									
4	−0.894	1.126	0.100	−0.860	1.124	0.024				−0.859	1.125	0.020
5	−0.569	1.124	0.112	−0.550	1.124	0.027	−0.546	1.125	0.006	−0.549	1.125	0.022
6	−0.393	1.125	0.116	−0.381	1.124	0.029	−0.379	1.125	0.007	−0.381	1.125	0.025
7	−0.287	1.125	0.119	−0.280	1.125	0.031	−0.278	1.125	0.007	−0.280	1.125	0.034
		$g\sigma_g$										
5	−0.546	1.125	0.007									
6	−0.379	1.125	0.008									
7	−0.278	1.124	0.008									

[a] a″ ${}^1\Sigma_g^+$ Inner, Expt. $\alpha = 0.97$.

[b] Series is c'_{4-11} ${}^1\Sigma_u^+$, Expt. $\alpha = 0.60822$, Huber and Jungen (1990).

[c] k ${}^1\Pi_g$.

[d] First four in series are: c_3 ${}^1\Pi_u$, Expt. $\alpha = 0.73$. c_4 ${}^1\Pi_u$, Expt. $\alpha = 0.70$., c_5 ${}^1\Pi_u$, Expt. $\alpha = 0.7$. c_6 ${}^1\Pi_u$, Expt. $\alpha = 0.68$

[e] d_3 Σ_g^+, Expt. $\alpha = 0.171$, Cossart and Cossart-Magos (2004).

[f] Perturbed equilibrium position.

the o_3 ${}^1\Pi_u$ and y ${}^1\Pi_g$ states. As indicated earlier this could be partly attributed to the A state being slightly too high in this model and perturbed equilibrium positions.

The agreement with spectroscopic data for the $n \geq 4$ states converging on the ground state asserts confidence in the validity of the Rydberg components predicted by this model. The agreement with the states converging on the A state is not as favourable, although, with the limited spectroscopic data available it is difficult to make a clear judgement as only limited comparisons can be made. As a result the data produced for Rydberg states converging upon the A state should be treated with more caution if used in future studies.

4.6 Conclusion

The R-matrix bound state search procedure based on finding negative energy scattering states has been used to identify the electronically excited states of the nitrogen molecule. The method is not competitive with high quality *ab initio* calculations for the low-lying valence curves but gives very good results for Rydberg states when, as here, a good representation of the ion is included in the calculation. The use of the procedure allows for the systematic characterisation of the singlet and

Table 4.4: Equilibrium binding energies (eV), equilibrium positions (Å) and quantum defects for Rydberg states of $^1\Delta$ and $^1\Phi$ symmetry.

	$^1\Delta_\mathrm{g}$			$^1\Delta_\mathrm{u}$			$^1\Phi_\mathrm{g}$			$^1\Phi_\mathrm{u}$		
n	E_e	R_e	α	E_e	R_e	α	E_e	R_e	α	E_e	R_e	α
		$\mathrm{d}\delta_\mathrm{g}$			$\mathrm{f}\delta_\mathrm{u}$			$\mathrm{g}\phi_\mathrm{g}$			$\mathrm{f}\phi_\mathrm{u}$	
3	−1.539	1.129	0.028									
4	−0.848	1.124	−0.005	−0.851	1.125	0.002				−0.844	1.125	−0.014
5	−0.543	1.125	−0.008	−0.545	1.125	0.005	−0.546	1.125	−0.001	−0.544	1.125	−0.012
6	−0.377	1.125	−0.008	−0.379	1.125	0.007	−0.379	1.125	−0.001	−0.378	1.125	−0.009
7	−0.277	1.125	−0.008	−0.279	1.125	0.009	−0.278	1.125	−0.001	−0.278	1.125	−0.003
8	−0.212	1.125	−0.008	−0.213	1.125	0.011						
9				−0.169	1.125	0.014						
10				−0.137	1.125	0.017						
		$\mathrm{g}\delta_\mathrm{g}$										
5	−0.546	1.125	0.009									
6	−0.380	1.125	0.014									
7	−0.279	1.125	0.017									
8	−0.214	1.125	0.019									

Table 4.5: Equilibrium binding energies (eV), equilibrium positions (Å) and quantum defects for Rydberg states of $^3\Sigma$ and $^3\Pi$ symmetry. All experimental quantum defects are from Lofthus and Krupenie (1977).

	$^3\Sigma_\mathrm{g}^+$			$^3\Sigma_\mathrm{u}^+$			$^3\Pi_\mathrm{g}$			$^3\Pi_\mathrm{u}$		
n	E_e	R_e	α	E_e	R_e	α	E_e	R_e	α	E_e	R_e	α
		$\mathrm{s}\sigma_\mathrm{g}$			$\mathrm{p}\sigma_\mathrm{u}$			$\mathrm{d}\pi_\mathrm{g}$			$\mathrm{p}\pi_\mathrm{u}$[f]	
3	−3.575[a]	1.127[a]	1.049	−2.680[b]	1.125[b]	0.747	−1.494	1.124	−0.018	−2.660[c]	1.127[c]	0.739[c]
4	−1.680	1.129	1.155	−1.256	1.124	0.709	−0.826	1.126	−0.059	−1.242	1.125	0.690
5	−0.915	1.124	1.143	−0.739	1.123	0.710	−0.532	1.125	−0.055	−0.733	1.123	0.693
6	−0.579	1.124	1.152	−0.489	1.123	0.727	−0.371	1.125	−0.053	−0.484	1.126	0.701
7	−0.398	1.125	1.156	−0.350	1.122	0.767	−0.274	1.125	−0.051	−0.346[e]	1.125[e]	0.726[e]
		$\mathrm{d}\sigma_\mathrm{g}$			$\mathrm{f}\sigma_\mathrm{u}$			$\mathrm{g}\pi_\mathrm{g}$			$\mathrm{f}\pi_\mathrm{u}$	
3	−1.514	1.128	0.003									
4	−0.840	1.125	−0.024	−0.854	1.125	0.008				−0.859	1.125	0.020
5	−0.546	1.125	0.007	−0.547	1.125	0.011	−0.546	1.125	0.006	−0.549	1.125	0.024
6	−0.379	1.124	0.008	−0.380	1.125	0.015	−0.379	1.125	0.007	−0.382[d]	1.125[d]	0.029[d]
7							−0.278	1.125	0.007			
		$\mathrm{g}\sigma_\mathrm{g}$										
5	−0.539	1.124	−0.023									
6	−0.375	1.124	−0.022									

[a] E $^3\Sigma_\mathrm{g}^+$, Expt. $\alpha = 1.08$.

[b] D $^3\Sigma_\mathrm{u}^+$, Expt. $\alpha = 0.77$.

[c] G $^3\Pi_\mathrm{u}$.

[d] Perturbed equilibrium position.

[e] Series continues but equilibrium positions become ambiguous due to strong perturbations from Rydberg series converging on $\mathrm{A}^2\Pi_\mathrm{u}$.

[f] Guberman (2012), R = 1.143, $\alpha = 0.7540$.

Table 4.6: Equilibrium binding energies (eV), equilibrium positions (Å) and quantum defects for Rydberg states of $^3\Delta$ and $^3\Phi$ symmetry.

	$^3\Delta_g$			$^3\Delta_u$			$^3\Phi_g$			$^3\Phi_u$		
n	E_e	R_e	α	E_e	R_e	α	E_e	R_e	α	E_e	R_e	α
		$\mathrm{d}\delta_g$			$\mathrm{f}\delta_u$			$\mathrm{g}\phi_g$			$\mathrm{f}\phi_u$	
3	−1.551	1.131	0.041									
4	−0.850	1.123	−0.001	−0.851	1.125	0.0023				−0.844	1.125	−0.014
5	−0.547	1.125	0.014	−0.545	1.125	0.0055	−0.544	1.124	−0.001	−0.542	1.125	−0.012
6	−0.380	1.125	0.020	−0.379	1.125	0.0080	−0.378	1.125	−0.001	−0.377	1.125	−0.008
7				−0.279	1.125	0.0103	−0.278	1.125	−0.001			
8				−0.213	1.125	0.0126						
9				−0.169	1.125	0.0154						
10				−0.136	1.125	0.0194						
		$\mathrm{g}\delta_g$										
5	−0.545	1.125	0.004									
6	−0.378	1.125	0.004									

Table 4.7: Equilibrium binding energies (eV), equilibrium positions (Å) and quantum defects for Rydberg states of Γ symmetry.

	$^1\Gamma_g$			$^3\Gamma_g$		
n	E_e	R_e	α	E_e	R_e	α
				$\mathrm{g}\gamma_g$		
5	−0.545	1.125	0.004	−0.543	1.125	−0.008
6	−0.378	1.125	0.004	−0.377	1.125	−0.008
7	−0.278	1.125	0.004			
8	−0.213	1.125	0.005			

Table 4.8: Equilibrium binding energies (eV), equilibrium positions (Å) and quantum defects for Rydberg states Rydberg states converging on A $^2\Pi_u$. The quantum defect is given relative to the A$^2\Pi_u$ state of N_2^+, the term in the parentheses gives the Rydberg electron symmetry. States given with full spectroscopic notation have be characterised previously and appear also in table 4.2.

State	E_e	R_e	α
$^1\Sigma_g^+(3\mathrm{p}\pi_u)$	−1.199	1.163	0.634
x $^1\Sigma_g^-(3\mathrm{p}\pi_u)$	−1.347	1.179	0.696
$^1\Sigma_u^-(3\mathrm{d}\pi_g)$	−0.219	1.182	−0.080
y $^1\Pi_g(3\mathrm{p}\sigma_u)$	−1.219	1.179	0.6360
o $^1\Pi_u(3\mathrm{s}\sigma_g)$	−2.182	1.170	0.172
z $^1\Delta_g(3\mathrm{p}\pi_u)$	−1.331	1.155	0.704
$^1\Delta_u(3\mathrm{d}\pi_g)$	−0.233	1.182	−0.065
$^3\Sigma_g^+(3\mathrm{p}\pi_u)$	−1.482	1.189	0.768
$^3\Sigma_g^-(3\mathrm{p}\pi_u)$	−1.349	1.181	0.697
$^3\Sigma_u^-(3\mathrm{d}\pi_g)$	−0.221	1.182	−0.078
$^3\Pi_g(3\mathrm{p}\sigma_u)$	−1.278	1.163	0.672
F $^3\Pi_u(3\mathrm{s}\sigma_g)$[a]	−2.254	1.168	1.022
$^3\Delta_g(3\mathrm{p}\pi_u)$	−1.486	1.196	0.760
$^3\Delta_u(3\mathrm{d}\pi_g)$	−0.2449	1.182	−0.0527

[a] Guberman (2012), R = 1.164, $\alpha = 1.009$.

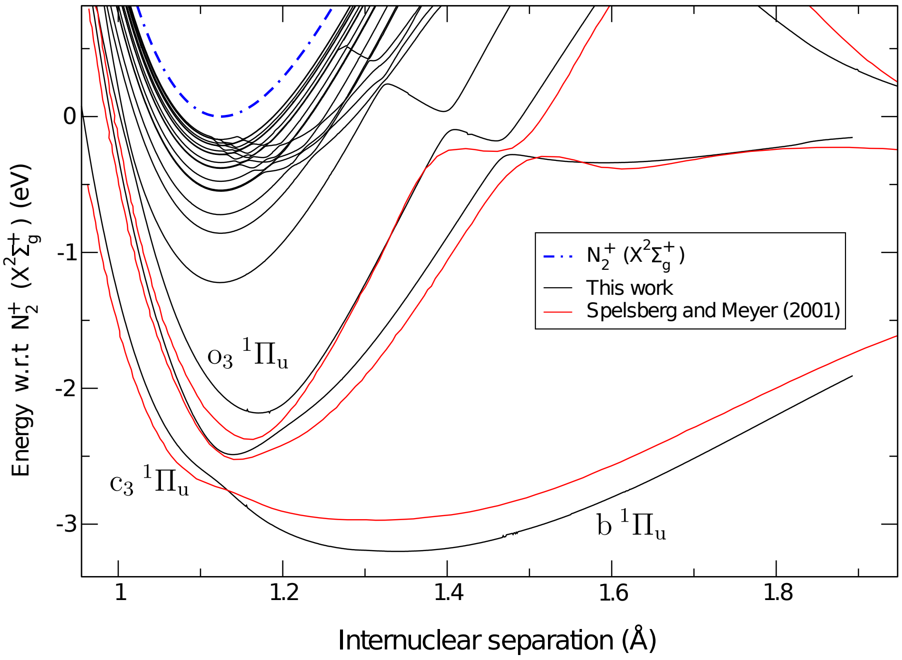

Figure 4.5: N_2 electronically excited states of ${}^1\Pi_u$ symmetry compared to those of Spelsberg and Meyer (2001).

triplet Rydberg series of N_2, the majority of them for the first time. The use of a computationally rapid procedure means that curves have been computed on a dense grid of points allowing the complicated nature of the many avoided crossings present in the system to be mapped out in detail and removing the need to fit the underlying curves. The comparison with spectroscopic data where available gave excellent agreement for Rydberg states converging on the ground state with $n \leq 4$. The curves represent the most comprehensive description of the electronic structure of N_2 and sets a bench mark for the calculation of Rydberg-valence states of diatomic molecules.

The work presented in the chapter is the first step towards gathering the data needed to compute a dissociative recombination cross-section. The bound states computed provide the lower portion of the potential energy curves, quantum defects and Rydberg-Rydberg couplings.

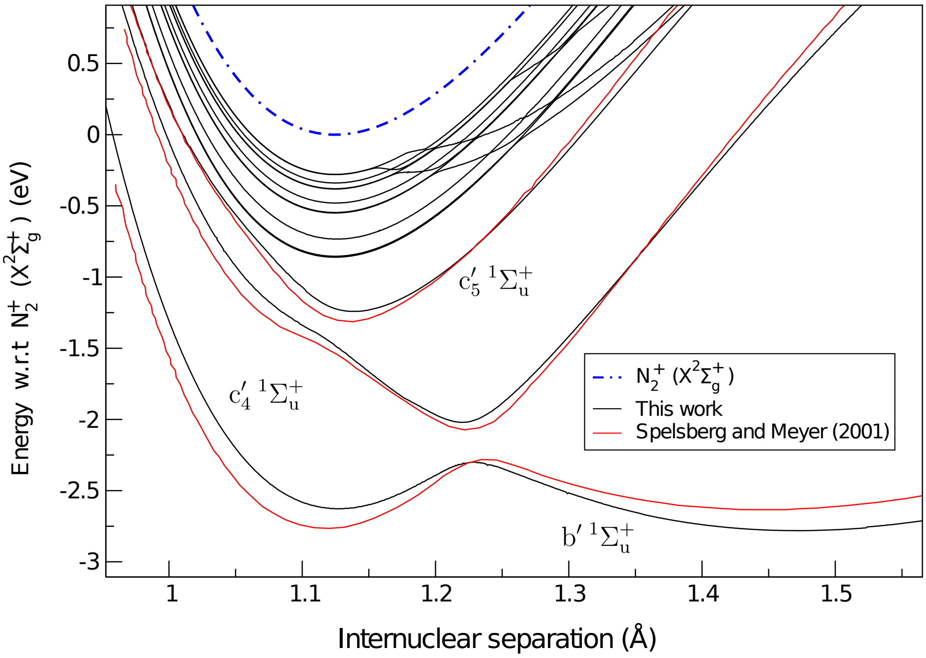

Figure 4.6: N_2 electronically excited states of ${}^1\Sigma_u^+$ symmetry compared to those of Spelsberg and Meyer (2001).

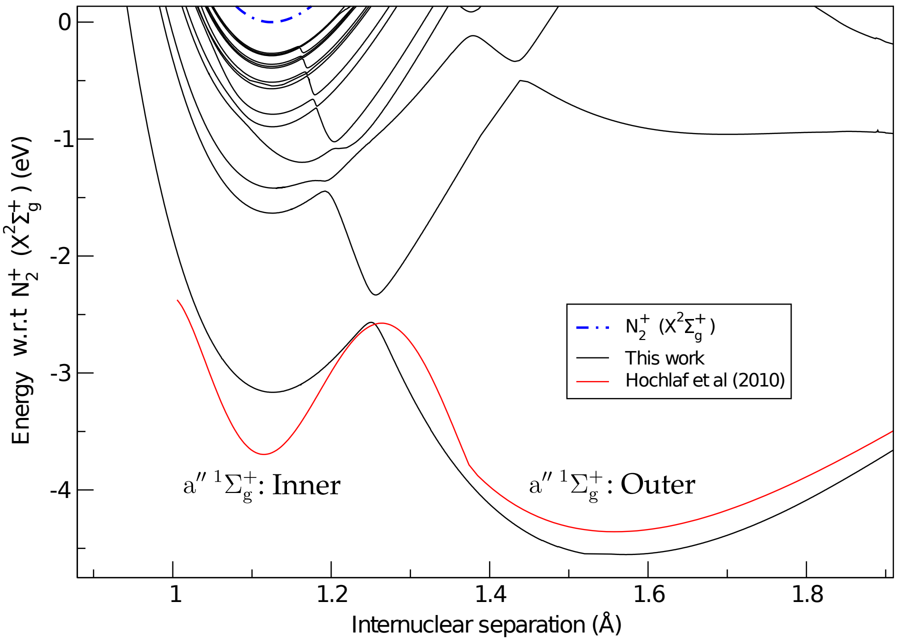

Figure 4.7: N_2 electronically excited states of ${}^1\Sigma_g^+$ symmetry compared to Hochlaf, Ndome, Hammoutène and Vervloet (2010).

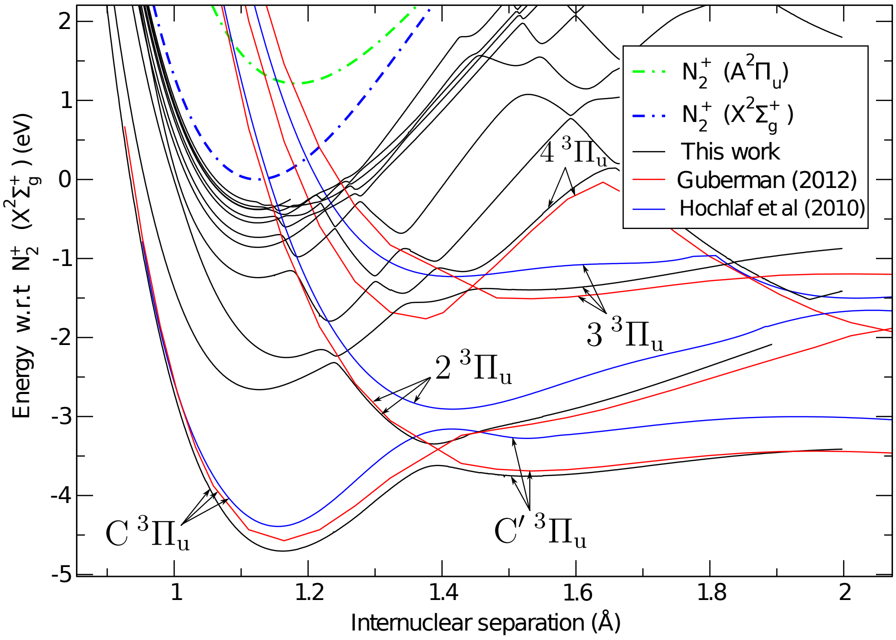

Figure 4.8: N_2 electronically excited states of $^3\Pi_u$ symmetry compared to those of Hochlaf, Ndome, Hammoutène and Vervloet (2010) and Guberman (2012).

Chapter 5

Computing resonant states

5.1 Introduction

In this chapter, using the model described in chapter 4, the calculation is extended into the continuum to the quasi-bound or resonance states lying above the ion ground state. The position and width of resonant states with both valence and Rydberg character are characterised. In the context of dissociative recombination (DR) the resonances are the intermediate step between electron recombination and dissociation, that is the doubly excited neutral molecule in eq. (1.4). The width of these resonances, known as the autoionisation width, gives the survival probability that the neutral molecule will autoionise before it has the chance to cross the ion curve, see figure 1.1 of chapter 1. The resonance positions provide the upper-portion of the potential energy curves, combined with the bound states calculated in chapter 4 a full description of the dissociative states above and below the ionisation threshold can be achieved.

Previous *ab initio* studies characterising states above the ion ground state can be separated into two categories: potential energy curve (PEC) calculations using quantum chemical methods, for which care is required (Stibbe and Tennyson, 1999), and scattering calculations. Guberman (2003, 2007, 2012, 2013) calculated PECs for his specific use in DR calculations using a multi-reference configuration interaction (MRCI) approach with the quantum chemistry package MOLPRO (Werner et al., 2010). As shown in chapter 4, while the representation of valence states given by an MRCI calculation is good, this approach does not give the same comprehensive information on the Rydberg states when compared to a scattering calculation. Comparisons with the work of Guberman are given below.

An R-matrix calculation by Ballance et al. (1998) found Rydberg-type resonances of $^{1,3}\Sigma_g^+$ symmetry, this work was extended by Nagy (Nagy et al., 1999; Nagy, 2003) to include vibrational motion to determine vibronic electron impact excitation cross-sections for the X → B transition. These calculations are in the spirit of a conventional scattering calculation; a single or small number of appropriate geometries are calculated to determine a scattering parameter which, in general, only depends on these internuclear separations. The aim of this work is to calculate resonant states at a large number of separations to make up sets of PECs for each symmetry with singlet and triplet spin.

Three methods were considered for the detection of characterisation of resonances; fitting the eigenphase sum (Hazi, 1979) using the UKRmol module RESON (Tennyson and Noble, 1984), the QB method of Quigley and Berrington (Quigley and Berrington, 1996; Quigley et al., 1998) and the time-delay method using the UKRmol module TIMEDEL which was discussed in the previous chapter. The use of each will be discussed in turn below. The calculations were performed using the same grid of internuclear separations described in section 4. The result is a comprehensive set of curves for singlet and triplet valence and Rydberg states of N_2 up to g-wave character above the ionisation threshold.

The chapter is organised as follows, first a description of the detection and fitting methods is given and comparisons between the methods are made. Following this are the results and discussion, and a comparison with previous work. Conclusions are made at the end of the chapter.

All data presented in this chapter is available in the supplementary data of Little and Tennyson (2014).

5.2 Resonance detection and fitting

The calculation of resonant states is identical to that of the bound states in chapter 4 in terms of the target and inner region. Only at the point at which the R-matrix generated and propagated do the models diverge. For the resonant states the R-Matrix is propagated to distance for results to stabilise; here a distance 300.1 a_0 (as opposed to 30.1 a_0 in the bound state model) was used. This is the only parameter that was changed from the model presented in chapter 4.

5.2.1 Fitting the eigenphase sum

Fitting of the eigenphase sum has long been the *de facto* option for resonance detection and fitting, not just for R-matrix calculations but also the complex Kohn variational method (Rescigno et al., 1995). The eigenphase sum, $\delta(E)$, at a given energy is calculated from the sum of the eigenvalues of the K-matrix, that is,

$$\delta(E) = \sum_i \arctan(K_{ii}).$$

Resonances appear as a rapid increase of π radians as a function of increasing energy. Once a resonance has been located it can be fitted to the Breit-Wigner form (Hazi, 1979),

$$\delta(E) = \delta_0(E) + \arctan\frac{\Gamma}{2(E^r - E)}, \tag{5.1}$$

where $\delta_0(E)$ is the background eigenphase. This form is explicitly appropriate for a single, isolated resonance. Breit-Wigner eigenphase fitting is integrated within the UKRmol code suite through the program RESON (see section 2.4.2 of chapter 2 and Tennyson and Noble (1984)). RESON scans $\delta(E)$ for points in which there is a change in sign of the numerically computed second derivative $\frac{d^2E}{d\delta^2}$. A new finer grid is constructed around the point of inflection and fitted with the Breit-Wigner form. This approach has the advantage of being automatic and computationally inexpensive: the resonances can be found rapidly with a fairly sparse energy grid and then the points of most importance computed. For neutral systems this approach is fast and reliable as there are few resonances which are generally well spaced in energy. For positively charged targets however, where there are many resonances often very close in energy, for example Rydberg states, this method runs into difficulty. Resolving multiple resonances close in energy and with varying width is problematic, often resonances are poorly fitted or missed see figure 5.1 and figure 5.2 below.

5.2.2 The QB method

The QB method (Quigley and Berrington, 1996; Quigley et al., 1998) is an R-matrix specific resonance characterisation procedure that takes advantage of the analytical properties of the R-matrix around a resonance. It was developed to be used for scattering from charged atomic targets and is based on the neglect of the outer region potential. Such potentials are significantly stronger in molecular ions so the QB method is not necessarily as accurate for molecules. However, it has been suggested that in favourable circumstances the QB method should produce results similar to that of RESON and TIMEDEL (Ballance et al., 1998). Homonuclear molecules such as nitrogen do not possess a permanent dipole moment so should be a favourable case. The QB method is analytic, so the inherent issues of a numerical calculation, robustness and numerical stability are avoided. The method is also computationally rapid and, unlike RESON and TIMEDEL which occasionally fail, in favourable circumstances provides complete sets of resonance.

In the QB method, the eponymous $\mathbf{Q}$ and $\mathbf{B}$ matrices are defined in terms of the asymptotic solutions, the R-matrix and energy derivatives so that, $d\mathbf{K}/dE = \mathbf{B}^{-1}\mathbf{Q}$. Eigenphase energy gradients of the $\mathbf{K}$ matrix can then be obtained; resonance positions are defined as the maximum gradient, the associated widths being related to the inverse of the eigenphase gradients.

Generally, the radius of the R-matrix sphere, a, is chosen to be large enough to enclose the target molecular charge cloud. For the QB method another issue has to be considered. Since the method neglects long-range potentials in the outer region, enlarging the inner region extends the range that these potentials are allowed for. In the case of N_2^+ the QB method gave, in most cases, positions and widths that were systematically lower than that given by both RESON and TIMEDEL, see figure 5.1. Attempts were made to improve the results by extending the R-matrix sphere to 15 a_0; although the resonance positions did change, they were still not comparable to those found by RESON and TIMEDEL. QB also did not detect a number of resonances associated with Rydberg states, see figure 5.1, the reason for this is unclear. As it was apparent that QB was not going to be suitable for this study no further investigation of this issue was undertaken.

5.2.3 Time-delay method

Using the module described in detail in chapter 3: TIMEDEL, the time-delay method was used to detect and fit resonances of N_2^+. Figures 5.1 and 5.2 give a comparison with the other two methods investigated. It is clear from figure 5.1 that TIMEDEL gives the most comprehensive description of the resonances. Figure 5.2 shows the suitability of TIMEDEL to detect and fit closely spaced, narrow overlapping resonances. That is, at energies close to the threshold ($\gtrsim$ 1.1 eV) separating individual behaviour of resonances becomes intractable when using the eigenphase sum; RESON successfully detects very few resonances in this energy range. Figure 5.2 also shows that even at low energies far from the threshold the very narrow resonances are only detected by TIMEDEL. Although the TIMEDEL fittings were subject to some false detections it was found to be the most robust and accurate fitting method and hence was the fitting method of choice for this study.

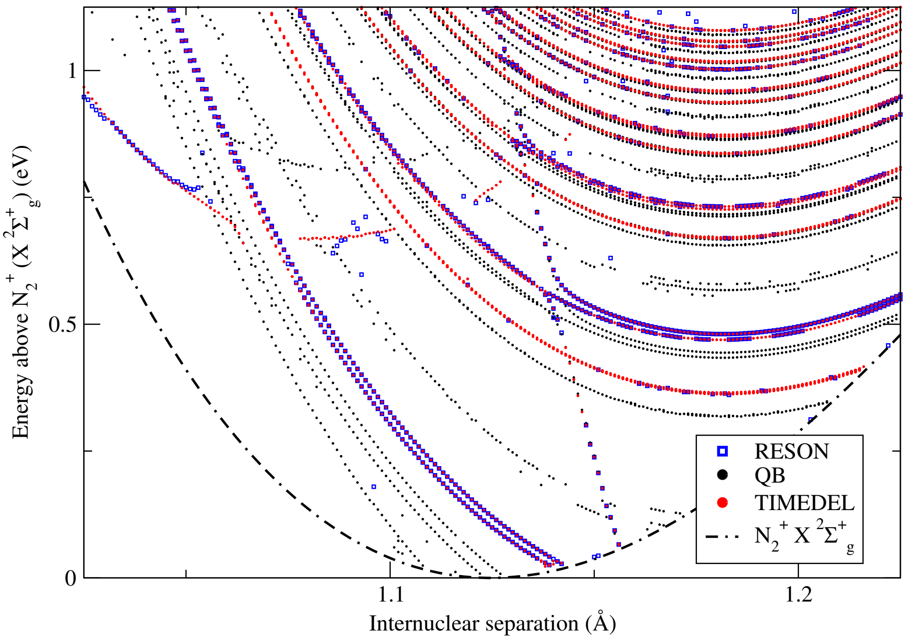

Figure 5.1: Comparison of the three different detection and fitting methods tested by resonance position. TIMEDEL gives the most comprehensive description of the resonant states followed by QB. RESON is subject to many false and missed detections. TIMEDEL and RESON give the same resonance positions as they are calculated using the same set of K-matrices. QB uses analytical K-matrices which are found using approximations which are not accurate for N_2; this is evident by the systematic shift in resonance position when compared to TIMEDEL and RESON.

5.3 Calculation details

Resonances were calculated up to 6 eV above the equilibrium energy of the X state, this restricts the range of internuclear separations to $R \approx 0.894$ - 1.818 Å, a grid of 0.001 Å was used. In principle the maximum calculable value of n is only limited by the energy difference used to calculate the numerical derivative of the time-delay matrix. In this study Rydberg states were calculated up to $n = 10$. As in section 4.2.1 of chapter 4 the choice of 100 target states in the close-coupling expansion is arbitrary and the actual states selected change as a function R due state crossings. As a result of this, beyond 1.466 Å there are significant numerical problems, that is, channels relating to Rydberg states dropping out of the calculation and lead to discontinuities in PECs. PECs that remain smooth across 1.466 Å can be used in other studies as they are not affected by this state switch. Data relating to curves beyond 1.466 Å which is unstable should be ignored. These target state crossings also cause a some minor ($\sim$ 0.02 eV) discontinuities in the resonance energy curves at shorter R. Although in most cases TIMEDEL provides accurate robust fits, it is subject to false detections and poor fits due to the complications imposed by fitting overlapping resonances. In general it is obvious when there is a false detection or bad fit. A width which is very large or small in comparison to the other points making up the PEC can be discounted as a bad fit. There is, however, the possibility that significant changes in the magnitude of the width can occur as a state crosses a threshold and these points should not be discounted.

5.4 Results, discussion and comparison with previous work

5.4.1 Potential energy curves and quantum defects

Table 5.1 gives a comparison of equilibrium energies and quantum defects of the Rydberg states with the limited experimental data available. Agreement is generally good. It is expected that the agreement with experimental data, if it was available, would increase for higher n as shown for $\mathrm{c}'_\mathrm{n}\ {}^1\Sigma_\mathrm{u}^+$ series in table 4.2 of chapter 4. The equilibrium energy of A ${}^2\Pi_\mathrm{u}$ state is 0.07825 eV above the experimental value given in Huber and Herzberg (1979) in the target model (see section 4.2.1 of 4), this contributes to the disagreement with experiment of the Rydberg states converging on the A state. The equilibrium positions for the Rydberg states ${}^1\Sigma_\mathrm{u}^+(4\mathrm{s}\sigma_\mathrm{g})$ and ${}^1\Sigma_\mathrm{u}^+(4\mathrm{d}\sigma_\mathrm{g})$ were very close in energy and internuclear separation to the A ${}^2\Pi_\mathrm{u}$ state. As TIMEDEL does not function reliably close to thresholds for reasons described in section 3.2 of chapter 3, the equilibrium positions of these Rydberg states are only estimated.

Resonant states of singlet and triplet symmetries appear in figures 5.4 and 5.5 respectively. A comparison between the calculated curves and those of Guberman (2012) is also given. Although the curves largely appear to be solid lines, the resonant positions, coloured black, are simply represented by single points. The coloured lines from this work are the points joined together, no formal diabatisation has been performed; the many avoided crossings are simply interpolated using a straight lines. Many states not presented by Guberman are also given. In most cases this data can be separated into $D_{\infty h}$ symmetry states by matching up degenerate resonant positions. As this is a numerical technique the positions are not exactly degenerate. However, by considering the avoided crossings with other adiabats of the same symmetry and the quantum defects, symmetry assignments can be made unambiguously in almost all cases.

For the singlet states, the general agreement between this work and Guberman's is reasonable, except for the b′ $^1\Sigma_u^+$ state. The calculations presented here suggest that this state is bound and does not appear above the ionisation threshold, the position and shape of this curve in the bound region is in good agreement with that of Spelsberg and Meyer (2001), see figure 4.6 in chapter 4, adding confidence to this assertion. The position of Guberman's curve is similar to that of the $3d\pi_g$ Rydberg state converging on the B state. It is possible that due to the adiabatic nature of the MRCI approach that the state presented in Guberman (2012) is a combination of this Rydberg state and the valence state. This highlights an advantage of using a scattering calculation to find the neutral states above the ionisation threshold; it is easily seen that this state is part of a Rydberg series converging on the first excited state and not a valence state. This is confirmed by the narrow width of this state (~ 5 meV) normally associated with Rydberg states.

Again for the triplet states the agreement with Guberman is generally good, with particularly good agreement for the 1 $^3\Sigma_g^+$ and G $^3\Delta_g$ states. The crossing point of the main DR dissociative channel, 2 $^3\Pi_u$, is similar. However, there is a large disparity between the shape and position of states of 3 $^3\Pi_g$ symmetry, such a large level of disagreement is unusual. As there is no experimental data for these states it is difficult to make a judgement as to which or even if either of these states are correct.

Resonances of Σ^- symmetry states lying in the continuum are a special case. It is not possible to form Σ^- states by coupling a one-electron continuum orbital to the ground X $^2\Sigma_g^+$ state, all states of $^1\Sigma_g^-$, $^1\Sigma_u^-$, $^3\Sigma_g^-$ and $^3\Sigma_u^-$ symmetry cannot autoionise below the threshold to the A $^2\Pi_u$ state. These resonances therefore become bound states in the continuum and are not detected by any of the resonance fitting techniques employed. Since none of these resonances appear important for DR (for example they have zero coupling at low energies), there was not an attempt to map out these states in the low-energy region and curves simply stop at the A $^2\Pi_u$ state, see examples of $^1\Sigma_g^-$ and $^3\Sigma_g^-$ in, respectively, figures 5 and 6 below. It should be fairly straightforward to interpolate between the resonance curves and the bound states if full curves are required.

'Intruder' states, also known as interloper resonances, are Rydberg states that appear below an ionic state below the one on which they converge; for N_2 they appear in all symmetries. The $^{1,3}\Sigma_g^+$ interloper resonances of N_2 have been described previously at a single internuclear separation by Ballance et al. (1998). These interloper resonances are due to the close proximity in energy of the X, A and B states and lead to complicated state mixing as they overlap below each ionisation threshold.

Finally by matching the data using quantum defects, see section of chapter 4 for a more detailed description of this procedure, to form adiabats and combining it with bound adiabats discussed in chapter 4 a complete picture of the electronic states of N_2 above and below the ionisation threshold can be obtained, see figure 5.6. This figure shows that the R-matrix method can be used to create a comprehensive map of highly excited Rydberg-valence type neutral states for diatomic molecules and sets a benchmark for further calculations of this type.

5.4.2 Electronic resonance widths

Figure 5.3 gives a comparison of the three methods of resonance detection and a comparison with the widths of Guberman (2012) for the $^3\Pi_u$ symmetry. The 2 $^3\Pi_u$ state is the dominant dissociating channel in the DR of N_2^+ (see chapter 6 and (Guberman, 2012)) and hence the magnitude of this width will have a significant affect on the cross-section. For reasons explained in section 5.2.2, the approximations made by the QB method are not suitable for N_2. This is reconfirmed by the widths being around half the magnitude of those found by RESON and TIMEDEL. RESON and TIMEDEL give the same positions and widths as they are calculated using the same K-matrices unlike the QB method. However, at the points where the states are interacting with others and overlapping significantly, for example above 1.19 Å in the plot of the 4 $^3\Pi_u$ state, RESON fails to resolve the position and width.

TIMEDEL and RESON both reveal a significant amount of structure in the widths as they cross the Rydberg series converging on each threshold. The energy spacing of the Rydberg states is proportional to $^1/_{n^3}$, meaning that close to the threshold resolving individual resonances becomes intractable. The behaviour of the resonances is left undescribed slightly above and below each threshold. For resonant positions this is less of a problem as the shape of the PEC is generally predictable across the threshold. The behaviour of widths can change dramatically across a threshold as can be seen in figure 5.3; as the 3 and 4 $^3\Pi_u$ states cross the A state their width decreases significantly as the number of channels available for autoionisation decreases.

To compare with widths calculated by Guberman (2012) only open channels from the data provided are included above each threshold. That is, above the A state the widths are a sum of the X and A state widths and below the A state only the X state. For the 2 and 4 $^3\Pi_u$ states, Guberman's widths are systematically larger than ours and smooth. Conversely, agreement for the narrowest 3 $^3\Pi_u$ is good. In Guberman's characterisation, these resonances continue to have a width below the ionisation threshold, in terms of the purely electronic behaviour considered here this is not possible as bound electronic states have zero (electronic) widths. In general, it is expected that the width of a resonance will decrease as the number of open channels decreases

Table 5.1: Equilibrium energies, E_e (eV), internuclear separations, R_e (Å) and, quantum defects, α, of some Rydberg states converging upon excited states of N_2^+ compared to experiment. The equilibrium energy is given relative to the zero point energy of the X $^2\Sigma_g^+$ state. All states converge upon A $^2\Pi_u$ unless specified otherwise.

	This work			Experiment[a]		Comparison[b]	
State	E_e	R_e	α	E_e	α	ΔE_e	$\Delta\alpha$
$^3\Pi_u(5s\sigma_g)$	0.2914	1.182	1.1620	0.20	1.15	−0.0914	−0.0120
$^1\Pi_u(5s\sigma_g)$	0.3164	1.182	1.1093	0.25	1.05	−0.0664	−0.0593
$^3\Pi_u(6s\sigma_g)$	0.6327	1.182	1.1671	0.54	1.16	−0.0927	−0.0071
$^1\Pi_u(6s\sigma_g)$	0.6454	1.182	1.1136	0.57	1.03	−0.0754	−0.0836
$^1\Sigma_u^+(4s\sigma_g)^{c,d}$	1.6017	1.085	1.0506	1.57	1.08	−0.0032	0.0294
$^1\Sigma_u^+(4d\sigma_g)^{c,d}$	1.7942	1.087	0.8517	1.73	—	−0.0642	—

[a] Lofthus and Krupenie (1977).
[b] Obs. − Calc..
[c] Converges upon B $^2\Sigma_u^+$.
[c] Converges upon B $^2\Sigma_u^+$.
[d] Estimated as equilibrium position is close to A $^2\Pi_u$.

unless the width is dominated by a channel associated with the ground state. A decrease in open channels occurs as the state crosses a threshold. For 3,4 $^3\Pi_u$ there is a significant drop in width as they cross the B state, for 2 $^3\Pi_u$ the width remains fairly constant across the threshold showing that the dominant channel is associated with the X state. This decrease is seen in the 3 and 4 $^3\Pi_u$ states in Guberman's results whilst there is a general increase in resonance width with internuclear separation for the 2 $^3\Pi_u$.

Figure 5.7 shows PECs and widths for the $^1\Delta_u(nd\pi_g)$ and $^1\Delta_u(nd\delta_g)$ states converging on the A and B state respectively. This plot shows the detailed structure of the widths as these two Rydberg series interact. Each curve has been matched using quantum defect, the width-adiabat of each PEC has then been plotted in the lower panel. In this region of bond lengths, on average, the $nd\delta_g$ series (coloured in the plot) has a larger width than that of the $nd\pi_g$ series. As the $nd\delta_g$ series crosses the width rapidly increases and plateaus as it becomes the dominant electronic configuration of the adiabat and then rapidly decrease as it smoothly transitions back to $nd\pi_g$. The Rydberg series itself is reflected in the structure of the widths, with a series of plateaus decreasing in size for each value of n. Even with the dense grid of internuclear separations used it is not fine enough for the plateaus close to the thresholds to be resolved. This kind of detailed width structure is only possible to obtain using TIMEDEL and a dense grid of internuclear separations.

5.5 Conclusion

Three different methods for detecting and fitting singlet and triplet continuum states above the ionisation threshold of N_2 have been presented. The most comprehensive of these methods, the time-delay method, provides a highly detailed mapping of the resonance structure and widths. Comparison with the very limited experimental data available is good. The use of a dense grid and an improved fitting method presented in chapter 3 reveals complicated structures in the widths and a description of their adiabatic nature with changing electronic configuration. Neutral states which could provide routes to dissociation in a DR calculation have been identified and compared with those given by Guberman (2012). In general agreement in position for the main dissociative states is good, but narrower widths with much more pronounced structure have been found. These differences should affect calculated DR cross-sections.

The data presented in this chapter and the previous one when combined, provides all of the parameters needed to calculate the DR cross-section N_2^+. In the following chapter this calculation will be presented.

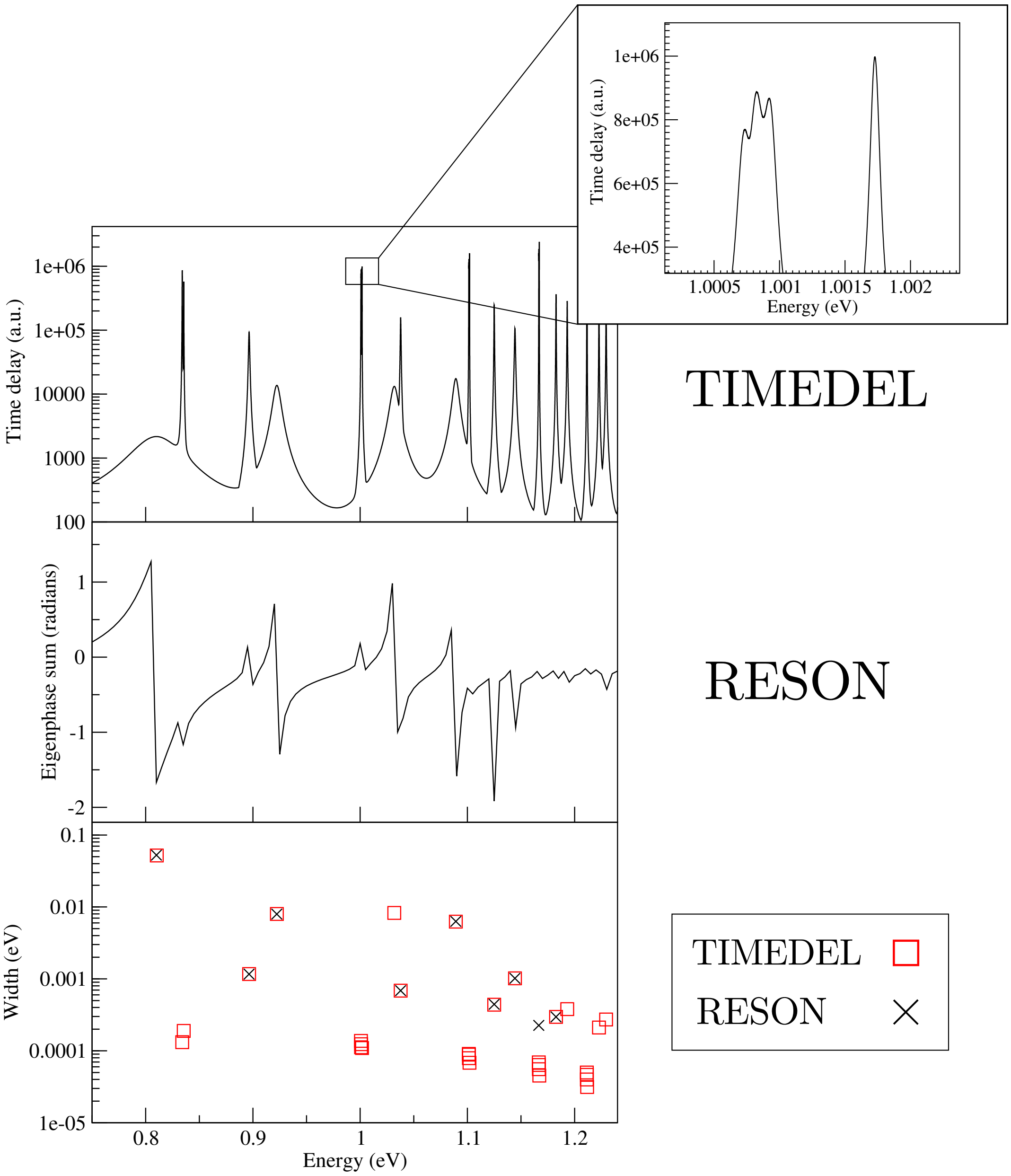

Figure 5.2: Comparison of the time-delay and eigenphase sum for the same energy range (top two panels) with fitted widths (lowest panel). The inset plot shows a zoom of one of the time-delay peaks. At high energies, close to the threshold, the resonances are narrow, close in energy, and overlap. As a result the eigenphase sum becomes impossible to interpret and unsuitable for fitting. The very fine energy grid used by TIMEDEL means that close-spaced narrow resonances, such as those shown in the inset plot, can be resolved. As shown in the plot of widths, the very narrow resonances ($\lesssim$ 0.2 meV), even at energies far from ($\sim$ 0.85 eV) the threshold are only detected by TIMEDEL.

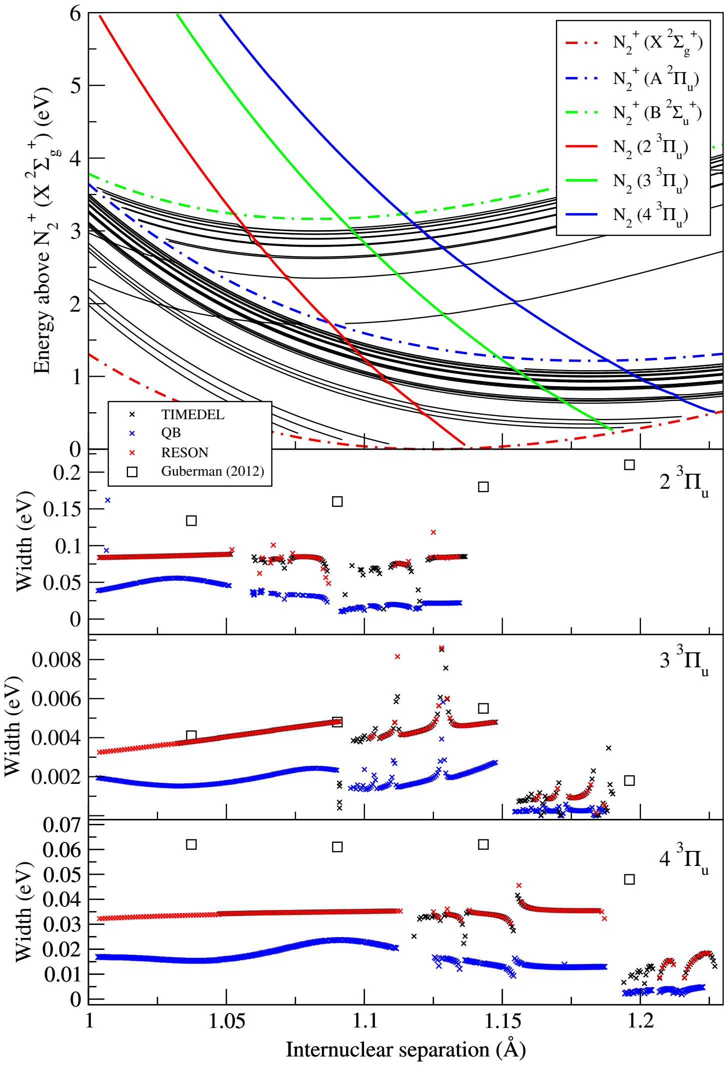

Figure 5.3: Potential energy curves of $^3\Pi_u$ symmetry with their respective widths and a comparison with widths calculated by Guberman (2012) .

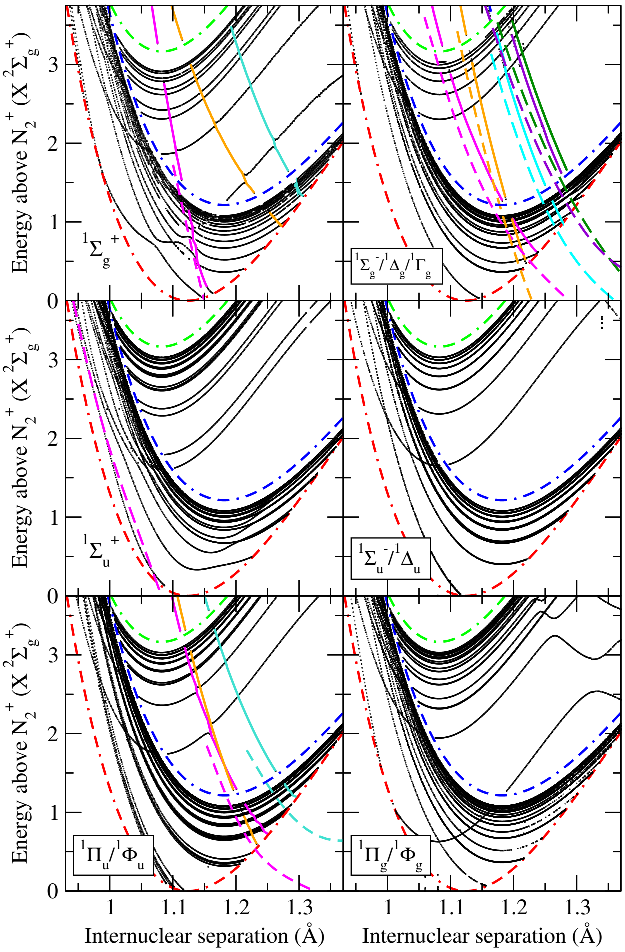

Figure 5.4: Potential energy curves for each of the singlet symmetries. Dashed and dotted lines are the N_2^+ states: X $^2\Sigma_g^+$ (red), A $^2\Pi_u$ (blue) and B $^2\Sigma_u^+$ (green). The dissociative valence states are highlighted in colour. Solid lines are this work and broken lines are curves by Guberman (2012). Although, in places, the data series coloured in black showing the Rydberg states look like solid lines they are actually just single points in a dense grid of internuclear separations. The valence states are assigned as follows. $^1\Sigma_g^+$: — a $^1\Sigma_g^+$ (labelled as 2 $^1\Sigma_g^+$ by Guberman (2012)), — 2 $^1\Sigma_g^+$, — 3 $^1\Sigma_g^+$. $^1\Sigma_g^-/^1\Delta_g/^1\Gamma_g$: — 1 $^1\Delta_g$, — 1 $^1\Gamma_g$, — 2 $^1\Delta_g$, — 3 $^1\Delta_g$, — 1 $^1\Sigma_g^-$. $^1\Sigma_u^+$: — b′ $^1\Sigma_u^+$ (in this work this state is bound and hence does not appear on the plot). $^1\Pi_u/^1\Phi_u$: — 2 $^1\Pi_u$, — 1 $^1\Phi_u$, — 3 $^1\Pi_u$.

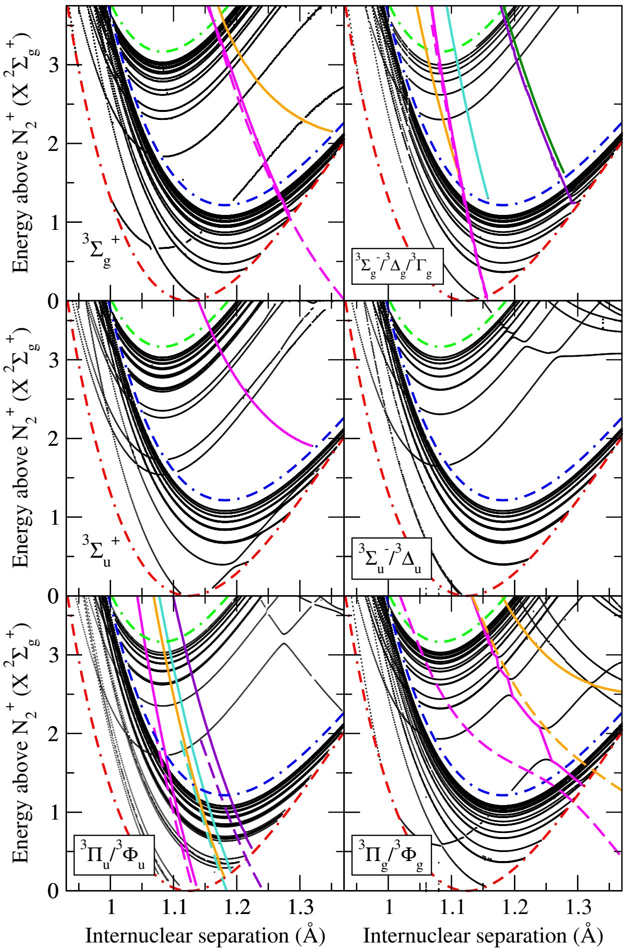

Figure 5.5: Potential energy curves for each of the triplet symmetries. Dashed and dotted lines are the N_2^+ states: X $^2\Sigma_g^+$ (red), A $^2\Pi_u$ (blue) and B $^2\Sigma_u^+$ (green). The dissociative valence states are highlighted in colour. In some cases Guberman has only presented a single curve of each symmetry and not assigned a letter or number prefix. In this case the curve corresponds to the curve in the this work with the prefix '1'. Solid lines are this work and broken lines are curves by Guberman (2012). Although, in places, the data series coloured in black showing the Rydberg states look like solid lines they are actually just single points in a dense grid of internuclear separations. The valence states are assigned as follows. $^3\Sigma_g^+$: — 1 $^3\Sigma_g^+$, — 2 $^3\Sigma_g^+$, — 3 $^1\Sigma_g^+$. $^3\Sigma_g^-/^3\Delta_g/^3\Gamma_g$: — G $^3\Delta_g$, — 1 $^3\Sigma_g^-$, — 2 $^3\Sigma_g^-$, — 3 $^3\Delta_g$, — 3 $^3\Sigma_g^-$. $^3\Sigma_u^+$: — 1 $^3\Sigma_u^+$. $^3\Pi_u/^3\Phi_u$: — 2 $^3\Pi_u$, — H $^3\Phi_u$, — 3 $^3\Pi_u$, — 4 $^3\Pi_u$. $^3\Pi_g/^3\Phi_g$: — 2 $^3\Pi_g$, — 3 $^3\Pi_g$.

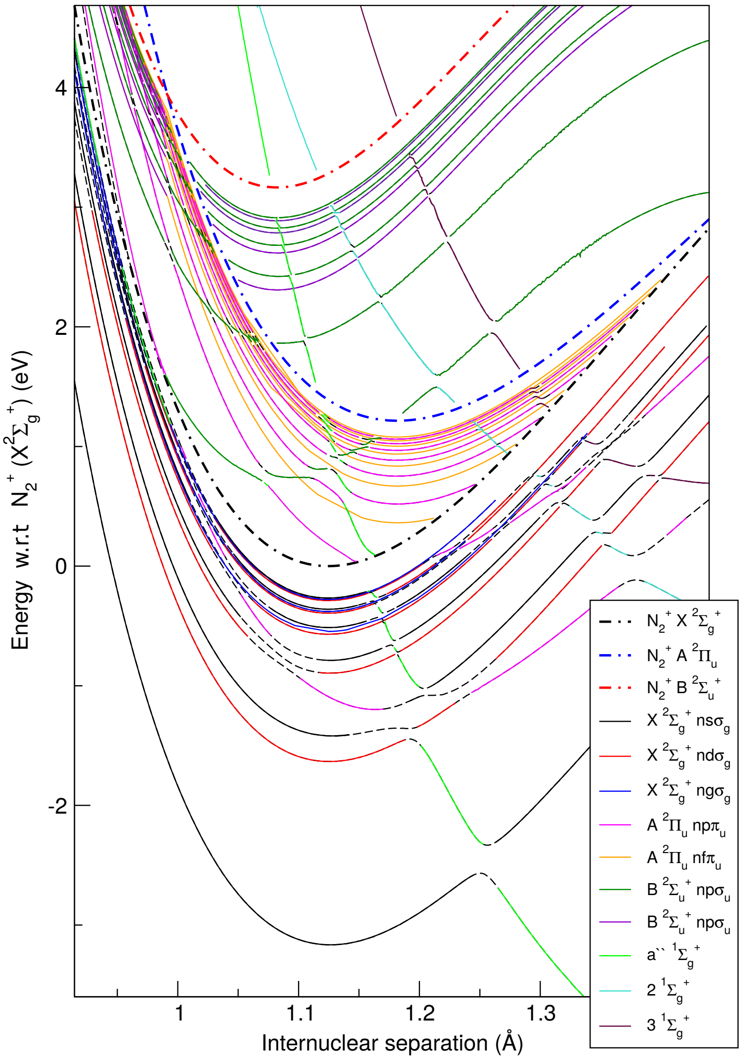

Figure 5.6: A complete description of the electronic structure of N_2 above and below the ionisation threshold for states of ${}^1\Sigma_g^+$ symmetry. Data was matched by quantum defect to form adiabats, the colours show the diabatic states.

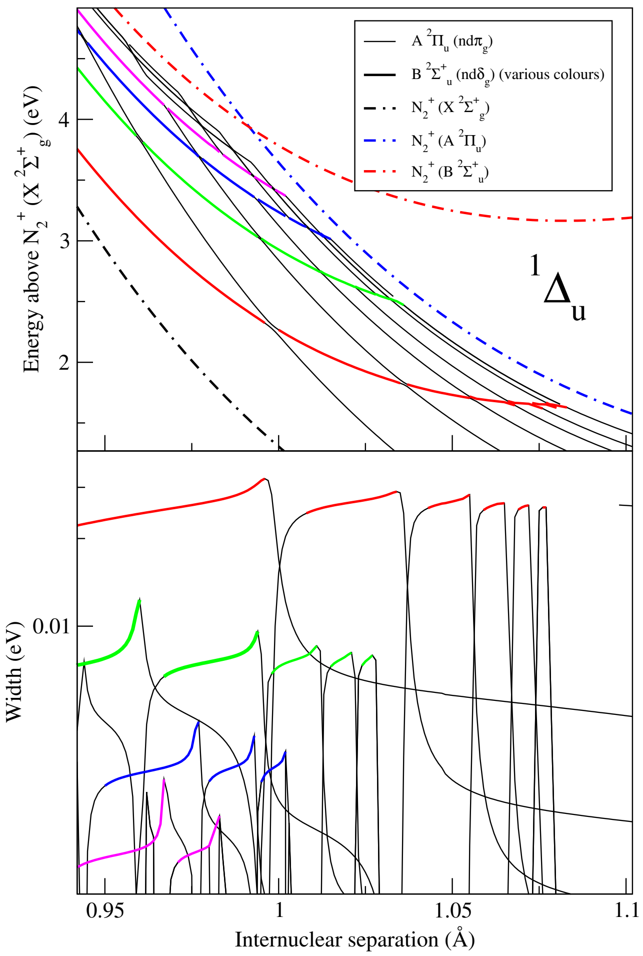

Figure 5.7: Interacting Rydberg series and their widths for total symmetry $^1\Delta_u$. On the top panel are the PECs of A $^2\Pi_u$ ndπ_g Rydberg series (narrow black lines) interacting with the A $^2\Pi_u$ ndδ_g Rydberg series (thick coloured lines). Sections of the width-adiabats displayed in the lower panel are coloured coded to the Rydberg state they are associated with. The structure of the Rydberg series is represented in the widths as a series of plateaus decreasing in magnitude.

Chapter 6

Computing dissociative recombination cross-sections

6.1 Introduction

In this chapter a description is given of the calculation of the cross-sections for the dissociative recombination (DR) of N_2^+ using multichannel quantum defect theory (MQDT) with the molecular data generated in chapters 4 and 5. The cross-section is calculated for four initial vibrational states of the ion, $v_i^+ = 0 - 3$. The calculation was carried out using the MQDT code of K. Chakrabarti and I. F. Schneider with contributions from J. Zs. Mezei (Chakrabarti et al., 2013).

The focus of this chapter is to demonstrate how molecular data from an R-matrix data calculation can be prepared and input to produce a completely *ab initio* DR cross-section. The resulting cross-section is in excellent agreement with experimental and other theoretical results, as shown in the comparisons made below.

This chapter is organised as follows: first, a brief theoretical exposition is given of the cross-section calculation using MQDT. Secondly a description of how the data from the R-matrix calculations is prepared for its use in an MQDT calculation. Third, a brief summary of computational details followed by the results with a discussion. Conclusions are made at the end of the chapter.

All data presented in this chapter is available in the supplementary data of Little et al. (2014).

6.2 The multichannel quantum defect approach to dissociative recombination

As the focus of this thesis has been to produce molecular data which could then be applied to a dissociative recombination calculation, the theoretical details of MQDT are only given here briefly For a more in depth discussion the reader is directed to the following references: Giusti (1980), Schneider et al. (2000), Motapon et al. (2006), Florescu-Mitchell and Mitchell (2006) and Larsson and Orel (2008). The following theoretical exposition is largely derived from Giusti (1980) and Florescu-Mitchell and Mitchell (2006).

The DR calculation is restricted to the case where the energy of the incident electron is lower than the dissociation energy of the target ion, considered to be in its ground electronic state. The collision process involves two mechanisms (see section 1.2 of chapter 1 for a qualitative description): (a) the direct process, where the incoming electron is captured in a doubly excited neutral dissociative state N_2^{**} which either autoionises or leads to two neutral N atoms,

$$\mathrm{N}_2^+(\mathrm{v}_\mathrm{i}^+) + \mathrm{e}^- \rightarrow \mathrm{N}_2^{**} \rightarrow \begin{cases} \mathrm{N} + \mathrm{N}^* \\ \mathrm{N}_2^+(\mathrm{v}_\mathrm{f}^+) + \mathrm{e}^-, \end{cases} \tag{6.1}$$

(b) the indirect process, where the incident electron is temporarily captured into a singly excited bound Rydberg state N_2^*, predissociated by N_2^{**} :

$$\begin{aligned} \mathrm{N}_2^+(\mathrm{v}_\mathrm{i}^+) + \mathrm{e}^- \rightarrow \mathrm{N}_2^* &\rightarrow \mathrm{N}_2^{**} \\ \mathrm{N}_2^{**} &\rightarrow \begin{cases} \mathrm{N} + \mathrm{N}^* \\ \mathrm{N}_2^+(\mathrm{v}_\mathrm{f}^+) + \mathrm{e}^-. \end{cases} \end{aligned} \tag{6.2}$$

In MQDT, instead of considering electronic configurations interacting, the problem is written in terms of channels. Both direct and indirect processes involve two different types of channels, namely dissociation and ionisation channels. A channel is open if the total energy of the molecular system is higher than the energy of its fragmentation threshold, and closed in the opposite case. A closed ionisation channel introduces into the calculation a series of Rydberg states differing only by the principal quantum number of the external electron (Schneider et al., 1994). Hence, the inclusion of the closed channels allows for the indirect mechanism, which interferes with the direct mechanism resulting in the total process.

The problem is split up into three separate space regions defined as follows (Florescu-Mitchell and Mitchell, 2006), see figure 6.1:

Region I: The inner reaction zone, both the electron coordinate, r, and the internuclear separation, R are limited by some finite value (r_0, R_0) on the order of tens of *a.u.*. In this region all many body interactions are taken into account and the Born-Oppenheimer approximation is valid

Region II: The outer reaction zone, $r > r_0$ (but finite) and $R < R_0$. The external electron is under the influence of the Coulomb potential of the nuclei and also the finite range potential of the electrons of the ion, $V(R)$. It is the short-range interaction region for the nuclei and motion of the electron is coupled to that of the ion. The Born-Oppenheimer approximation is no longer valid.

Region III: The asymptotic zone, the external electron is now only under the influence of the isotropic Coulomb potential of the ion. Asymptotic boundary conditions are applied to describe an ionisation event, $r \to \infty$. The interaction potential between nuclei vanishes and at $R \to \infty$, the molecule dissociates.

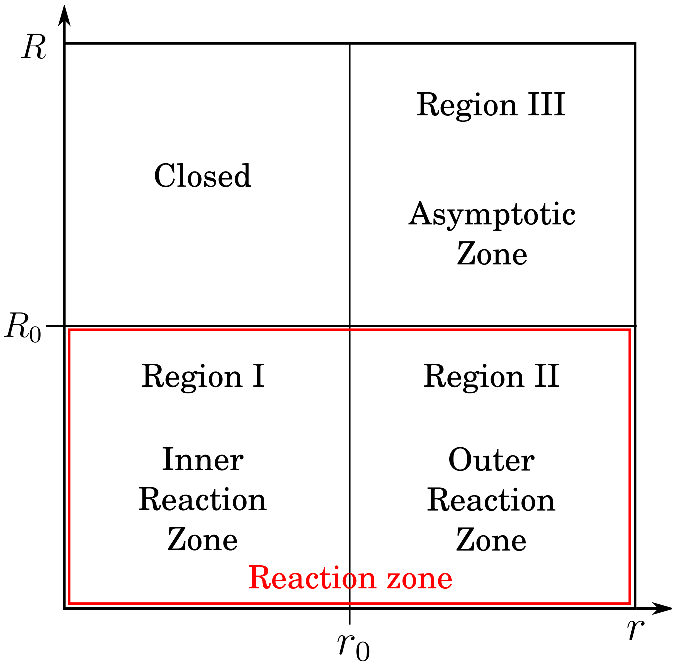

Figure 6.1: The relevant reaction regions in terms of internuclear separation (y-axis) and external electron coordinate (x-axis). $R > R_0$, $r > r_0$ is closed as the external electron is always bound to a nuclei as the molecule dissociates.

The effect of the channel interaction is 'imprinted' on the channel wavefunctions in region I. The imprint on the wavefunction comes in the form of a phase shift $\pi\mu$; in the reaction zone (regions I and II) μ is the quantum defect of the ionisation channels, that is, the Rydberg series of the ion. The defining principle of MQDT is the interpolation of this quantum defect for negative electron energies (bound states) to the scattering phase shift for positive electron energies across the ionisation potential of the ion. This is possible as the quantum defect is weakly dependent on the energy of the external electron ϵ.

The wavefunction of region II can be written in terms of a superposition of channel wavefunctions that contain the phaseshift imprinted on the wavefunction in region I. This channel wavefunction can then be determined by building a K-matrix based on the vibronic interaction between the ionisation and dissociation channels. Once this K-matrix has been diagonalised the solutions on the edge of the reaction zone are matched to asymptotic solutions using a frame transformation. The projection coefficients of this frame transformation form a scattering matrix which then gives cross-sections.

6.2.1 One-channel case

For the one channel case, H_0 is a one-electron radial Hamiltonian, $V(r)$ is a strong but short ranged potential; $V(r) = 0$ for $r > r_0$. Beyond the range of this potential, subject only to the Coulomb attraction of the nucleus, the wavefunction of the system has the form,

$$\phi_E(r) = f_E(r)\cos\eta - g_E(r)\sin\eta, \qquad r > r_0. \tag{6.3}$$

where η is the phase shift due to the short range potential, $V(r)$. This is a superposition of regular and irregular solutions; the function g lags behind f with a phase of $\frac{\pi}{2}$ so that the asymptotic behaviour of the wavefunction is,

$$\phi_E(r) \sim A(E)\sin(kr + \delta(E) + \eta(E)), \tag{6.4}$$

where $\sim$ indicates the asymptotic behaviour of the wavefunction. $\delta(E)$ is the phase shift due to Coulomb attraction of the nucleus.

The ratio of the coefficients f and g gives the K-matrix for a collision of energy E,

$$\tan\eta(E) = -\pi K(E). \tag{6.5}$$

6.2.2 Multiple-channel case

In the multiple-channel case, the total wavefunction of a given channel is denoted by φ_{iE}. This wavefunction consists of a 'core' wavefunction of the ion multiplied by a one particle continuum wavefunction. The continuum can be either electronic or nuclear.

The additional interaction between channels, V, is accounted for by adding a superposition of conjugated wavefunctions $\bar{\varphi}_{jE}$; $\bar{\varphi}_{jE}$ have the same total energy as φ_{iE} and are found by dephasing the continuum factors by $\frac{\pi}{2}$. The wavefunction is then

$$\psi_{iE} = \varphi_{iE} + \sum_j \pi K_{ji}(E)\bar{\varphi}_{jE}, \tag{6.6}$$

$K_{ji}(E)$ is the $N \times N$ reaction matrix associated with interaction V, where N is an orthonormal channel.

To represent the results of the short range interaction in terms of phaseshifts (as in the one channel case) the K-matrix is diagonalised with eigenvalues $-\pi\tan\eta_\alpha$ and unitary eigenvectors $U_{i\alpha}$, where $\alpha = 1, \ldots, N$,

$$\sum_j \pi K_{ji} U_{\alpha j} = -\tan \eta_\alpha U_{i\alpha}. \tag{6.7}$$

The wavefunction ψ_i (eq. (6.6)) is then written in terms of N eigenchannel functions

$$\psi_\alpha = \sum_i U_{i\alpha} \psi_i B_\alpha, \tag{6.8}$$

where the energy dependence has been omitted and B_α is the normalisation condition $B_\alpha = \cos \eta_\alpha$. With the use of eq. (6.7), ψ_α can then be written

$$\psi_\alpha = \sum_i U_{i\alpha} (\varphi_i \cos \eta_\alpha - \bar{\varphi}_i \sin \eta_\alpha). \tag{6.9}$$

Now consider a DR process with N_{el} ionisation channels and N_d dissociation channels to give $N = N_{el} + N_d$ channels in total. In region I, the short-range potential is the short range Rydberg-valence interaction, that is the interaction between dissociative and ionisation channels; first of all accounted for on the electronic level:

$$V(R) = \langle \Phi_{d_j} | H_{el} | \Phi^{el/ion} \rangle, \tag{6.10}$$

which is assumed to be independent of the energy of the external electron and the integration is performed over the electronic coordinates of the neutral (electron + ion) system. Here H_{el} denotes the electronic Hamiltonian, Φ_{d_j} is the electronic wavefunction of the dissociative state and $\Phi^{el/ion}$ the wavefunction describing the electron-ion system. This energy independent coupling is related to the autoionisation width found in chapter 5 by (Larsson and Orel, 2008),

$$V(R) = \sqrt{\frac{\Gamma(R)}{2\pi}}. \tag{6.11}$$

Using the result for the multichannel case described above (eq. (6.9)), the wavefunction of an electron emerging from region I to region II can be expressed as linear combination of regular and irregular Coulomb functions with a phase shift $\pi\mu$. The wavefunction for an ionisation channel in region II is defined as:

$$\psi_v^{II} = \chi_v(R) \phi_{core}(q^+, R) (f_l(\nu, r) \cos \pi\mu(R) - g_l(\nu, r) \sin \pi\mu(R)), \qquad r > r_0, \tag{6.12}$$

where μ is the quantum defect. v denotes an ionisation channel; $\chi_v(R)$ is a bound vibrational wavefunction associated with ionisation channel v; $\phi_{core}(q^+, R)$ is the electronic wavefunction of the ion where q^+ are the electron coordinates of the ion; f_l, g_l are Coulomb functions where $\nu = (-2\epsilon)^{-1/2}$. As the channels are now mixed due to the coupling in eq. (6.10), with reference to eq. (6.9) a new set of mixed channel wavefunctions can be defined for region II:

$$\psi'^{II}_{\alpha} = \sum_{v} U_{v\alpha}[\psi^{II}_{v} \cos\eta_{\alpha} - \bar{\psi}^{II}_{v} \sin\eta_{\alpha})] + \sum_{i} U_{d_i\alpha}[\psi_{d_i} \cos\eta_{\alpha} - \bar{\psi}_{d_i} \sin\eta_{\alpha}]. \tag{6.13}$$

where

$$\bar{\psi}^{II}_{v} = \chi_{v}(R)\phi_{core}(q^{+}, R)(f_l(\nu, r)\cos\pi\mu(R) + g_l(\nu, r)\sin\pi\mu(R)) \tag{6.14}$$

and the dissociative channels are written,

$$\psi_{d_i} = \Phi_{d_i}(q, R)F_{d_i}(\kappa_i, R), \tag{6.15}$$

$\Phi_{d_i}(q, R)$ is the electronic wavefunction of a neutral dissociative electronic state d_i, $F_{d_i}(\kappa_i, R)$ is the nuclear wavefunction for the relative motion of two atoms of reduced mass M, $\kappa_i = \sqrt{2M(E - E_{d_i})}$. $F_{d_i}(\kappa_i, R)$ is the solution to the nuclear Schrodinger equation with repulsive dissociative potential $U_{d_i}(R)$;

$$\left(-\frac{1}{2M}\frac{d^2}{dR^2} + U_{d_i}(R) - E\right) F_{d_i}(\kappa_i, R) = 0. \tag{6.16}$$

By determining and diagonalising the K-matrix, eq. (6.7), the phase shifts η_{α} and channel eigenvectors can be found. This is equivalent to determining the form of the total wavefunction of the system in region II, eq. (6.13), (Florescu-Mitchell and Mitchell, 2006).

The K-matrix, $\boldsymbol{\mathcal{K}}$, is built by first determining the vibronic coupling between the ionisation and dissociation channels, this is given as the interaction matrix $\boldsymbol{\mathcal{V}}$,

$$\mathcal{V}_{d_j,v}(E) = \langle F_{d_j}(E)|V(R)|\chi_{\nu}\rangle. \tag{6.17}$$

between χ_{ν}, the vibrational wavefunction associated with an ionisation channel and F_{d_j} the radial wavefunction (see eq. (6.15)) of the dissociative state d_j. $V(R)$, is from eq. (6.18).

The short-range reaction matrix, $\boldsymbol{\mathcal{K}}$, can then built as a solution of the Lippmann-Schwinger equation

$$\boldsymbol{\mathcal{K}} = \boldsymbol{\mathcal{V}} + \boldsymbol{\mathcal{V}}\frac{\mathbf{1}}{\boldsymbol{E} - \boldsymbol{H_0}}\boldsymbol{\mathcal{K}}, \tag{6.18}$$

where H_0 is the zero-order Hamiltonian of the molecular system. For an energy-independent coupling $V(R)$, eq. (6.18), has a perturbative solution which is exact to second-order (Ngassam et al., 2003).

The diagonalised K-matrix eigen-pairs give the the phase shifts, η_{α}, and channel eigenvectors. Eq. 6.13 can then be written

$$\psi'^{II}_{\alpha} = \sum_{v} U_{v\alpha}[f_l(\nu,r)\cos(\pi\mu(R)+\eta_\alpha) - g_l(\nu,r)\sin(\pi\mu(R)+\eta_\alpha)] + \tag{6.19}$$

$$\sum_{i} U_{d_i\alpha}\Phi_{d_i}(q,R)[(F_{d_i}(\kappa_i,R)\cos\eta_\alpha - G_{d_i}(\kappa_i,R)\sin\eta_\alpha]. \tag{6.20}$$

To move the solutions from region II to the asymptotic region, region III, a frame transformation must be performed. The frame transformation transforms the motion of the electron in region II which is coupled to the nuclear motion via the quantum defect, to region III where it is only under the influence of the Coulomb potential and therefore its wavefunction is R independent. This frame transformation is performed via the projection coefficients (Giusti, 1980),

$$\mathcal{C}_{v^+,\alpha} = \sum_{v} U_{v,\alpha}\langle\chi_{v^+}|\cos(\pi\mu+\eta_\alpha)|\chi_v\rangle, \tag{6.21}$$

$$\mathcal{C}_{d_j,\alpha} = U_{d_j,\alpha}\cos\eta_\alpha, \tag{6.22}$$

$$\mathcal{S}_{v^+\alpha} = \sum_{v} U_{v,\alpha}\langle\chi_{v^+}|\sin(\pi\mu+\eta_\alpha)|\chi_v\rangle, \tag{6.23}$$

$$\mathcal{S}_{d_j,\alpha} = U_{d_j,\alpha}\sin\eta_\alpha, \tag{6.24}$$

where χ_{v^+} are vibrational wavefunctions of the molecular ion. These can be grouped into matrices $\boldsymbol{\mathcal{C}}$ and $\boldsymbol{\mathcal{S}}$ which are the building blocks of the generalised scattering matrix $\boldsymbol{X}$ that involves all open ("o") and closed ("c") channels. The $\boldsymbol{X}$ matrix in turn can be arranged into four sub matrices

$$\boldsymbol{X} = \frac{\boldsymbol{\mathcal{C}} + \boldsymbol{i}\boldsymbol{\mathcal{S}}}{\boldsymbol{\mathcal{C}} - \boldsymbol{i}\boldsymbol{\mathcal{S}}} = \begin{pmatrix} \boldsymbol{X_{oo}} & \boldsymbol{X_{oc}} \\ \boldsymbol{X_{co}} & \boldsymbol{X_{cc}} \end{pmatrix}. \tag{6.25}$$

Imposing boundary conditions leads to the physical scattering matrix (Seaton, 1983):

$$\boldsymbol{S} = \boldsymbol{X_{oo}} - \boldsymbol{X_{oc}}\frac{\boldsymbol{1}}{\boldsymbol{X_{cc}} - \mathbf{exp}(\boldsymbol{-i2\pi\nu})}\boldsymbol{X_{co}}, \tag{6.26}$$

where the diagonal matrix $\boldsymbol{\nu}$ is constructed with the effective quantum numbers $\nu_{v^+} = [2(E_{v^+} - E)]^{-1/2}$ (in atomic units) associated with each vibrational threshold E_{ν^+} of the ion, situated above the current total energy E, labelling a closed channel.

For a molecular ion, initially in the vibrational state v_i^+, recombining with an electron of energy ε the cross-section of capture into all the dissociative states d_j of the same symmetry Γ (gerade/ungerade, singlet/triplet) and electronic angular momentum projection Λ can be written as (Schneider et al., 1997):

$$\sigma^{\Gamma,\Lambda}_{diss\leftarrow v_i^+} = \frac{\pi}{4\varepsilon}\rho^{\Gamma,\Lambda}\sum_{j}|S_{d_j,v_i^+}|^2, \tag{6.27}$$

where $\rho^{\Gamma,\Lambda}$ is the ratio between the spin multiplicities of the neutral and the target ion. The total cross-section for DR is obtained by summing over all available Γ, Λ:

$$\sigma^{sym}_{diss\leftarrow v_i^+} = \sum_{\Gamma,\Lambda} \sigma^{\Gamma,\Lambda}_{diss\leftarrow v_i^+}. \tag{6.28}$$

6.2.3 Inclusion of core excited states

It is possible to also include Rydberg states associated with excited states of the ion into the calculation using MQDT (see section 1.2 of chapter 1 for a qualitative description of this mechanism). For a detailed description of how this is done see Chakrabarti et al. (2013).

From a molecular data point of view, this involves including the additional coupling describing the interactions between ionisation channels associated with each state of the ion, the Rydberg-Rydberg couplings given by

$$\mathcal{V}^{\Lambda}_{vw} = \langle \chi_v | V^{\Lambda}_{c_1,c_2}(R) | \chi_w \rangle, \tag{6.29}$$

$$\mathcal{V}^{\Lambda}_{vu} = \langle \chi_v | V^{\Lambda}_{c_1,c_3}(R) | \chi_u \rangle, \tag{6.30}$$

$$\mathcal{V}^{\Lambda}_{wu} = \langle \chi_w | V^{\Lambda}_{c_2,c_3}(R) | \chi_u \rangle, \tag{6.31}$$

where the vibrational quantum numbers v, w and u label the ionisation channels of core 1, 2 and 3 (c_1, c_2 and c_3) respectively and χ is the vibrational wavefunction of each ionisation channel.

Secondly the Rydberg-valence coupling (eq. (6.10)) must be resolved by the Rydberg series associated with each ionic state,

$$\mathcal{V}^{\Lambda}_{d_j,w}(E) = \langle F_{d_j}(E) | V^{\Lambda}_{d_j,c_2}(R) | \chi_w \rangle, \tag{6.32}$$

$$\mathcal{V}^{\Lambda}_{d_j,u}(E) = \langle F_{d_j}(E) | V^{\Lambda}_{d_j,c_3}(R) | \chi_{u\cdot} \rangle, \tag{6.33}$$

where F_{d_j} is the radial wavefunction associated with each dissociative state j, see eq. (6.16).

6.3 Molecular data

The following set of parameters are needed for an MQDT calculation of the DR cross-section including the indirect process:

- The potential energy curves (PEC) of the ground state of the ion. This gives the vibrational wavefunction of the ion.
- The PECs of the neutral molecule providing routes to dissociation. This gives the wavefunction of the dissociative states.
- The electronic couplings between the neutral valence states and the Rydberg series converging to the ground state of the ion. These are the energy independent couplings (eq. (6.11)).

- The quantum defect of the Rydberg series converging on the ion as a function of R.

For a MQDT calculation which includes 'core-excited' bound states of the ion there is an additional requirement of;

- The PECs of the excited ion states. This gives the vibrational wavefunction of the excited ionic states.
- The electronic coupling between the valence states and the Rydberg series converging to each excited state of the ion (eq. (6.32) and eq. (6.33)).
- The Rydberg-Rydberg coupling between each series converging to each state of ion (eqs. (6.29), (6.30) and (6.31)).
- The quantum defects of the Rydberg series converging on the excited states of the ion as a function of R.

It should be noted that the implementation of MQDT used (Chakrabarti et al., 2013) only supports couplings between the ground state and the excited states, so the couplings given in eq. (6.31) were not included even though the data was available.

6.3.1 Potential energy curves

By combining the data from below (bound, chapter 4) and above (resonant, chapter 5) the ionisation threshold of N_2^+, a complete description of the super-excited neutral electronic states which are important for dissociative recombination is given. The states which cross the ion ground state at favourable positions can then be identified. In the following discussion the N_2^+ states X $^2\Sigma_g^+$, A $^2\Pi_u$ and B $^2\Sigma_g^+$ will be referred to as X, A, and B respectively. The chapters 4 and 5 will be referred to as I and II respectively.

To form smooth potential energy curves from the data presented in I and II it was necessary to fit the data with smoothing splines. The reasons for this were twofold. Firstly, as mentioned in section 2.2.1 of chapter 2, the R-matrix method works in the Born-Oppenheimer approximation and hence avoided crossings are present in the PECs. These avoided crossings were interpolated across using the smoothing spline, no formal diabatisation took place. Secondly for reasons described in detail in I and II, gaps in the data appear slightly above and slightly below the PEC of each electronic state of the ion. Therefore it was necessary to interpolate across these gaps. An example of a smoothing spline being fitted to the adiabatic curves given is given in figure 6.2.

To compute DR cross-sections, it is necessary to know the asymptotic behaviour of the PECs. The bound curves were extended using the R-matrix method in 'quantum chemistry (QC) mode', see section 2.4.1 of chapter 2. The advantage of using QC mode to extend the calculation to longer bond lengths is that it relies only on the diagonalisation of a Hamiltonian (Tennyson, 1996)

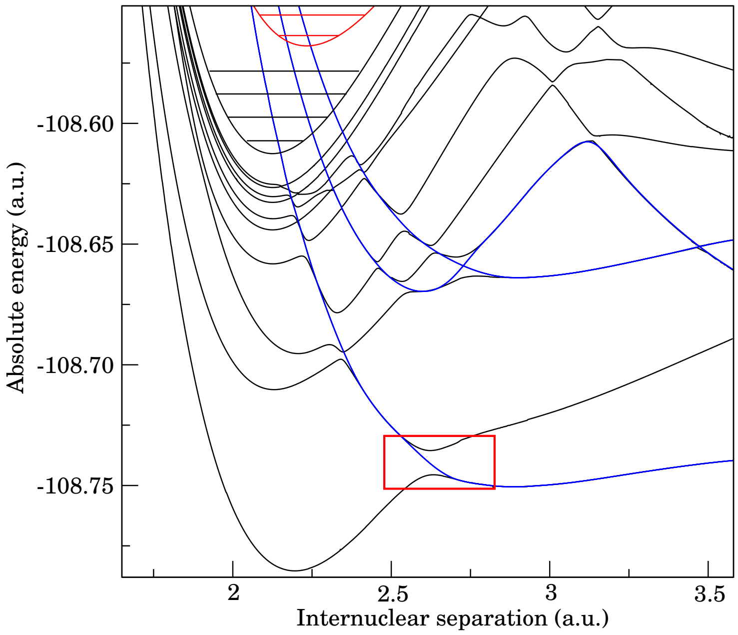

Figure 6.2: Example of spline fitting to the data presented in I, in this case for the symmetry $^3\Pi_u$. The avoiding crossings are interpolated across using a smoothing spline, no formal diabatisation is performed. The avoided crossing discussed in section 6.5.4 is highlighted by the red box.

to find energy eigenvalues which is more numerically stable than propagating and solving the R-matrix, and it does not suffer from problems with the target wavefunction leaking outside the R-matrix sphere at large internuclear separations. Therefore, when one is only interested in low-lying bound states at long bond lengths, where there is no influence of Rydberg states, QC mode is the preferred option. Despite this, issues do arise when performing QC mode calculations at large internuclear separations. As described in I, the number of target states used in an R-matrix calculation is arbitrary and their energetic order switches with internuclear separation leading to discontinuities in the calculated potential energy curves. Secondly the continuum orbitals which are placed at the center-of-mass of the molecule become less appropriate at longer bond lengths. As the information of interest is the asymptote the state converges upon and the asymptotic behaviour is easily predictable, these issues do not present significant problems.

The potential energy curves taken from the data given in I and II with their asymptotes, can be seen in figure 6.3 and figure 6.4.

6.3.2 Electronic couplings

For a DR calculation including multiple ionic cores it is necessary to use two types of coupling. Rydberg-valence couplings (eq. (6.11)) describe the coupling of the ionisation channels to valence or dissociative states. Rydberg-Rydberg couplings (eqs. (6.29), (6.30)) describe the coupling between ionisation channels of a given symmetry associated with each ionic state.

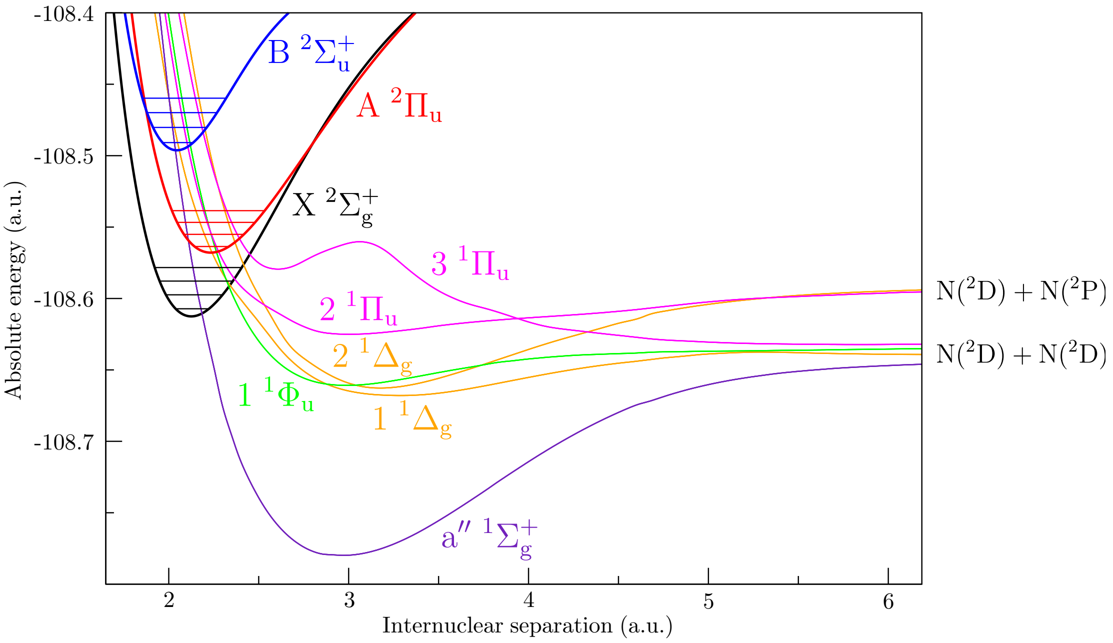

Figure 6.3: Singlet dissociative states included in the cross-section calculation with their asymptotic limits. The potential energy curves were taken from the data provided by I and II.

Rydberg-valence couplings

A discussed in II, resonances were calculated using the time-delay method of Smith (1960) using the module TIMEDEL discussed in chapter 3. Resonances appear as Lorentzians when the eigenvalues of the time-delay matrix are plotted against energy. These Lorentzians are fitted to find the autoionisation width, $\Gamma(R)$, of the resonance (see section 2.4.2 in chapter 2), where R is internuclear separation. The autoionisation width is then transformed into a Rydberg-valence coupling using eq. (6.11). The time-delay method also provides the branching ratio of the autoionisation to a partial wave through the square of the time-delay matrix eigenvector (see equation 3.2 in chapter 3). This means that the coupling can be resolved by autoionisation to a specific electronic state of the ion and then again to a specific partial wave associated with that state. In this study the coupling was only resolved to autoionise into a particular electronic state of the ion, see figure 6.5, this gives the couplings in eq. (6.32) and eq. (6.33).

Again, due to the reasons outlined in section 6.3.1 regarding the avoided crossings and gaps in data, it was necessary to fit the couplings with smoothing splines; an example is given in figure 6.5. There is a significant amount of structure in the couplings due to the adiabatic behaviour of the dissociative state interacting with Rydberg states as it passed through them; this structure was ignored, which can be thought of as a 'diabatisation of the couplings'. For more details on the adiabatic structure of the couplings see section 5.4.2 of II.

In the R-matrix method the electronic width of a resonance goes to zero below the ground state of the ion. Therefore couplings were forced to zero rapidly after the threshold had been crossed see figure 6.5. The couplings associated with each dissociative state are displayed in figure 6.6 and

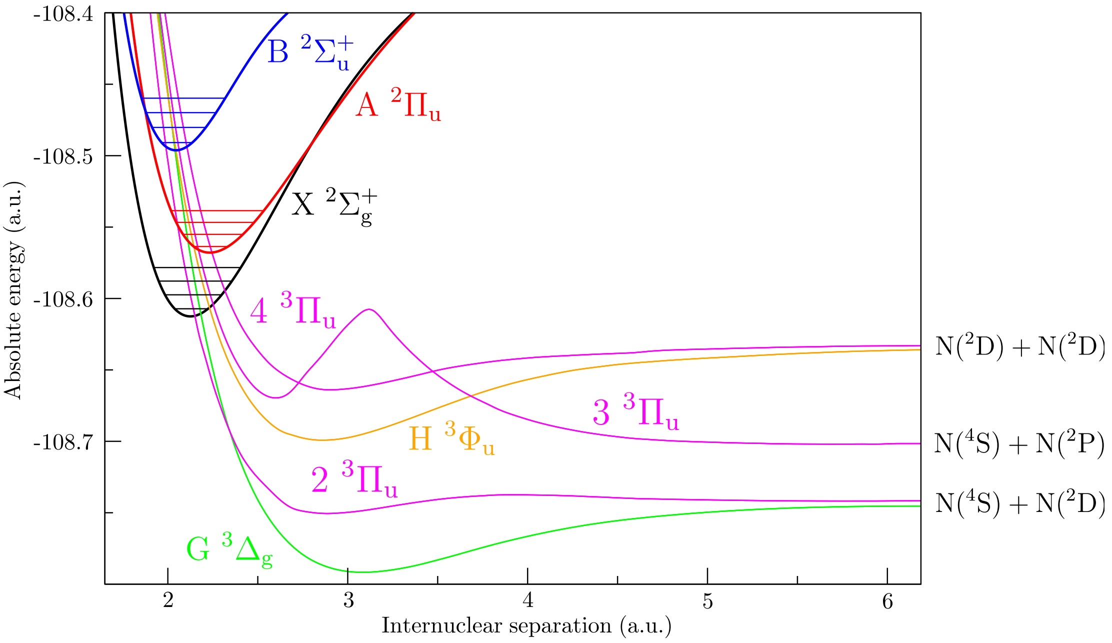

Figure 6.4: Triplet dissociative states included in the cross-section calculation with their asymptotic limits. The potential energy curves were taken from the data provided in I and II.

figure 6.7 for singlet and triplet states respectively.

Rydberg-Rydberg couplings

Rydberg-Rydberg couplings were found for the interaction between the Rydberg series with the lowest value of ℓ converging on the X state and the Rydberg state with the lowest value of n and ℓ converging on the A state. Rydberg-Rydberg couplings for the B state interacting with the X state were not included in the calculation as the only interaction was at very short internuclear separations. The implementation of MQDT used only supports Rydberg-Rydberg couplings between the ground and excited states and hence couplings between the A and B state were not included in the calculation. The couplings were calculated by assuming a two state interaction with adiabatic potential energy matrix $\mathbf{V}$ between the two adiabatic Rydberg state potentials with matrix elements $V(R)_{ij} = V(R)\delta_{ij}$. This can be transformed to a diabatic potential matrix $\mathbf{U}$ with a 2×2 rotation matrix $\mathbf{R}$ using $\mathbf{U} = \mathbf{R}^{-1}\mathbf{V}\mathbf{R}$. The off-diagonal elements of the diabatic potential matrix $U_{12} = U_{21} = \frac{1}{2}(V(R)_{22} - V(R)_{11})\sin(2\gamma(R))$ then gives the unscaled electronic coupling between the two states where γ is the rotation angle. If the energetic point of closest approach occurs at the same R then $\gamma = \pi/4$ and the coupling is simply half the difference between the adiabatic states (Roos et al., 2009). The coupling is then scaled according to the scaling law

$$\tilde{U}_{n_i n_j} = \sqrt{n_i^{*3} n_j^{*3}}\, U_{n_i n_j} \tag{6.34}$$

(in atomic units) where i and j correspond to each core state, and n^* is the effective quantum number associated with each Rydberg state (Carata et al., 2000).

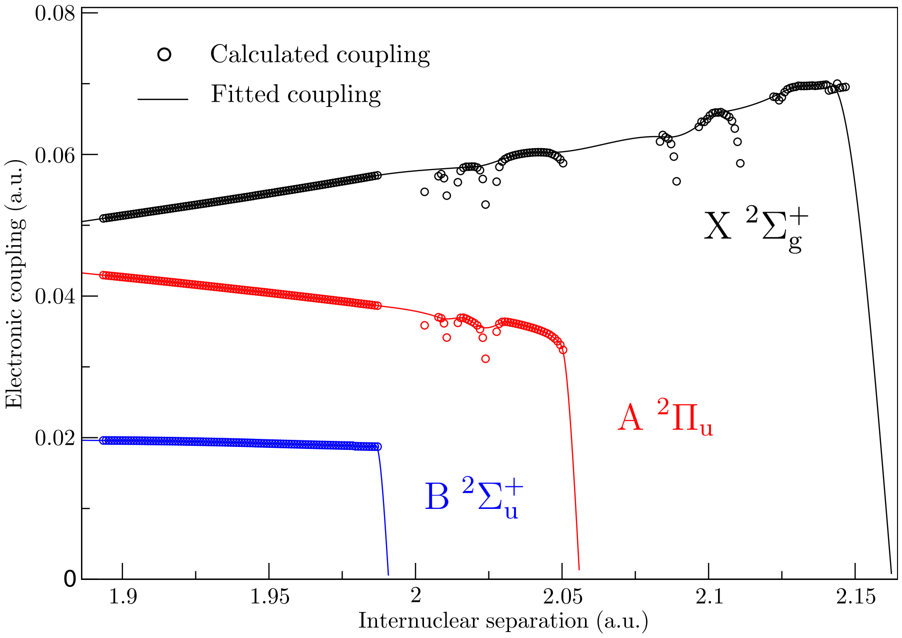

Figure 6.5: Example of the fitted couplings, in this case of $^3\Pi_u$ symmetry. The couplings show considerable structure due to the adiabatic nature of the states they are associated with. This structure was ignored and the gaps interpolated across using smoothing splines. The structure of the couplings is discussed in more detail in II.

In the data presented here, the point of closest approach only occurs at the same value of R for Rydberg states of low n. For interactions between Rydberg states of higher n (≥ 5), the coupling was approximated by taking half the difference between the adiabatic potentials at the value of R halfway between the point of closest approach. The couplings were assumed to go to zero at a point where the X Rydberg series and A Rydberg state were clearly no longer interacting, usually $\sim 0.2\ a_0$ away from the energetically lowest avoided crossing. The Rydberg-Rydberg couplings used in the calculation are plotted in figure 6.8.

6.3.3 Quantum defects

In an MQDT calculation the quantum defect is transformed in to the scattering phase shift and therefore, ideally, quantum defects associated with the highest value of n should be used. Computing quantum defects of high n can be problematic for standard configuration interaction (CI) techniques as they decrease in accuracy with increasing energy. As a result averages are taken of the quantum defect over the entire series (Carata et al., 2000).

The R-matrix method has a distinct advantage in that the highest n Rydberg states are the most accurate, as shown in table 4.2 of I. Therefore, for this calculation the quantum defect for the highest value of n was used. Limitations were placed on this value by the energetic proximity of the A state to the X state which results in Rydberg states interacting close the threshold. This, coupled with the energy difference between states scaling with $1/n^3$, makes it difficult to confidently identify high n Rydberg states over a large enough range of internuclear separations, $\sim 1.5 - 3.5$

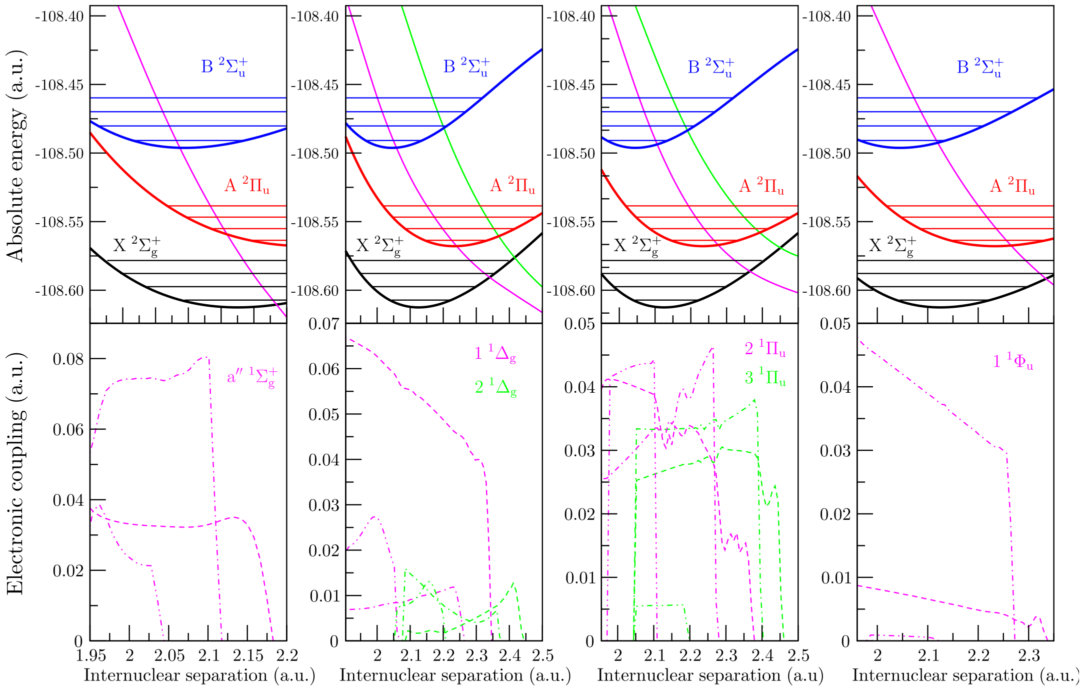

Figure 6.6: Potential energy curves of singlet states (top panel) and their respective Rydberg-valence coupling (lower panel). The couplings are resolved by the ionic state to which they are coupled; X state – – –, A state – · –, B state – · · –.

a.u.. Nevertheless, for all symmetries, quantum defects with $n \geq 7$ were successfully used.

6.4 Computational details

The potential energy curves included in the calculation were selected based on their crossing point with the ground state PEC of the ion and the size of their Rydberg-valence coupling. The R-matrix calculation yielded many more states than those that are included in the calculation, however, most were deemed to make insignificant contributions to the total cross-section for the energy range studied. There is also some ambiguity as to whether previously unidentified states are valence states or Rydberg states converging on the a $^4\Sigma_u^+$ state of the ion.

Eleven dissociative states of singlet and triplet symmetry were included in the calculation, see figure 6.3 and figure 6.4, with couplings resolved to each state of the ion, see figure 6.6 and figure 6.7. Cross-sections were calculated for $v_i^+ = 0 - 3$ with an energy range 10^{-5} - 1 eV. Ionisation channels associated with the X, A and B states were included in the calculation. Only the X and A ionisation channels were coupled as the X-B Rydberg-Rydberg coupling is only important at very short bond lengths and was deemed negligible. The cross-section calculation was performed for each symmetry of the neutral individually and then summed to find the total cross-section. The integration of eq. (6.17) was performed from 0.5 to 25.0 a_0.

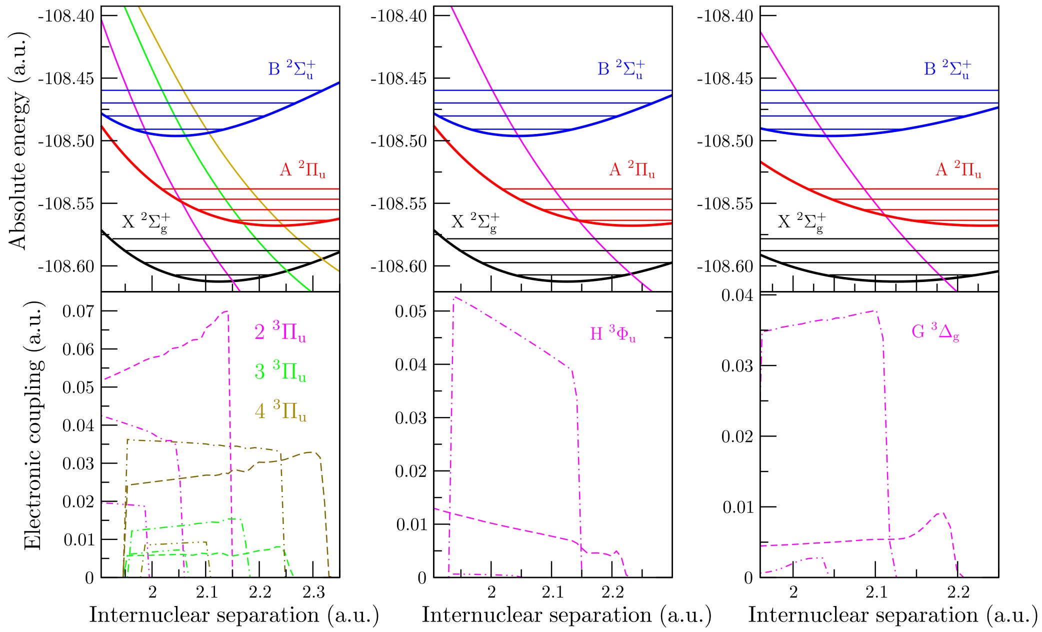

Figure 6.7: Potential energy curves of triplet states (top panel) and their respective Rydberg-valence coupling (lower panel). The couplings are resolved by the ionic state to which they are coupled; X state – – –, A state – · –, B state – · · –.

6.5 Results and discussion

6.5.1 Cross-sections

The DR cross-section of N_2^+ in its electronic ground state, X, in initial vibrational levels $v_i^+ = 0 - 3$ can be seen in figure 6.9 and, at a larger scale for $v_i^+ = 0$ in figure 6.10. What is immediately obvious from figure 6.10 is that the cross-section is dominated by the $^3\Pi_u$ symmetry, in particular the 2 $^3\Pi_u$ state. This is unsurprising considering the state's position close to the turning point of the ion ground state, its large coupling, see figure 6.11, and previous studies by Guberman (Guberman, 2003, 2007, 2012, 2013) and Kella et al. (1996).

Secondly, the $N_2^+(v_i^+ = 1)$ DR rate is significantly lower than that for $v_i^+ = 0, 2, 3$. If one considers that the dominant state in the cross-section is the 2 $^3\Pi_u$ state, then this is also to be expected. The crossing point of this state is very close to the turning point of the ion ground state, therefore, for $v_i^+ = 1$, the overlap of the wavefunction of this state and the vibrational wavefunction will be significantly reduced due to the node in the vibrational wavefunction. This effect is illustrated in figure 6.11. For $v_i^+ = 0$, the contribution to the total cross-section from the 3 and 4 $^3\Pi_u$ states is almost negligible in comparison to 2 $^3\Pi_u$. For $v_i^+ = 1$, the 2 and 4 $^3\Pi_u$ states have a similar level of contribution to the overall cross-section. This is in agreement with previous studies by Guberman that the most important dissociative states for DR are the 2 and 4 $^3\Pi_u$. For $v_i^+ = 2, 3$ the overlap with the dissociative state wavefunction increases and the magnitude of the cross-section is similar to that of $v_i^+ = 0$.

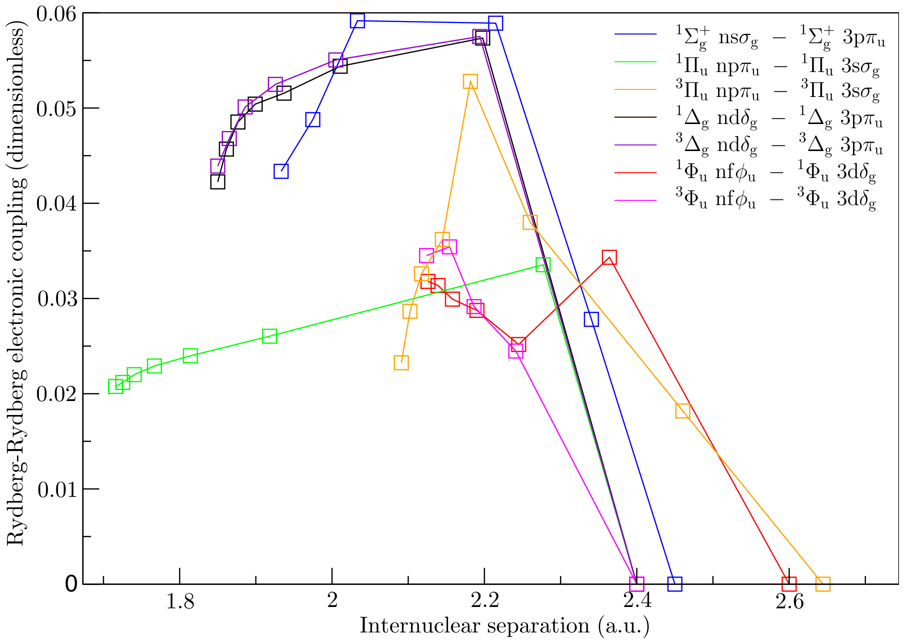

Figure 6.8: Rydberg-Rydberg couplings for each symmetry included in the cross-section calculation. The couplings associated with Rydberg states with $n \geq 5$ are only approximate, see text.

States of other symmetry which cross within $v_i^+ = 0$ are a$''$ $^1\Sigma_g^+$ and G $^3\Delta_g$; figure 6.6 and figure 6.7 show that although the total width of these states is large, consideration of the autoionisation branching ratios shows that the majority of the coupling is to the A state rather than X state, resulting in a reduced DR cross-section.

All other states included in the calculation either have a small coupling to the X state, cross the ground state far from the turning point, or both and as a result make only minor relative contributions to the cross-section. The $^1\Pi_u$ channel does not open until 0.397 eV. Therefore, in a high resolution measurement of the DR cross-section it is expected that the majority of the structure will be due to the 2 $^3\Pi_u$ with only narrow resonance peaks due to states of other symmetry.

The effect of including additional cores on the cross-section can be seen in figure 6.12 and figure 6.13 for $v_i^+ = 0$ for $^3\Pi_u$ and $^3\Delta_g$ respectively. For $^3\Pi_u$ the cross-section does not change significantly with the addition of each core to the calculation, except for slight shifts in the resonance structure, the most significant change occurring with the inclusion of the third core. This is to be expected as the majority of the coupling for the dominant dissociative state 2 $^3\Pi_u$ is to the X state, see the left most panel of figure 6.7. The addition of the second core has a much larger impact on the $^3\Delta_g$ cross-section, this is because the G $^3\Delta_g$ state is most strongly coupled to the A state as shown in the rightmost panel of figure 6.7. As $^3\Pi_u$ is the dominant symmetry, the core-excited effects are only present in the minor dissociative channels, such as G $^3\Delta_g$, and are therefore not prevalent in the global cross-section.

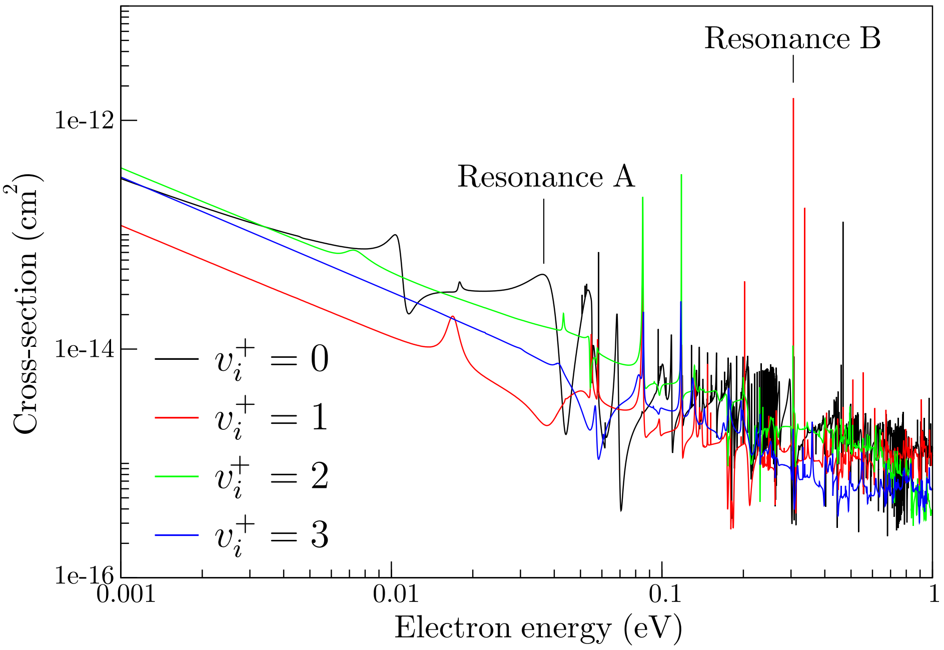

Figure 6.9: Computed N_2^+ dissociative recombination cross-section as a function of cation vibrational state, v_i^+.

6.5.2 Rate-coefficients

Isotropic rate-coefficients were obtained by convoluting the DR cross-section with the Maxwellian isotropic distribution function for velocities of free electrons (Florescu et al., 2003),

$$\alpha(T) = \frac{8\pi}{(2\pi kT)^{3/2}} \int_0^\infty \sigma(\epsilon) e^{-\epsilon/kT} d\epsilon, \tag{6.35}$$

where $\sigma(\epsilon)$ is the cross-section. The resulting rates $\alpha(T)$ were fitted with the form $A(T_e/T)^{-a}$ and are given in Table. (6.1), the fits give a good reflection of the temperature dependence within their respective ranges. However, this fitting form is not particularly suitable for the $v_i^+ = 1$ DR rate as its temperature dependence changes frequently. Therefore fits were made over shorter energy ranges to compensate.

6.5.3 Comparison with other work and discussion of vibrational dependence

Cross-sections

As discussed in chapter 1, section 1.2.3, there have been a number of difficulties cooling N_2^+ sufficiently so that a measurement can be made of it's vibrational ground state. Therefore to make a correct comparison with experiment, the relative proportions of the cross-section must first be summed according to the vibrational distribution of the ions with energy. Only two experimental studies provide vibrational distributions of the ion beam and cross-sections, Peterson et al. (1998)

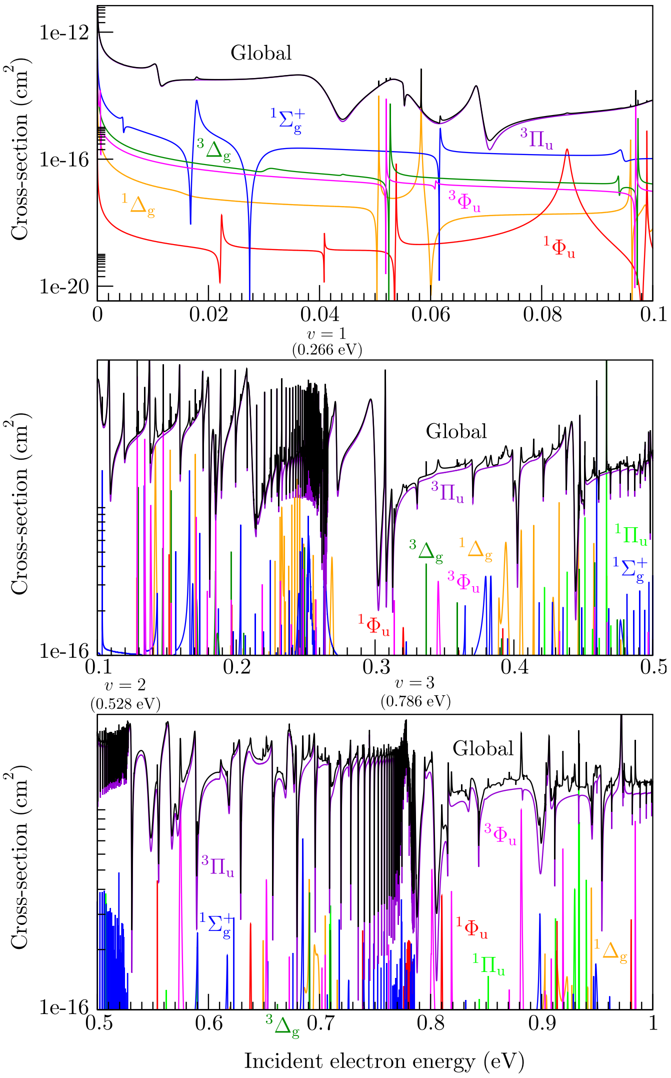

Figure 6.10: Contribution of different dissociative curves of N_2^{**} to the $N_2^+(v_i^+ = 0)$ DR cross-section as a function of energy.

and Sheehan and St.-Maurice (2004).

The vibrational distribution provided by Sheehan and St. Maurice was not directly measured in their merged beam experiment; instead it was taken from a calculation of the Franck-Condon distribution following electron impact ionisation (Schmidt et al., 1996) by Noren et al. (1989). It was deemed that this distribution should give a "reasonable reflection" of the vibrational population of their ion beam. Peterson *et al* did not perform a direct measurement of their vibrational populations either; instead they measured the DR rate times population at zero relative energy of the electron and ion beam. By convoluting the calculated cross-section according to the temperature distribution of the ion beam (transversal 0.01 eV and longitudinal 0.0001 eV) using an anisotropic Maxwell electron velocity distribution (Guberman, 2013) vibrationally resolved rates can be calculated to find a derived population. The derived population using the rates at 10^{-5} eV is 0.274:0.533:0.066:0.127 for $v_i^+ = 0 - 3$ respectively for the JIMIS ion source (Peterson et al., 1998). The vibrational distribution provided by Sheehan and St. Maurice is a

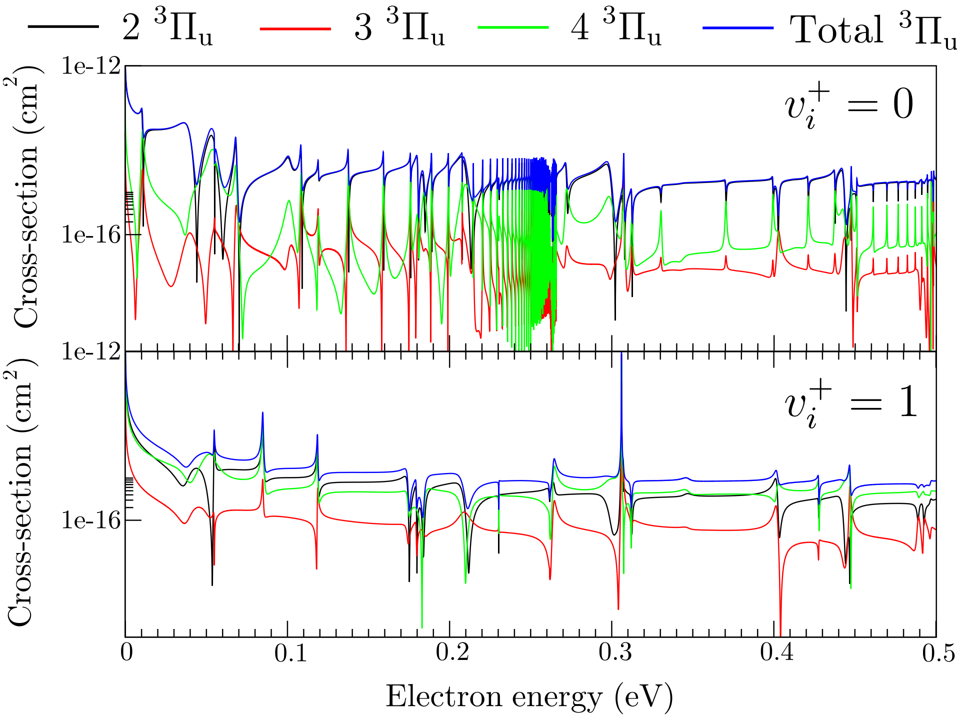

Figure 6.11: Contribution to the DR cross-section of N_2^+ for $v_i^+ = 0$ (top) and $v_i^+ = 1$ (bottom) from N_2^{**} states of $^3\Pi_u$ symmetry.

0.651:0.211:0.084:0.035:0.013:0.005:0.001 for $v_i^+ = 0 - 6$ respectively.

Figure 6.14 gives a comparison of the effective cross-sections measured in both experiments with the calculated convoluted cross-sections scaled with their respective vibrational populations. The general agreement with experiment is good; in practice use of the vibrational distribution given by Sheehan and St. Maurice gives better agreement with both measurements than the derived population distribution from Peterson *et al.*

There are two main structures in the CRYRING cross-section which are reproduced by the calculation: a broad resonance centred at ~ 0.07 eV and a smaller resonance structure at ~ 0.3

Table 6.1: Fitted DR rate-coefficients for N_2^+ as function of vibrational state, v_i^+.

v_i^+	Rate-coefficient (cm^3 s^{-1})	Temperature range (K)
0	$2.568 \times 10^{-7}(T_e/300)^{-0.5166}$	$300 \leq T_e \leq 800$
	$1.492 \times 10^{-7}(T_e/800)^{-0.47}$	$800 \leq T_e \leq 1500$
1	$6.378 \times 10^{-8}(T_e/300)^{-0.239}$	$300 \leq T_e \leq 500$
	$5.652 \times 10^{-8}(T_e/500)^{-0.17}$	$500 \leq T_e \leq 800$
	$5.225 \times 10^{-8}(T_e/800)^{-0.075}$	$800 \leq T_e \leq 1025$
	$5.117 \times 10^{-8}(T_e/1100)^{-0.023}$	$1025 \leq T_e \leq 1250$
	$5.104 \times 10^{-8}(T_e/1300)^{0.008}$	$1250 \leq T_e \leq 1500$
2	$2.145 \times 10^{-7}(T_e/300)^{-0.36}$	$300 \leq T_e \leq 800$
	$1.499 \times 10^{-7}(T_e/800)^{-0.42}$	$800 \leq T_e \leq 1500$
3	$1.228 \times 10^{-7}(T_e/300)^{-0.50}$	$300 \leq T_e \leq 600$
	$8.711 \times 10^{-7}(T_e/600)^{-0.4352}$	$600 \leq T_e \leq 1500$

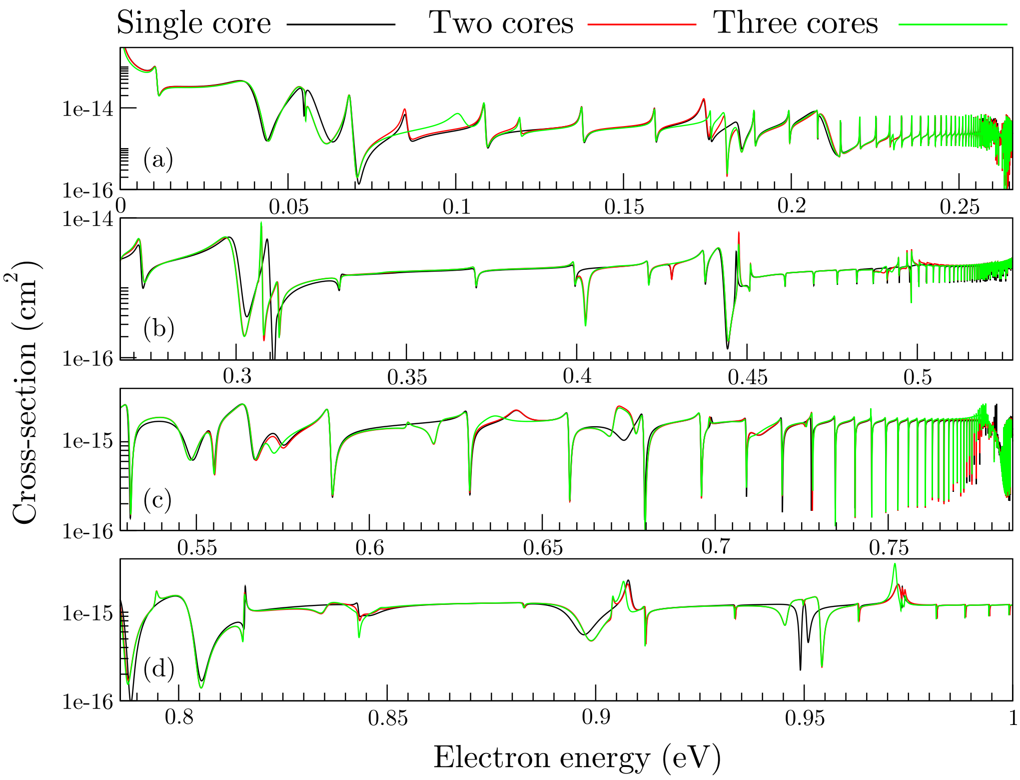

Figure 6.12: Effect of including multiple cores in the cross-section calculation for $^3\Pi_u$ symmetry. Each panel, with exception of the final, ends at a vibrational threshold. That is, (a) 10^{-5} eV - $v_i^+ = 1$ (0.266 eV), (b) $v_i^+ = 1$ (0.266 eV) - $v_i^+ = 2$ (0.528 eV), (c) $v_i^+ = 3$ (0.528 eV) - $v_i^+ = 4$ (0.786 eV), (d) $v_i^+ = 4$ (0.786 eV) - 1 eV. Including the second and third core only has a minor effect on the cross-section as, for the dominant dissociative state $2^3\Pi_u$, the majority of the Rydberg-valence coupling is to the ground state, see the leftmost panel of figure 6.7.

eV. These structures are present in the cross-section with both population distributions, and are labelled 'resonance A' and 'resonance B' in figure 6.14. The results presented here indicate that each structure comes from a cross-section of a different vibrational level; resonance A is from the $v_i^+ = 0$ cross-section and resonance B from the $v_i^+ = 1$ cross-section, figure 6.9. This gives a clear theoretical indication that the vibrational distribution is dominated by $v_i^+ = 0$ and $v_i^+ = 1$; the results do not show any large resonance features in $v_i^+ = 2, 3$.

Sheehan and St. Maurice make the point that as their measured cross-sections and the CRYRING cross-section are similar, that the vibrational distribution of the ions may have also been similar in both experiments. This is, of course, only true if the cross-section is significantly vibrationally dependent. This calculation suggests that there is clearly a significant difference between $v_i^+ = 0$ and 1 cross-sections, and that the calculated cross-section with the Sheehan and St. Maurice population distribution has better agreement with the CRYRING cross-section. One, however, must be cautious in making these comparisons as the measurement of the population distribution was not actually carried out on the ion beam of either experiment and population effects are know to have subtle effects on the effective DR cross-sections measured, as found, for example, in the DR of H_3^+ (Kreckel et al., 2012).

Guberman's most recent study (Guberman, 2013) suggests that at very low energies (0.001 eV)

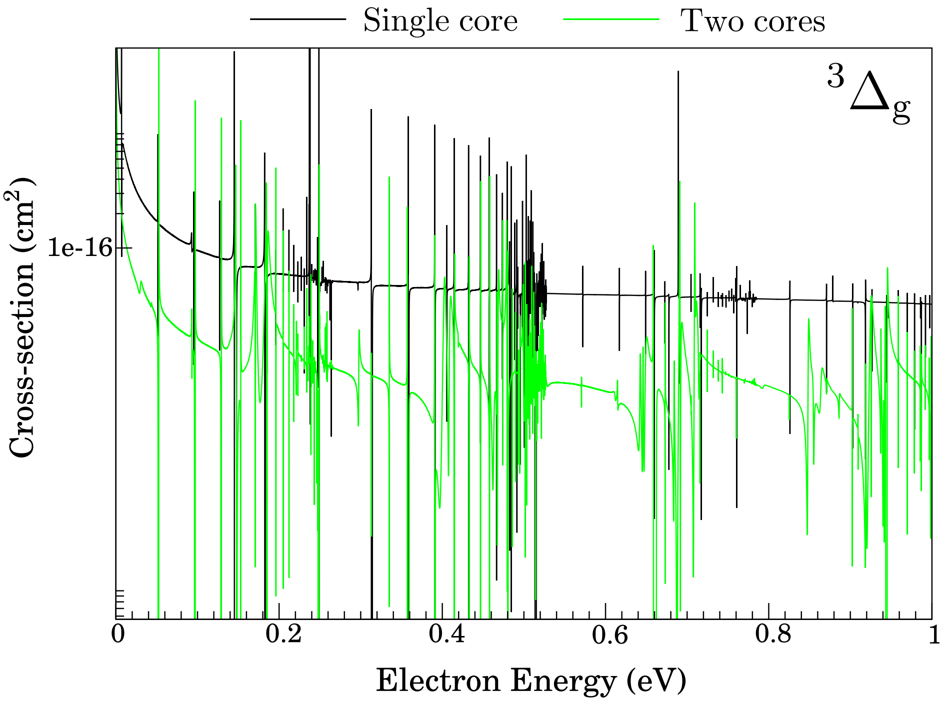

Figure 6.13: Effect of including multiple cores in the cross-section calculation for $^3\Delta_g$ symmetry. It can be seen in the rightmost panel of figure 6.7 that for this symmetry the majority of Rydberg-valence coupling is to the A state. As a result, the inclusion of the second core has a significant impact on the cross-section. The inclusion of the third core makes very little difference to the cross-section and resultantly is not shown.

the cross-sections for each vibrational level are all of a similar magnitude, and in fact that $v_i^+ = 1$ is the largest. Use of these cross-sections yields a vibrational distribution of 0.50:0.25:0.10:0.14 for $v_i^+ = 0-3$ respectively, which is similar to that of Sheehan and St. Maurice. From the perspective of this model, the difference between the two studies comes down to the importance of the 4 $^3\Pi_u$ state. In Guberman's model this state is slightly lower in energy and has a Rydberg-valence coupling which is around double the magnitude found by the R-matrix calculations presented in II, dominating the $v_i^+ = 1$ cross-section at low energies. In this model the process is driven entirely by the 2 $^3\Pi_u$ which, for reasons described in section 6.5.1, leads to a reduced $v_i^+ = 1$ cross-section. Unfortunately the data for the cross-sections is not available for Guberman's 2013 study so direct comparisons of the vibrationally resolved cross-sections cannot be made.

Rate-coefficients

Figure 6.15 compares the flowing afterglow Langmuir probe (FALP) (Larsson and Orel, 2008) measurements, given as an isotropic rate-coefficient, of Mahdavi et al. (1971), Geoghegan et al. (1991) and Canosa et al. (1991) and the calculated $v_i^+ = 0$ isotropic rate-coefficient at 300 K by Sheehan and St.-Maurice (2004). There is very good agreement with the calculated $v_i^+ = 0$ rates and the FALP measurements, the value is within error of the measurement of Canosa et al. (1991), and Mahdavi and is just outside the error bars of Geoghegan et al. (1991).

By comparing the above measurements for $v_i^+ = 0$ and those with a mix of vibrational levels

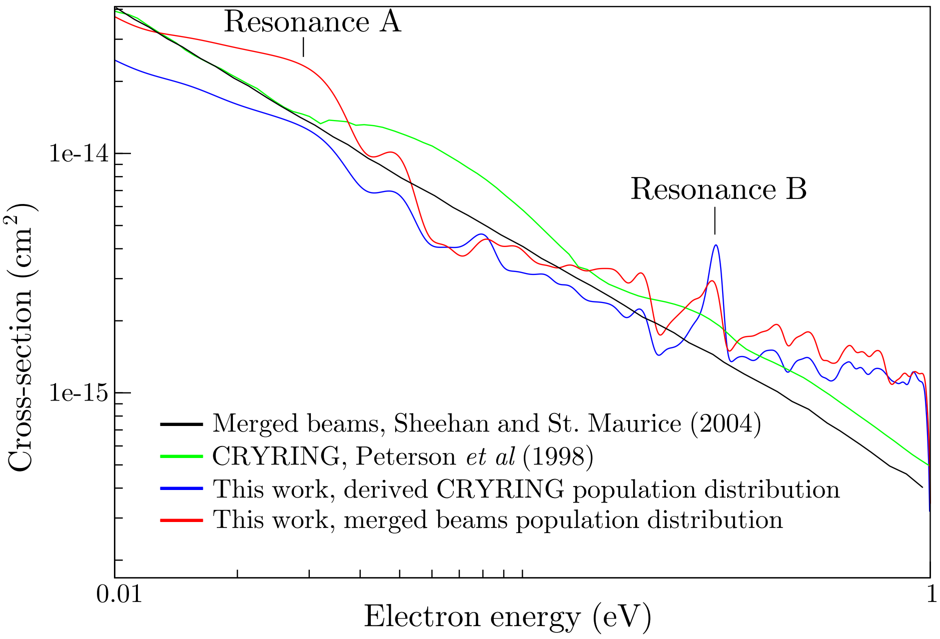

Figure 6.14: Comparison of the computed N_2^+ DR effective cross-sections with those measured using CRYRING by Peterson et al. (1998) and the merged beams measurement of Sheehan and St.-Maurice (2004).

there is another indication that the $v_i^+ = 1$ rate must be lower than $v_i^+ = 0$; the rates where the ions are not vibrationally cool (Peterson *et al* and Sheehan and St. Maurice) are both lower than the FALP measurements of $v_i^+ = 0$.

To compare the computed rate-coefficient with the measurements of Peterson *et al* and Sheehan and St. Maurice the rate-coefficients using the cross-sections they provided have been found. Although rates of the form $A(T_e/T)^{-a}$ are provided in both studies, fittings of this form ignore a lot of structure due to the simple single-exponent temperature dependence. Sheehan and St. Maurice also recalculated an isotropic rate-coefficient using the cross-section of Peterson *et al* and found a fitted value of $(1.50{\pm}0.23){\times}10^{-7}(T_e/300)^{-0.39}$ cm^3 s^{-1} which has nearly perfect agreement with the value found for their merged beams experiment, $(1.50{\pm}0.23){\times}10^{-7}(T_e/300)^{-0.38}$ cm^3 s^{-1}. The value found at 300 K in this study is 1.734×10^{-7}cm^3 s^{-1} which is similar to the original value given by Peterson *et al*, $(1.75 \pm 0.09) \times 10^{-7}$cm^3 s^{-1}.

Figure 6.16 gives a comparison of this work scaled by the derived CRYRING and Sheehan and St. Maurice distributions with the rate-coefficients calculated using their respective cross-sections. Again it is seen that the Sheehan and St. Maurice vibrational distribution gives better agreement with the CRYRING results indicating that this may be closer to the true distribution. All of the rates have a very similar temperature dependence above 600 K, the vibrationally resolved rate-coefficients in figure 6.17 also indicate that there is not a drastic change in temperature dependence with vibrational excitation. The divergence between the Sheehan and St. Maurice distribution and the CRYRING rate is due to resonance A (see figure 6.14) being slightly too low in energy and narrower than that measured in the CRYRING cross-section

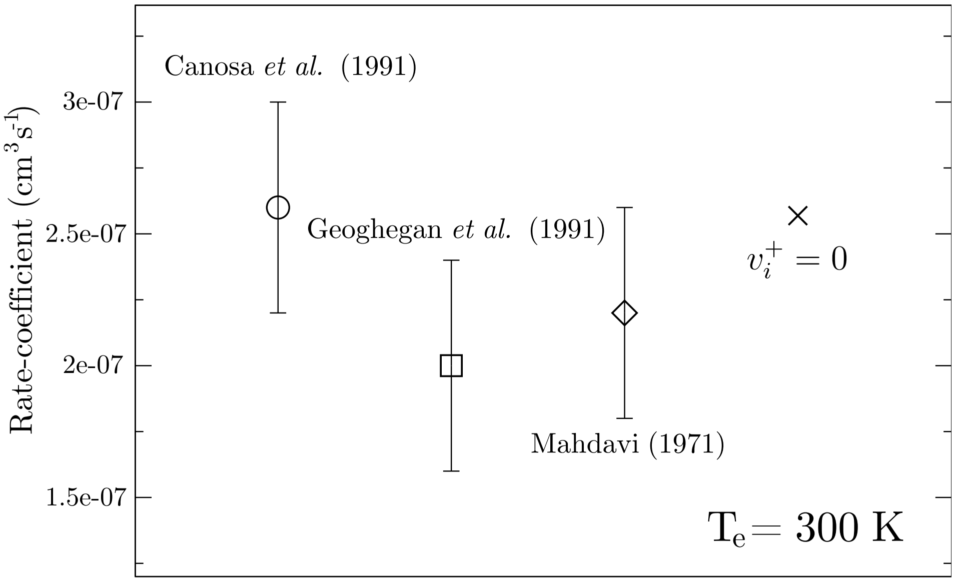

Figure 6.15: Comparison of the calculated, isotropic rate-coefficient for N_2^+ DR of this work for $v_i^+ = 0$ with the FALP measurements of Mahdavi et al. (1971), Geoghegan et al. (1991) and Canosa et al. (1991) at 300 K. Agreement with experiment is good.

Comparisons with available calculated rates from Guberman are presented in figure 6.17. The formula given by Guberman is $2.2^{+0.2}_{-0.4} \times 10^{-7}(T_e/300)^{-0.40}$ cm^3 s^{-1}. When comparing unfitted and fitted, it is clear that fitting over a large temperature range (100–3000 K) averages out a lot of the structure. There is, however, good agreement between this and the $v_i^+ = 0$ rate of this study fitted and unfitted. The rates for $v_i^+ = 1, 2$ are very different in terms of both magnitude and temperature dependence.

Summary of vibrational distribution discussion

Overall the agreement between both experiments and experiment and theory is good. The agreement between the calculated rate and Guberman's for $v_i^+ = 0$ is also good. It is, however, difficult to make a solid conclusion as to the actual vibrational population of each experiment. More weight should be placed on the vibrational distribution of Peterson *et al* as this measurement took place on the ion beam used in the cross-section measurement. However, this measurement was taken at 0 eV relative collision energy and it is not guaranteed that the vibrational distribution will not change during the experiment. The fact that the $v_i^+ = 1$ DR cross-section is much lower relative to the other vibrational level results in this vibrational state dominating the population. The better agreement with the vibrational distribution of Sheehan and St. Maurice indicates that this maybe be closer to the vibrational distribution in the CRYRING experiment.

6.5.4 Branching ratios

Branching ratios are calculated by simply summing the cross-sections for each individual dissociative channel to each asymptote and dividing by the total cross-section. A Landau-Zener calculation

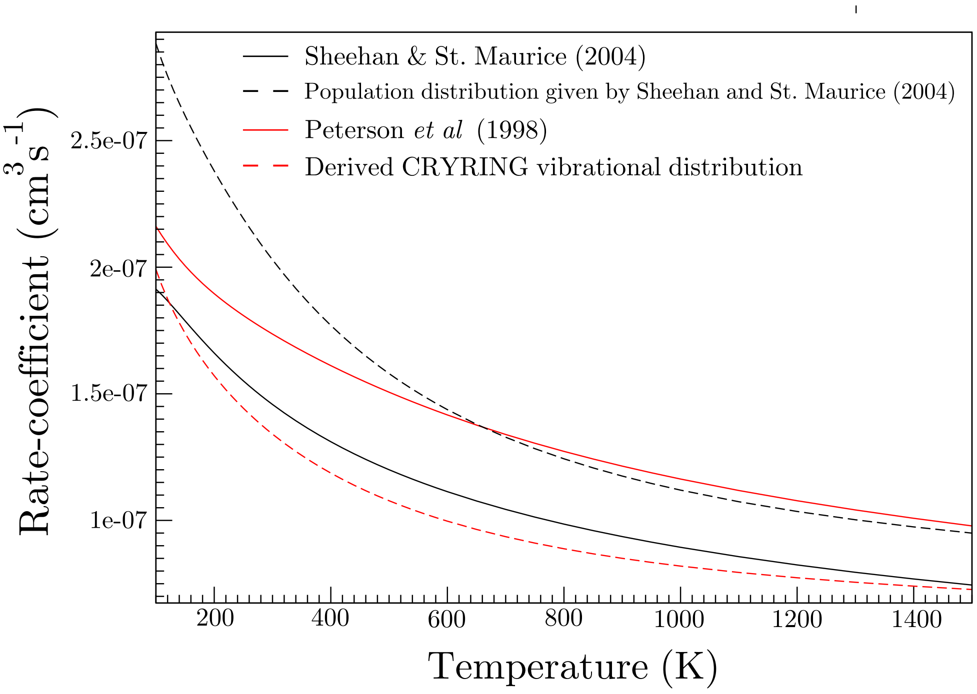

Figure 6.16: Comparison of the calculated, isotropic rate-coefficients for N_2^+ DR with the measurements of Peterson et al. (1998), and Sheehan and St.-Maurice (2004). The experimental rate-coefficients were recalculated using the cross-sections from each respective study.

(Marx and Hutter, 2009) was performed on the avoided crossing highlighted by the red box in figure 6.5, the crossing probability to the lower state was found to be 0.85 for $v_i^+ = 0$ and 0.87 for $v_i^+ = 1$. Therefore 15% and 13% of the branching ratio going to $\mathrm{N}(^4\mathrm{S}) + \mathrm{N}(^2\mathrm{D})$ was subtracted and added to the branching ratio for $\mathrm{N}(^2\mathrm{D}) + \mathrm{N}(^2\mathrm{D})$ for $v_i^+ = 0$ and $v_i^+ = 1$ respectively. The branching ratios for $v_i^+ = 0, 1$ are displayed in figure 6.18 for 10^{-5}–0.1 eV.

The branching ratios of the DR of N_2^+ were measured by Peterson et al. (1998) for $v_i^+ = 0$ and it's isotopologue $^{15}\mathrm{N}^{14}\mathrm{N}^+$ by Kella et al. (1996) for $v_i^+ = 0, 1$ at zero relative energy. The use of $^{15}\mathrm{N}^{14}\mathrm{N}^+$ by Kella *et al* meant that radiative rovibrational relaxation was possible due to the dipole of the molecule and the branching ratios for $v_i^+ = 0$ could be measured. Given the small difference between the ground vibrational state of $^{14}\mathrm{N}_2^+$ and $^{15}\mathrm{N}^{14}\mathrm{N}^+$, a comparison between the measured rate of the isotoplogue and the calculated rate of the homonuclear $^{14}\mathrm{N}_2^+$ is justified. Table. (6.2) gives the branching ratio at 10^{-5} eV with a comparison with experimental data.

For $v_i^+ = 0$ the agreement is reasonable if it is considered that both experimental studies report that the majority of the cross-section should go to $\mathrm{N}(^4\mathrm{S}) + \mathrm{N}(^2\mathrm{D})$ and $\mathrm{N}(^2\mathrm{D}) + \mathrm{N}(^2\mathrm{P})$. In this model there is no path to the $\mathrm{N}(^2\mathrm{D})+\mathrm{N}(^2\mathrm{P})$ asymptote available at this energy which is confirmed by experiment. There is, however, a disparity between the experiment and the relative branching to these two products. The reasons for this are unclear; both this theoretical study and that of Guberman (2012) suggest that the 2 $^3\Pi_\mathrm{u}$ is the dominant state for $v_i^+ = 0$ which dissociates to $\mathrm{N}(^4\mathrm{S}) + \mathrm{N}(^2\mathrm{D})$. In Guberman's first study of the DR of N_2^+ (Guberman, 1991) he also calculates the crossing probability of the avoided crossing highlighted in figure 6.2 and finds a similar crossing

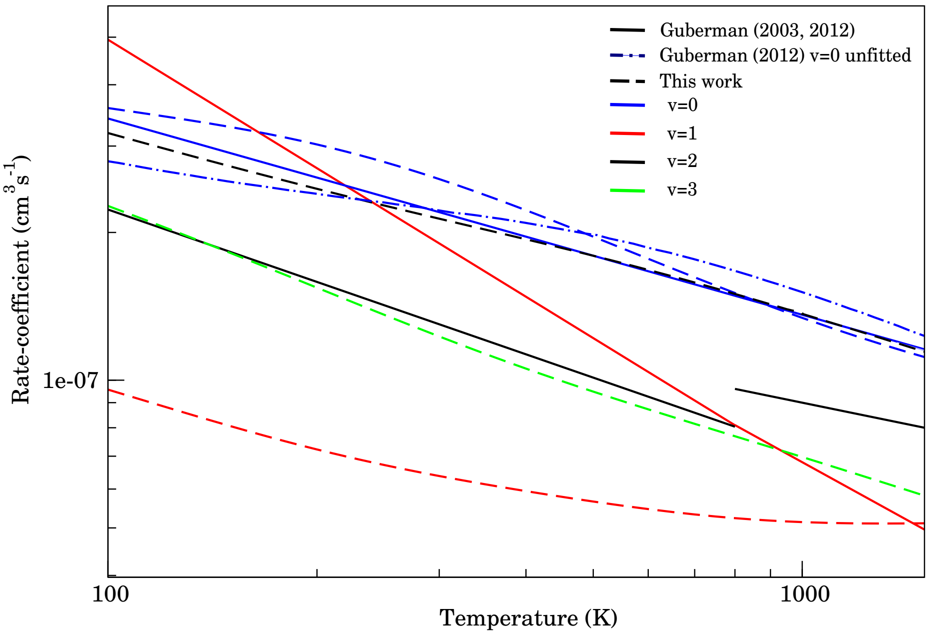

Figure 6.17: Comparison with Guberman's (Guberman, 2003, 2012) isotropic N_2^+ DR rate-coefficients. Guberman's fitted and unfitted values for $v_i^+ = 0$ are displayed for comparison.

Table 6.2: Branching ratios, calculated and experimentally measured for $v_i^+ = 0, 1$.

	Product channel	Branching ratio		
$v_i^+ = 0$		This work	Kella *et al*	Peterson *et al*
	$N(^4S) + N(^2D)$	0.776	0.46 ± 0.08	0.37 ± 0.08
	$N(^4S) + N(^2P)$	0.005	0.08 ± 0.06	0.11 ± 0.06
	$N(^2D) + N(^2D)$	0.219	0.46 ± 0.08	0.52 ± 0.04
	$N(^2D) + N(^2P)$	0.0	0.0	
$v_i^+ = 1$		This work	Kella *et al*	
	$N(^4S) + N(^2D)$	0.434	–	
	$N(^4S) + N(^2P)$	0.047	–	
	$N(^2D) + N(^2D)$	0.519	0.5 ± 0.1	
	$N(^2D) + N(^2P)$	0.0	0.5 ± 0.1	

probability of 0.88, this again is not enough to account for the difference between the theory and experiment. Kella *et al* report that Guberman has recalculated branching ratios to be 0.70, 0.27, and 0.03 for $N(^4S) + N(^2D)$, $N(^2D) + N(^2D)$ and $N(^4S) + N(^2P)$ respectively. This calculation has not been reported in detail, but gives good agreement with the results presented here.

Due to the resolution of their experimental equipment Kella *et al* were only able to measured the branching ratios for the $N(^2D) + N(^2D)$ and $N(^2D) + N(^2P)$ asymptotes which they found to be equal. In this model only 1% of the cross-section is going to the $N(^2D) + N(^2P)$ asymptote and just under half to $N(^2D) + N(^2D)$. The branching ratios for $v_i^+ = 1$ are very similar to the measured values for $v_i^+ = 0$.

Figure 6.2 shows the many avoided crossings in the super-excited states of N_2, some strongly avoided. It may be that accounting for these avoided crossings in a more rigorous way is key to reproducing the experimental results. A time-dependent wave packet calculation (Orel, 2005)

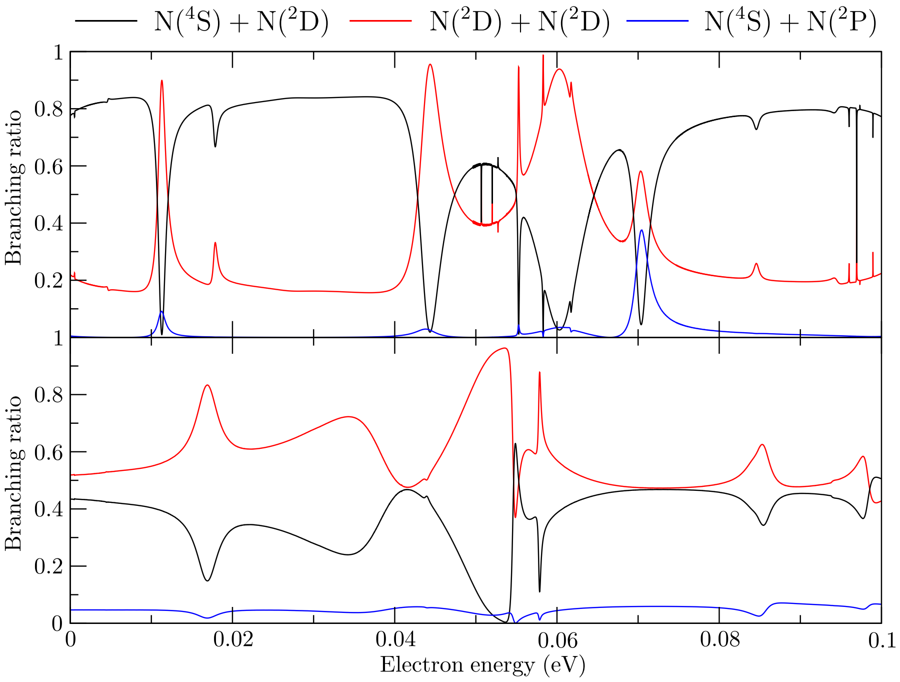

Figure 6.18: Energy-dependent branching ratios for $v_i^+ = 0$ (upper panel) and $v_i^+ = 1$ (lower panel).

would provide more information about the final state products.

6.6 Conclusion

The calculated cross-section has good agreement with experiment and also reproduces the two main structures in the CRYRING (Peterson et al., 1998) cross-section. The cross-section is completely *ab initio*, no empirical data has been introduced into the calculation at any point. This shows that the R-matrix method coupled with MQDT approach presented in this chapter provides a self-consistent and accurate *ab initio* approach to calculating DR cross-sections. As with previous theoretical studies by Guberman (Guberman, 1991, 2003, 2007, 2012, 2013) this study shows that the most important symmetry for the DR of N_2^+ is $^3\Pi_u$. The main difference between the model presented here and that of Guberman is the relative importance of the 2 $^3\Pi_u$ and 4 $^3\Pi_u$ states. It is interesting to note that, although the potential energy curve crossing positions were similar in both studies, the couplings were not. Nevertheless, both results, at least for $v_i^+ = 0$, resulted in good agreement with experiment. There is strong experimental evidence to suggest that the $v_i^+ = 1$ rate is lower than $v_i^+ = 0$ one, this study also suggests that this is the case. The vibrationally resolved rates that have been calculated indicate that there is not a strong vibrational dependence on temperature dependence, this is in agreement with previous studies (Peterson et al., 1998; Sheehan and St.-Maurice, 2004). Finally, it is noted that after the completion of this work another theoretical calculation of the DR cross-section of N_2^+ was published by Fifirig (2014).

Chapter 7

Conclusion

This thesis has shown that the R-matrix method has the capability to produce the data needed to compute accurate fully *ab initio* dissociative recombination cross-sections for diatomic molecules. A brief summary of the results by chapter is given below followed by conclusions for the individual parameters calculated. Finally a discussion of future work is given to conclude.

7.1 Summary of results

Chapter 4 showed that it was possible to obtain accurate *ab initio* potential energy curves for the bound region of an N_2 molecule using the R-matrix method. Potential energy curves were found for all singlet and triplet symmetries with $\ell \leq 4$. Although not competitive with multireference configuration interaction computations for low-lying valence states, it was shown that this method of computation was particularly appropriate for Rydberg states and Rydberg-valence states, see figure 4.7. The comparison of the equilibrium energies of the Rydberg states converging on the ground state of the ion was particularly favourable with a maximum percentage difference of 5.58% for $n \geq 3$ and a maximum percentage difference of 1.42 % for $n \geq 5$. Those converging on the first excited state of the ion had a disagreement of $\sim$ 12.5 %. The reasons for this disagreement were discussed in section 4.5.2. The agreement with experiment for valence states varied considerably, with generally a percentage difference of over 5 % and below 10 %, the use of these curves should be considered on a case by case basis. That is, for these states a number of sources of data already exist which were computed using different *ab initio* techniques (Spelsberg and Meyer, 2001; Michels, 2007; Ndome et al., 2008; Hochlaf, Ndome, Hammoutène and Vervloet, 2010; Hochlaf, Ndome and Hammoutène, 2010). Therefore each valence curve should be compared with the already available data to ensure that the curve with the best agreement with experiment is used in further studies.

The detailing of the interaction between the Rydberg and valence states is unprecedented and sets a benchmark for the calculation of Rydberg-valence states in diatomic molecules. The adiabats were matched using quantum defects, this method of matching is invaluable when dealing with energetically close-spaced states (such as Rydberg states) interacting in a complex manner. Many of the states characterised were previously unknown, particularly Rydberg states, see tables 4.2 to 4.8, and were characterised for the first time.

Chapter 5 showed that with the use of the improved fitting method implemented in TIMEDEL described in chapter 3, the time-delay method can provide a comprehensive description of the resonance structure and widths of a diatomic molecule. This chapter, like the previous, also shows the level of detail the R-matrix method is capable of producing with regards to Rydberg-valence interactions. In this case the problem is complicated by the fact that the resonances must be detected and then fitted, this problem is exacerbated in ions by the close energetic spacing and overlapping nature of the resonances. The inclusion of additional eigenvalues in the fitting process provides a robust method for characterising these overlapping resonances, see figure 3.1. When compared to fitting of the eigenphase sum using RESON it is clear that for ions, TIMEDEL should be the method of choice, see figures 5.1 and 5.2.

By combining the results from chapter 4 and chapter 5 it was possible to produce a complete description of the highly-excited electronic states of N_2 above and below the ionisation threshold, see figure 5.6.

Chapter 6 gave details of the actual dissociative recombination (DR) cross-section calculation using the data found in the previous two chapters and multichannel quantum defect theory (MQDT). This chapter showed the steps that needed to be taken to prepare the data from the R-matrix calculation to be used as inputs for the MQDT calculation. The calculated cross-section is completely *ab initio* and has excellent agreement with experiment; extensive comparisons were made in the chapter with a detailed discussion of the vibrational dependence of the cross-section. It was shown in this chapter that a DR cross-section can be calculated completely *ab initio* for a diatomic molecule by combining the R-matrix method with MQDT, whereas in previous studies empirical intervention was required (Schneider et al., 2000).

7.2 Potential energy curves

This is the first time a dense grid of internuclear separations has been used to compute potential energy curves using the R-matrix method, this has only become possible recently due to the parallelisation of the SCATCI module and the processing power of modern computers. Two important steps were taken to exploit these recent developments. During the development of the inner region model a significant amount of time and effort was invested in keeping the running time of the inner region calculation low meaning that many internuclear separations could be computed in a reasonable amount of time. The total run time of the target and inner region calculations in the final model was around 20 minutes per internuclear separation, meaning that calculating 2000 points per symmetry was feasible. Secondly, bash scripting was used to completely automate the process; computing 2000 points per symmetry and manually changing the inputs would have been laborious, impractical and subject to human error.

Integral to the correct representation of the Rydberg states was a good representation of the target, this was made possible by the use of multiconfiguration self consistent field (MCSCF) orbitals from MOLPRO and a large basis set (cc-pVQZ). Based on the success of the work presented here the use of MCSCF orbitals should become standard in all R-matrix calculations for diatomic molecules of a similar size to N_2.

The improved fitting method for TIMEDEL described in chapters 3 and 5 means that it is now possible to produce comprehensive potential energy curves using resonances from a R-matrix scattering calculation. Imperative to the success of this method was the fitting of multiple eigenvalues, this is integral for calculating resonances of ionic targets in lower symmetry groups than that of the molecule, in this case D_{2h} from $D_{\infty h}$. Resonances can be obscured by a resonance belonging to a different symmetry group in $D_{\infty h}$, but the same symmetry group in D_{2h}. The result of this is that these resonances can go completely undetected unless multiple eigenvalues of the time-delay matrix are used.

7.3 Electronic widths

This is the first time that electronic widths of resonances have been detected and fitted for a dense grid of internuclear separations. The use of this dense grid revealed a significant amount of structure due to the adiabatic states interacting with one another. The influence of this on processes such as DR remains untested.

The robust nature of the fitting process is best exemplified by the smooth ‘width-adiabats’ that can be generated using the fitted widths from TIMEDEL, see figure 5.7. In this figure it is possible to see the magnitude of the width smoothly transition from one dominant electronic configuration to another, showing the stability of the calculation and the fitting method.

The ability to easily compute branching ratios in the time-delay method made it convenient to resolve the widths by ionic state for the core-excited DR calculation. This facility coupled with TIMEDEL’s robust fitting method for overlapping resonances makes the time-delay method ideal for future calculations of resonances for DR cross-section calculations.

7.4 Quantum defects

As mentioned above, the agreement between the calculated Rydberg states and the experimental data was good, indicating the quantum defects of these states were also accurate; the use of high n quantum defects is imperative in a DR calculation as the quantum defect is transformed to the phaseshift in the electron-ion continuum. The use of BOUND for ground state quantum defects and TIMEDEL for the excited state quantum defects should be the preferred option for future calculations. Again, the use of a dense grid meant that the quantum defect could be found for many internuclear separations and comprehensive Edlén plots could be constructed revealing the adiabatic structure the quantum defects. The Edlén plots also served as an invaluable tool for matching the adiabats by quantum defect.

7.5 Future work

The aim of this thesis, as stated in chapter 1 was the following: 'to calculate the input parameters needed to calculate a DR cross-section of N_2^+ for temperatures relevant to space vehicle re-entry using the R-matrix method. Then to use these parameters to calculate a DR cross-sections using multichannel quantum defect theory (MQDT)'. One could only say that this aim has been partially achieved; that is, whilst input parameters were calculated and a DR cross-section found, the current data only has a temperature range up to 1500 K; as stated in chapter 1 the temperatures relevant to space-vehicle re-entry are $\gtrsim$ 10000 K. This corresponds to an electron impact energy of around 6 eV. This means that all dissociative states that cross the ground state of the ion below $v_i^+ = 29$ must be included in the calculation for a complete description. This data is available using the PECs that were calculated in chapters 4 and 5, it simply needs to prepared for input into the MQDT code. This will form the basis for future work. The inclusion of additional dissociative states also means that cross-sections for initial vibrational levels beyond $v_i^+ = 3$ can be calculated.

As mentioned in section 6.3 of chapter 6, Rydberg-Rydberg couplings were only included between excited states of the ion and the ground state of the ion. This was due to the fact that Rydberg-Rydberg couplings between excited states had not yet been included in the implementation of MQDT used in this study (Chakrabarti et al., 2013). The A $^2\Pi_u$ and B $^2\Sigma_u^+$ have a number of interacting associated Rydberg states, see figures 5.4 and 5.5. Core-excited effects due to Rydberg-Rydberg interaction become more important at higher impact energies as the electron is more likely to be captured into a core-excited Rydberg state; therefore the inclusion of the Rydberg-Rydberg couplings between the A and B states could be important for a calculation over an extended energy range and needs further investigation.

In chapter 1 a number of processes relevant to space-vehicle re-entry were given in table 1.1. Cross-sections for all of these processes can now be calculated. Electron impact electronic excitation cross-section can be calculated using the R-matrix method (Nagy, 2003) using the model developed to calculate the bound and resonant states. A dissociative excitation cross-section can also be found using an MQDT treatment (Chakrabarti et al., 2013), this would require the inclusion of more dissociative states in the MQDT calculation. Electron impact vibrational excitation is the main competing process with DR, that is, when an electron autoionises the additional impact energy introduced by the electron is transferred to the vibrational modes of the molecule resulting in vibrational excitation. Consequently this data was produced in the DR cross-section calculation and is available for future publication. Rotational effects could be included in the DR calculation, although initial calculations showed them to be negligible for N_2^+ further investigations could be carried out. This would also lead to rotational excitation cross-sections (Motapon et al., 2008).

In chapter 6 many resonances associated with Rydberg states appeared in the DR cross-section. These resonances can be used for Rydberg state spectroscopy assignment (Waffeu Tamo et al., 2011).

Finally, this thesis has set a blueprint for the steps that need to be taken to calculate an accurate DR cross-section of a diatomic molecule using the R-matrix method *ab initio*. A model can be proven for the available experimental data and then vibrationally resolved cross-sections for excited vibrational levels can be found. This opens up a wealth of opportunities to find reliable DR cross-sections for molecules for which little experimental data exists.

Appendix A

Von-Neumann-Wigner non-crossing rule

Below is a description of the Von-Neumann-Wigner non-crossing rule (Bransden and Joachain, 2003).

Consider two different potential energy curves (PECs) $E_1(R)$ and $E_2(R)$ where R is the internuclear distance. At the point R_c the PECs are close in energy but distinct and are made up of eigenvalues $E_1^0 = E_1(R_c)$ and $E_2^0 = E_2(R_c)$ of the electronic Hamiltonian $H_c(E)$. The two orthonormal electronic wavefunctions which produce the two potential energy curves are Φ_1 and Φ_2 and assumed to be real.

A perturbation is made to the system by increasing the internuclear distance by ΔR to $R_c+\Delta R$. The Hamiltonian is now

$$H_e(R_c + \Delta R) = H_0 + H', \tag{A.1}$$

where,

$$H' = \Delta R \frac{\partial H_0}{\partial R_c}. \tag{A.2}$$

The perturbed Hamiltonian can then be written as,

$$H'_{ij} = \langle \phi_i | H' | \phi_j \rangle, \ i, j = 1, 2. \tag{A.3}$$

This set of equations has a non-trivial solution if (Bransden and Joachain, 2003),

$$det|\langle \phi_i | H' | \phi_j \rangle - E_{ij}\delta_{ij}| = 0, \tag{A.4}$$

which will only be satisfied if

$$E_1^0 - E_2^0 + H'_{11} - H'_{22} = 0 \tag{A.5}$$

and

$$H'_{12} = 0. \tag{A.6}$$

Therefore if $H'_{12} = 0$ then a crossing can occur, this will only be the case if Φ_1 and Φ_2 are of different symmetries. In general for states of the same symmetry H'_{12} will be non-zero and a crossing cannot occur except where, by coincidence, eqs. (A.5) and (A.6) are both satisfied by the same value of R. As there is only a single parameter to vary, R, it is impossible in general to find a solution to both eqs. (A.5) and (A.6) and states of the same symmetry can therefore not cross.

Appendix B

STATESKIP

It is possible to reduce the number of target states used in the outer region by using the input parameter `nvo`. To use this functionality it is necessary to run SWINTERF twice, once with `ntarg` set to original value with the correct accompanying `idtarg` and with the input `ntarg0` set to the reduced number of target states required. SWINTERF will then output a new input for `ntarg`, `idtarg` and `nvo` into the file '`skip.inf`'. The user then re-runs SWINTERF with these new inputs.

What follows is a description of how the new subrountine in SWINTERF, STATESKIP finds the value of `nvo` so that a reduced `ntarg` can be correctly used in the SWINTERF input.

The first thing to note is that the counting of the orbitals is in `idtarg` order, whereas `nvo` is entered in energy order. This means care must be taken when ordering `nvo` to ensure that the correct number of states have been skipped. The orbitals are counted like:

```
kcount=0
do i=1,ntarg
  kstart=kcount + nvo(idtarg(i))
  kcount=kcount+ncontcsf(idtarg(i))+nvo(idtarg(i))
enddo
```

where `nvo(idtarg(i))` is the number of virtual orbitals associated with the permuted symmetry of `idtarg` element `i` (this is in the same way `mcont` is permuted by symmetry in the inner region SCATCI inputs) and `ncontcsf` is the number of continuum orbitals associated with permuted symmetry `idtarg` element `i` (the final element of each input quartet in `ind` (SWEDMOS) subtracted from `nob` (CONGEN) for each symmetry). `ncontcsf + nvo = notgt` in the inner region SCATCI inputs. To reduce `ntarg`, `nvo` must be changed so that the values of `kstart` in the reduced `ntarg` calculation match the values of `kstart` in the original calculation for the states that aren't to be skipped. The values to which `nvo` needs to be set to can be calculated in the following way:

```
skip=0
j=0
```

```
do i=1,ntarg ! original
           if (i.eq.s(j)) then
             j=j+1
             skip=skip+nvo(idtarg(i))
             skipt(idtarg(i))=skip
             skip=0
           else
             skip=skip+nvo(idtarg(i))+ncontcsf(idtarg(i))
           endif
enddo
```

where `s(j)` is the number of the element of the original idtarg not to be skipped. `skipt(idtarg(i))` gives the value of `nvo` needed for `idtarg` element i. However, this needs to be entered in energy order, so if `idtarg(i)=3` this means this must be the third element in `nvo`. If the above algorithm is followed `skipt(idtarg(i))` will already be in the right order.

Below is an example for a molecule with D_{2h} symmetry (symmetries are counted from 0-7).

```
!INPUTS (FROM SWINTERF AND INNER REGION SCATCI)

! AG symmetry
mgvn=0,
! Triplet
stot=3
! Number of continuum orbitals for each target symmetry (ncontcsf)
notgt=35,18,18,17,17,5,16,16,16,16,18,18,35,5,16,16,
! Symmetry which above continuum orbitals correspond to
mcont=0,1,2,4,4,7,6,5,5,6,2,1,0,7,3,3,
! Number of target states associated with each of the above symmetries
numtgt=8,8,8,7,5,5,8,8,6,6,3,3,6,5,6,8,
! Total number of target states
ntarg=100
! Desired reduction of target states
ntarg0=5,
! see text for explanation of ordering of idtarg, vertical lines are to make the input
! easier to read and should not be included in a real input.
idtarg=1,32,37,39,49,61,64,74|2,34,42,57,59,75,78,89|3,33,41,58,60,76,79,88|
4,14,21,23,54,84,99|5,6,70,87,100|7,10,69,77,86|
11,17,26,30,47,55,80,91|12,18,27,31,48,56,81,92|
9,52,68,72,83,97|8,51,67,71,82,96|16,46,65,15,45,66|13,25,43,50,90,93
|19,20,22,28,98|24,29,44,53,94,95|35,36,38,40,62,63,73,85,
```

`idtarg` is ordered as follows; the number of numbers separated by '|' corresponds to numtgt for each symmetry. The order of each set of numbers corresponds to the order of `mcont`, which is specified by the ordering of the scattering symmetries CONGEN; that is, in this example, the first 8 numbers (1,32,37,39,49,61,64,74) belong to the '0' symmetry which in this example is $^2\mathrm{A_g}$. The numbers contained in each '`numtgt` group' are the index of each of these symmetries in the target properties files (`fort.24` by default). So a $^2\mathrm{A_g}$ state is the 1$^{\mathrm{st}}$, 32$^{\mathrm{nd}}$, 37$^{\mathrm{th}}$, and so on, state given in `fort.24` (which are given in energy order).

We want to reduce `ntarg` to 5. Therefore we want to skip `idtarg` elements 2-8, 10-16, 18-24, 26-31, 33-100. Reducing `ntarg` to 5 means that SWINTERF will ignore any states beyond the first five in energy order. Therefore s(0)=1, s(1)=9, s(2)=17, s(3)=25, s(4)=32. Using the above algorithm the resulting set of inputs will be:

```
ntarg=5,

idtarg=1,2,3,4,5,

nvo=0,245,126,126,108,
```

Appendix C

Irreducible representations

Table C.1 gives molecular orbitals in the D_{2h} symmetry group, used by the UKRmol codes and MOLPRO, in terms of ℓ and m_ℓ. Linear homonuclear molecules such as N_2 are in the $D_{\infty h}$ irreducible representation. The relationship between molecular orbitals in D_{2h} and molecular orbitals in $D_{\infty h}$ is shown in table C.2. Using these two tables, a new table, table C.3, can be constructed which gives molecular orbitals in $D_{\infty h}$ in terms of ℓ and m_ℓ. Finally in table C.4 electronic states in $D_{\infty h}$ are written in terms D_{2h}.

Table C.1: D_{2h} symmetry group up to $\ell = 4$ in terms of ℓ and m_ℓ.

ℓ									
					$m_\ell = 0$				
0					a_g				
				$m_\ell = -1$	$m_\ell = 0$	$m_\ell = 1$			
1				b_{2u}	b_{1u}	b_{3u}			
			$m_\ell = -2$	$m_\ell = -1$	$m_\ell = 0$	$m_\ell = 1$	$\mathrm{m}_\ell = 2$		
2			b_{1g}	b_{2g}	a_g	b_{3g}	a_g		
		$m_\ell = -3$	$m_\ell = -2$	$m_\ell = -1$	$m_\ell = 0$	$m_\ell = 1$	$\mathrm{m}_\ell = 2$	$m_\ell = 3$	
3		b_{2u}	a_u	b_{2u}	b_{1u}	b_{3u}	b_{1u}	b_{3u}	
	$m_\ell = -4$	$m_\ell = -3$	$m_\ell = -2$	$m_\ell = -1$	$m_\ell = 0$	$m_\ell = 1$	$\mathrm{m}_\ell = 2$	$m_\ell = 3$	$m_\ell = 4$
4	b_{1g}	b_{2g}	b_{1g}	b_{2g}	a_g	b_{3g}	a_g	b_{3g}	a_g

Table C.2: Molecular orbitals in $D_{\infty h}$ in terms of D_{2h}.

$D_{\infty h}$		D_{2h}
σ_g	$\longrightarrow$	a_g
σ_u	$\longrightarrow$	b_{1u}
π_g	$\longrightarrow$	$b_{3g} + b_{2g}$
π_u	$\longrightarrow$	$b_{3u} + b_{2u}$
δ_g	$\longrightarrow$	$b_{1g} + a_g$
δ_u	$\longrightarrow$	$b_{1u} + a_u$
ϕ_g	$\longrightarrow$	$b_{3g} + b_{2g}$
ϕ_u	$\longrightarrow$	$b_{3u} + b_{2u}$
γ_g	$\longrightarrow$	$b_{1g} + a_g$

Table C.3: Molecular orbitals in $D_{\infty h}$ in terms of ℓ and m_ℓ.

ℓ	$\lvert m_\ell \rvert = 0$	$\lvert m_\ell \rvert = 1$	$\lvert m_\ell \rvert = 2$	$\lvert m_\ell \rvert = 3$	$\lvert m_\ell \rvert = 4$
0	σ_g				
1	σ_u	π_u			
2	σ_g	π_g	δ_g		
3	σ_u	π_u	δ_u	ϕ_u	
4	σ_g	π_g	δ_g	ϕ_g	γ_g

Table C.4: Electronic states in $D_{\infty h}$ in terms of D_{2h}.

$D_{\infty h}$		D_{2h}
Σ_g^+	$\longrightarrow$	A_g
Π_u	$\longrightarrow$	$B_{3u} + B_{2u}$
Σ_g^-	$\longrightarrow$	B_{1g}
Σ_u^+	$\longrightarrow$	B_{1u}
Π_g	$\longrightarrow$	$B_{3g} + B_{2g}$
Σ_u^-	$\longrightarrow$	A_u
Φ_u	$\longrightarrow$	$B_{3u} + B_{2u}$
Φ_g	$\longrightarrow$	$B_{3g} + B_{2g}$
Δ_g	$\longrightarrow$	$B_{1g} + A_g$
Δ_u	$\longrightarrow$	$B_{1u} + B_u$
Γ_g	$\longrightarrow$	$B_{1g} + A_g$

Bibliography

Anderson E, Bai Z, Bischof C, Blackford S, Demmel J, Dongarra J, Du Croz J, Greenbaum A, Hammarling S, McKenney A and Sorensen D 1999 *LAPACK Users' Guide* third edn Society for Industrial and Applied Mathematics Philadelphia, PA.

Anderson J D 1989 *Hypersonic and High Temperature Gas Dynamics* McGraw-Hill New York.

Annaloro J, Bultel A and Omaly P 2014 *J. Thermophys. and Heat Transfer* **28**(4), 608–622.

Arfken G B, Weber H J and Harris F E 2013 *Mathematical Methods for Physicists: A Comprehensive Guide* Elsevier.

Arthurs A M and Dalgarno A 1960 *Proc. R. Soc. London Series A* **256**(1287), 540–551.

Baccarelli I, Sebastianelli F, Gianturco F A and Sanna N 2009 *Euro. Phys. J. D* **51**, 131–136.

Baker T S, Dormand J R and Prince P J 1999 *Appl. Numer. Math.* **29**, 171–188.

Ballance C P, McLaughlin B M, Nagy O, Berrington K A and Burke P G 1998 *J. Phys. B: At. Mol. Opt. Phys.* **31**, L305.

Baluja K L, Burke P G and Morgan L A 1982 *Comput. Phys. Commun.* **27**, 299.

Bates D R and Massey H S W 1946 *Proc. R. Soc. Lond. A* **187**(1010), 261–296.

Bialecke E P and Dougal A A 1958 *J. Geophys. Res.* **63**(3), 539–546.

Bird G 1989 *in* 'AIAA, Fluid Dynamics, 20th Plasma Dynamics and Lasers Conference' Vol. 1.

Bird G A 2009 *26th Symposium on Rarefied Gas Dynamics* American Institute of Physics.

Bird G A 2011 *Phys. of Fluids* **23**(10).

Bloch C 1957 *Nuclear Physics* **4**, 503 – 528.

Bominaar J, Schoemaecker C, Dam N, Meulen J T and Groenenboom G 2007 *Chemical Physics Letters* **435**(4âĂŞ6), 242 – 246.

Bortner H 1969 *Review of Rate Constants of Selected Reactions of Interest in Re-Entry Flow Fields in the Atmosphere* US National Bureau of Standards Technical Note Space Sciences Laboratory, Missile and Space Division, General Electric Company.

Boyd I D 2007 *AIAA-2007-206, 45th AIAA Aerospace Sciences Meeting and Exhibit* .

Branchett S E 1991 Bound and continuum states of diatomic molecules using the R-matrix method PhD thesis University College London.

Bransden B H and Joachain C J 2003 *Physics of Atoms and Molecules* Pearson Education.

Bultel A and Annaloro J 2013 *Plasma Sources Sci. Technol.* **22**(2), 025008.

Bultel A, Chéron B G, Bourdon A, Motapon O and Schneider I F 2006 *Phys. of Plasmas* **13**(4).

Bultel A, van Ootegem B, Bourdon A and Vervisch P 2002 *Phys. Rev. E* **65**, 046406.

Burke P 1973 *Computer Physics Communications* **6**(6), 288 – 302.

Burke P G 2011 *R-Matrix Theory of Atomic Collisions* Springer.

Burke P G, Hibbert A and Robb W D 1971 *J. Phys. B: At. Mol. Phys.* **4**, 153–161.

Burke P G, Mackey I and Shimamura I 1977 *J. Phys. B: At. Mol. Phys.* **10**, 2497–2512.

Burke P G and Seaton M J 1984 *J. Phys. B: At. Mol. Phys.* **17**(20), L683.

Canosa A, Gomet J C, Rowe B R and Queffelec J L 1991 *J. Chem. Phys.* **94**, 7159–7163.

Carata L, Orel A E, Raoult M, Schneider I F and Suzor-Weiner A 2000 *Phys. Rev. A* **62**(5), 052711.

Carr J M, Galiatsatos P G, Gorfinkiel J D, Harvey A G, Lysaght M A, Madden D, Masin Z, Plummer M and Tennyson J 2012 *Euro. Phys. J. D* **66**, 58.

Chakrabarti K, Backodissa-Kiminou D R, Pop N, Mezei J Z, Motapon O, Lique F, Dulieu O, Wolf A and Schneider I F 2013 *Phys. Rev. A* **87**(2), 022702.

Cossart D and Cossart-Magos C 2004 *J. Chem. Phys.* **121**, 7148–7152.

Cunningham A J and Hobson R M 1972 *J. Phys. B: At. Mol. Phys.* **5**, 2328.

de Lange A and Ubachs W 1999 *Chem. Phys. Lett.* **310**, 471 – 476.

Dunning T H 1989 *J. Chem. Phys.* **90**, 1007–1023.

Edlén B 1964 *Handbuch der Physik* Vol. 27 Springer Berlin.

Edwards S, Roncin J Y, Launay F and Rostas F 1993 *J. Mol. Spectrosc.* **162**, 257 – 267.

Ermler W C, McLean A D and Mulliken R S 1982 *J. Phys. Chem.* **86**, 1305–1314.

Faire A C and Champion K S W 1959 *Phys. Rev.* **113**(1), 1–6.

Faire A C, Fundingsland O T, Aden A and Champion K S W 1958 *J. Applied Phys.* **29**(6), 928–930.

Faure A, Gorfinkiel J D, Morgan L A and Tennyson J 2002 *Comput. Phys. Commun.* **144**, 224–241.

Feshbach H 1958 *Ann. Phys.* **5**(4), 357 – 390.

Feshbach H 1962 *Ann. Phys.* **19**(2), 287 – 313.

Fifirig M 2014 *Molecular Physics* **112**(14), 1910–1917.

Florescu A I, Ngassam V, Schneider I F and Suzor-Weiner A 2003 *J. Phys. B: At. Mol. Opt. Phys.* **36**(6), 1205.

Florescu-Mitchell A I and Mitchell J B A 2006 *Phys. Rep.* **430**, 277 – 374.

Gailitis M 1976 *J. Phys. B: At. Mol. Opt. Phys.* **9**(5), 843.

Gallis M A, Bond R B and Torczynski J R 2009 *J. Chem. Phys.* **131**, 124311.

Geoghegan M, Adams N G and Smith D 1991 *J. Phys. B: At. Mol. Opt. Phys.* **24**, 2589.

Gillan C J, Tennyson J and Burke P G 1995 *in* W Huo and F. A Gianturco, eds, 'Computational methods for Electron-molecule collisions' pp. 239–254.

Giusti A 1980 *J. Phys. B: At. Mol. Phys.* **13**(19), 3867.

Guberman S 2003 *in* 'Dissocative Recombination of Molecular Ions with Electrons' Kluwer/Plenum Publishers New York pp. 187–196.

Guberman S L 1991 *Geophysical Research Letters* **18**(6), 1051–1054.

Guberman S L 2007 *J. Phys. Chem. A* **111**, 11254–11260.

Guberman S L 2012 *J. Chem. Phys.* **137**, 074309.

Guberman S L 2013 *J. Chem. Phys.* **139**, 124318.

Gupta R N, Yos J M, Thompson R A and Lee K P 1990 *A review of reaction rates and thermodynamic and transport properties for an 11-species air model for chemical and thermal nonequilibrium calculations to 30000 K* NASA Reference publication No. 1232.

Hackam R 1965 *Planetary and Space Sci.* **13**(7), 667 – 674.

Hashimoto T and Kanamori H 2006 *J. Mol. Spectrosc.* **235**, 104 – 110.

Hazi A U 1979 *Phys. Rev. A* **19**, 920–922.

Hochlaf M, Ndome H and Hammoutène D 2010 *J. Chem. Phys.* **132**, 104310.

Hochlaf M, Ndome H, Hammoutène D and Vervloet M 2010 *J. Phys. B: At. Mol. Opt. Phys.* **43**, 245101.

Huber K and Herzberg G 1979 *Constants of Diatomic Molecules* Van Nostrand Reinhold New York. Available via `http://webbook.nist.gov`.

Huber K P and Jungen C 1990 *J. Chem. Phys.* **92**, 850–861.

Johnston H S 1968 Gas phase reaction kinetics of neutral oxygen species Technical report NSRDS-NBS 20 US Department of Commerce.

Kasner W H, Rogers W A and Biondi M A 1961 *Phys. Rev. Lett.* **7**(8), 321–323.

Kawamoto Y, Fujitake M and Ohashi N 1997 *J. Mol. Spectrosc.* **185**, 330 – 335.

Kella D, Johnson P J, Pedersen H B, Vejby-Christensen L and Andersen L H 1996 *Phys. Rev. Lett.* **77**(12), 2432–2435.

Kreckel H, Petrignani A, Novotny O, Crabtree K, Buhr H, McCall B J and Wolf A 2012 *Phil. Trans. Roy. Soc. A* **370**, 5088–5100.

Larsson M and Orel A E 2008 *Dissociative Recombination of Molecular Ions* Cambridge Molecular Science Cambridge University Press.

Levelt P F and Ubachs W 1992 *Chem. Phys.* **163**, 263 – 275.

Levine I N 2000 *Quantum Chemistry* Prentice-Hall.

Lewis B R, Baldwin K G H, Heays A N, Gibson S T, Sprengers J P, Ubachs W and Fujitake M 2008 *J. Chem. Phys.* **129**, 204303.

Lewis B R, Heays A N, Gibson S T, Lefebvre-Brion H and Lefebvre R 2008 *J. Chem. Phys.* **129**, 164306.

Li Z, Ozawa T, Sohn I and Levin D A 2011 *Phys. Fluids* **23**, 066102.

Little D A, Chakrabarti K, Mezei J Z, Schneider I F and Tennyson J 2014 *Phys. Rev. A* **90**(5), 052705.

Little D A and Tennyson J 2013 *J. Phys. B: At. Mol. Opt. Phys.* **46**, 145102.

Little D A and Tennyson J 2014 *J. Phys. B: At. Mol. Opt. Phys.* **47**, 105204.

Lofthus A and Krupenie P H 1977 *J. Phys. Chem. Ref. Data* **6**, 113–307.

Mahdavi M R, Hasted J B and Nakshbandi M M 1971 *J. Phys. B: At. Mol. Phys.* **4**, 1726.

Marriot P and Marriot P 2012 Personal communication.

Marx D and Hutter J 2009 *Ab Initio Molecular Dynamics Basic Theory and Advanced Methods* Cambridge University Press.

Masin Z and Gorfinkiel J D 2012 *J. Chem. Phys.* **137**, 204312.

Mehr F J and Biondi M A 1969 *Phys. Rev.* **181**, 264–271.

Mentzoni M H 1963 *J. Geophys. Res.* **68**(14), 4181–4186.

Michels H H 2007 *Electronic Structure of Excited States of Selected Atmospheric Systems* John Wiley and Sons, Inc.

Morgan L A 1984 *Comput. Phys. Commun.* **31**(4), 419 – 422.

Morgan L A, Burke P G and Gillan C J 1990 *J. Phys. B: At. Mol. Opt. Phys.* **23**(1), 99.

Morgan L A, Gillan C J, Tennyson J and Chen X 1997 *J. Phys. B: At. Mol. Opt. Phys.* **30**, 4087–4096.

Morgan L A, Tennyson J and Gillan C J 1998 *Comput. Phys. Commun.* **114**, 120–128.

Motapon O, Fifirig M, Florescu A, Waffeu-Tamo F O, Crumeyrolle O, Varin-Breant G, Bultel A, Vervisch P, Tennyson J and Schneider I F 2006 *Plasma Sources Sci. Technol.* **15**, 23–32.

Motapon O, Tamo F O W, Urbain X and Schneider I F 2008 *Phys. Rev. A* **77**(5), 052711.

Mul P M and McGowan J W 1979 *J. Phys.B: At. Mol. Phys.* **12**, 1591.

Nagy O 2003 *Chem. Phys.* **286**, 109 – 114.

Nagy O, Ballance C P, Berrington K A, Burke P G and McLaughlin B M 1999 *J. Phys. B: At. Mol. Opt. Phys.* **32**, L469.

NASA 1975 'Apollo program summary report'.
URL: *http://history.nasa.gov/apsr/apsr.htm*

Ndome H, Hochlaf M, Lewis B R, Heays A N, Gibson S T and Lefebvre-Brion H 2008 *J. Chem. Phys.* **129**, 164307.

Nestmann B M, Pfingst K and Peyerimhoff S D 1994 *J. Phys. B: At. Mol. Opt. Phys.* **27**(11), 2297.

Ngassam V, Florescu A, Pichl L, Schneider I, Motapon O and Suzor-Weiner A 2003 *Euro. Phys. J. D* **26**(2), 165–171.

Noble C and Nesbet R 1984 *Comput. Phys. Commun.* **33**(4), 399 – 411.

Noren C, Yousif F B and Mitchell J B A 1989 *J. Chem. Soc., Faraday Trans. 2* **85**(10), 1697–1703.

Orel A E 2005 *J. Phys: Conf. Series* **4**(1), 142.

Ozawa T, Zhong J and Levin D A 2008 *Phys. Fluids* **20**, 046102.

Park C 1990 *Nonequilibrium Hypersonic Aerothermodynamics* A Wiley-interscience publication John Wiley & Sons.

Park C 1993 *J. Thermophys. Heat Transf.* **7**, 385–398.

Peterson J R, Le Padellec A, Danared H, Dunn G H, Larsson M, Larson A, Peverall R, Stromholm C, Rosen S, af Ugglas M and van der Zande W J 1998 *J. Chem. Phys.* **108**, 1978–1988.

Quigley L and Berrington K 1996 *J. Phys. B: At. Mol. Opt. Phys.* **29**, 4529–4542.

Quigley L, Berrington K and Pelan J 1998 *Comput. Phys. Commun.* **114**, 225–235.

Rabadán I and Tennyson J 1996 *J. Phys. B: At. Mol. Opt. Phys.* **29**, 3747–3761.

Rabadán I and Tennyson J 1997 *J. Phys. B: At. Mol. Opt. Phys.* **30**, 1975–1988. erratum 31, 4485-4487 (1998).

Rabadán I, Tennyson J and Morgan L A 1998 *Chem. Phys. Lett.* **285**, 105–113.

Reese J M, Gallis M A and Lockerby D A 2003 *Phil. Trans. R. Soc. Lond. A* **361**(1813), 2967–2988.

Rescigno T, McCurdy C, Orel A and Lengsfield, B.H. I 1995 *in* W Huo and F Gianturco, eds, ‘Computational Methods for Electron - Molecule Collisions’ Springer US pp. 1–44.

Robb W 1972 *Comput. Phys. Commun.* **4**(1), 16 – 19.

Roncin J Y, Launay F and Larzilliere M 1984 *Phys. Rev. Lett.* **53**, 159–162.

Roncin J Y, Launay F, Subtil J L and Yoshino K 1991 *Planet. Space Sci.* **39**, 1301 – 1304.

Roncin J Y, Launay F and Yoshino K 1989 *J. Mol. Spectrosc.* **134**, 390 – 394.

Roncin J Y, Subtil J L and Launay F 1998 *J. Mol. Spectrosc.* **188**, 128 – 137.

Roos J B, Orel A E and Larson A 2009 *Phys. Rev. A* **79**(6), 062510.

Salumbides E J, Khramov A and Ubachs W 2009 *J. Phys. Chem. A* **113**(11), 2383–2386.

Sarpal B K, Branchett S E, Tennyson J and Morgan L A 1991 *J. Phys. B: At. Mol. Opt. Phys.* **24**, 3685–3699.

Sarpal B K, Tennyson J and Morgan L A 1994 *J. Phys. B: At. Mol. Opt. Phys.* **27**, 5943–5953.

Schmidt H T, Vejby-Christensen L, Pedersen H B, Kella D, Bjerre N and Andersen L H 1996 *J. Phys. B: At. Mol. Opt. Phys.* **29**(12), 2485.

Schneider B 1975 *Chem. Phys. Lett.* **31**(2), 237 – 241.

Schneider B I and Hay P J 1976 *Phys. Rev. A* **13**, 2049–2056.

Schneider I F, Dulieu O, Giusti-Suzor A and Roueff E 1994 *Astrophys. J.* **424**, 983–987.

Schneider I F, Rabadán I, Carata L, Tennyson J, Andersen L H and Suzor-Weiner A 2000 *J. Phys. B: At. Mol. Opt. Phys.* **33**, 4849–4861.

Schneider I F, Strömholm C, Carata L, Urbain X, Larsson M and Suzor-Weiner A 1997 *J. Phys. B: At. Mol. Opt. Phys.* **30**(11), 2687.

Schulz G J 1973 *Rev. Mod. Phys.* **45**, 423–486.

Seaton M J 1983 *Rep. Prog. Phys.* **46**(2), 167.

Sheehan C H and St.-Maurice J P 2004 *J. Geophys. Res.: Space Phys.* **109**, A03302.

Shimamura I 2011 *J. Phys. B: At. Mol. Opt. Phys.* **44**, 201002.

Shimamura I 2012 *in* C. A Nicolaides, E Brändas and J. R Sabin, eds, 'Advances in Quantum Chemistry' Vol. 63 of *Advances in Quantum Chemistry* Academic Press pp. 165 – 245.

Shimamura I, McCann J F and Igarashi A 2006 *J. Phys. B: At. Mol. Opt. Phys.* **39**, 1847–1854.

Singh R B and Rai D K 1966 *J. Mol. Spectrosc.* **19**, 424 – 434.

Smith F T 1960 *Phys. Rev.* **118**, 349–356.

Sochi T and Storey P J 2013 *Euro. Phys. J. Plus* **128**, 82.

Spelsberg D and Meyer W 2001 *J. Chem. Phys.* **115**, 6438–6449.

Sprengers J P, Johansson A, L'Huillier A, Wahlström C G, Lewis B R and Ubachs W 2004 *Chem. Phys. Lett.* **389**, 348 – 351.

Stahel D, Leoni M and Dressler K 1983 *J. Chem. Phys.* **79**, 2541–2558.

Stibbe D T and Tennyson J 1996 *J. Phys. B: At. Mol. Opt. Phys.* **29**, 4267–4283.

Stibbe D T and Tennyson J 1998 *Comput. Phys. Commun.* **114**, 236–242.

Stibbe D T and Tennyson J 1999 *Chem. Phys. Lett.* **308**, 532–536.

Suzuki T and Kakimoto M 1982 *J. Mol. Spectrosc.* **93**, 423 – 432.

Tennyson J 1996 *J. Phys. B: At. Mol. Opt. Phys.* **29**, 1817–1828.

Tennyson J 2004 *J. Phys. B: At. Mol. Opt. Phys.* **37**, 1061–1071.

Tennyson J 2010 *Phys. Rep.* **491**, 29–76.

Tennyson J, Brown D B, Munro J J, Rozum I, Varambhia H N and Vinci N 2007 *J. Phys: Conf. Series* **86**, 012001.

Tennyson J and Noble C J 1984 *Comput. Phys. Commun.* **33**, 421–424.

van der Kamp A B, Cosby P C and van der Zande W J 1994 *Chem. Phys.* **184**, 319 – 333.

Verma R D and Jois S S 1984 *J. Phys. B: At. Mol. Opt. Phys.* **17**, 3229.

Waffeu Tamo F O, Buhr H, Motapon O, Altevogt S, Andrianarijaona V M, Grieser M, Lammich L, Lestinsky M, Motsch M, Nevo I, Novotny S, Orlov D A, Pedersen H B, Schwalm D, Sprenger F, Urbain X, Weigel U, Wolf A and Schneider I F 2011 *Phys. Rev. A* **84**(2), 022710.

Werner H J, Knowles P J, Lindh R, Manby F R, Schütz M et al. 2010 'MOLPRO, a package of ab initio programs'. see `http://www.molpro.net/`.

Whang T J, Zhao G, Stwalley W C and Wuc C Y R 1996 *J. Quant. Spectrosc. Radiat. Transf.* **55**, 335 – 344.

Wigner E P 1946 *Phys. Rev.* **70**, 606–618.

Wigner E P and Eisenbud L 1947 *Phys. Rev.* **72**, 29–41.

Zhang R, Baluja K L, Franz J and Tennyson J 2011 *J. Phys. B: At. Mol. Opt. Phys.* **44**, 035203.

Zipf E C 1980 *Geophys. Res. Lett.* **7**, 645–648.